

Micro- and Nanoscale Characterization of Polymeric Materials by Means of Digital Image Correlation Techniques

Von der Fakultät Mathematik, Naturwissenschaften und Informatik
der Brandenburgischen Technischen Universität Cottbus

zur Erlangung des akademischen Grades

Doktor der Ingenieurwissenschaften
(Dr.-Ing.)

genehmigte Dissertation

vorgelegt von

Dipl.-Ing.

Jürgen Keller

geboren am 10.06.1972 in Bad Sobernheim

Gutachter: Prof. Dr. Monika Bauer

Gutachter: Prof. Dr. Bernd Michel

Gutachter: Prof. Dr. Norbert Meyendorf

Tag der mündlichen Prüfung: 09.05.2005

Danksagung

Die vorliegende Dissertation entstand während meiner Tätigkeit als wissenschaftlicher Mitarbeiter am Lehrstuhl für Polymerwerkstoffe der Brandenburgischen Technischen Universität Cottbus in Zusammenarbeit mit der Abteilung Mechanical Reliability and Micro Materials des Fraunhofer Instituts für Zuverlässigkeit und Mikrointegration (IZM), Berlin.

Ich bedanke mich herzlich bei allen, die zum Gelingen dieser Arbeit beigetragen haben.

Frau Prof. Dr. Monika Bauer danke ich für die Möglichkeit, die Arbeit in ihrem Arbeitskreis durchzuführen, und für den mir gewährten Freiraum bei der Durchführung der Arbeit.

Bei Herrn Prof. Dr. Bernd Michel bedanke ich mich für die fördernde Unterstützung und das stete Interesse am Fortschritt meiner Arbeit.

Herrn Prof. Dr. Norbert Meyendorf danke ich für die Übernahme des Gutachtens und die Zusammenarbeit auf dem Gebiet der Nanodeformationsanalyse.

Herrn Christoph Uhlig und Herrn Dr. Olaf Kahle gilt mein Dank für die wertvolle Einführung in das Verfahren der optischen Rissspitzenerfassung (OCT), was gewissermaßen die Initialzündung der Promotion ausmachte.

Herrn Dr. Dietmar Vogel danke ich für die Vorleistungen, die zum Gelingen des Verfahrens der SPM-basierten Deformationsmessung wesentlich beigetragen haben. Insbesondere die wertvollen Anregungen und Diskussionsrunden werden mir in Erinnerung bleiben.

In besonderem Maße möchte ich mich bei Herrn Dr. Habib Badri Ghavifekr für die Unterstützung und die wertvollen Diskussionen bei der Durchführung einiger FE-Simulationen bedanken.

Dr. Hans Walter und Dr. Olaf Wittler unterstützten mich bei messtechnischen Aufgaben rund um die Materialcharakterisierung.

Frau Astrid Gollhardt danke ich für die Durchführung der REM-Aufnahmen und die gute Zusammenarbeit innerhalb der Arbeitsgruppe.

Ich bedanke mich bei der Image Instruments GmbH, Chemnitz, für die gute Zusammenarbeit bei der Entwicklung der Grauwertkorrelationssoftware.

Ein kollegialer Dank gilt Dr. Bernhard Wunderle, Dr. Olaf Wittler, Dr. Ralph Schacht, Florian Schindler-Seafkow, Dr. Eckardt Höhne und Dr. Marcus Sonner, die mit ihrem gesellschaftspolitischen Diskussionsforum den Blick auf weitere Dimensionen menschlichen Daseins offen hielten.

Ich bedanke mich bei allen Kollegen für die stets angenehme und fruchtbare Arbeitsatmosphäre.

Ein großer Dank gilt Frau Doris Storrer für das Korrekturlesen des Manuskripts.

Meiner Familie danke ich für die Unterstützung während meiner Ausbildung.

Nicht zuletzt danke ich meiner Freundin Dagmar für das Verständnis und den notwendigen Rückhalt, den sie mir während der Promotion geben konnte.

Berlin im Mai 2005

Jürgen Keller

Abstract

This thesis comprises the development, accuracy testing and application of the so-called nanoDAC method (nano Deformation Analysis by Correlation). The method combines scanning probe microscopy (SPM) images and digital image correlation (DIC) to derive an in-situ deformation measurement technique. The results are full-field 2D displacement fields with nanometer resolution. The method can be performed on bulk materials, thin films, and on microelectronic components.

A thermosetting polymer material typically applied in microelectronics systems serves as an example to emphasize the capability of the method. Crack tip opening fields of a compact tension (CT) specimen are experimentally determined by means of nanoDAC and the obtained fields act as the basis for the extraction of the stress intensity factor as a fracture mechanical property.

In addition finite element analyses are carried out and an adaptation strategy between experimental and numerical results is developed.

Zusammenfassung

Die Arbeit beinhaltet die Entwicklung, Prüfung der Messgenauigkeit und Anwendung der so genannten nanoDAC Methode (nano Deformation Analysis by Correlation), die Rastersondenmikroskopie und digitale Bildkorrelation zur Ableitung einer in-situ Deformationsmesstechnik kombiniert. Als Ergebnis erhält man 2D-Verschiebungsfelder mit Auflösungsgenauigkeit im Nanometerbereich. Die Methode kann an Bulkmaterialien, dünnen Schichten und mikroelektronischen Komponenten angewendet werden.

Ein für mikroelektronische Systeme typisches Thermoset-Polymer dient als Anwendungsbeispiel der Methode. Rissöffnungsfelder an einer CT- (compact tension) Probe werden mittels der nanoDAC Methode experimentell ermittelt und die daraus abgeleiteten Felder stellen die Basis zur Ableitung des Spannungsintensitätsfaktors als bruchmechanische Kenngröße dar.

Zusätzlich werden Finite Elemente Analysen durchgeführt und eine Adaptionstrategie zwischen experimentellen und numerischen Ergebnissen wird entwickelt.

Contents

Danksagung	i
Abstract	ii
Zusammenfassung	ii
Abbreviations and List of Symbols	vi
1 Introduction and Motivation	1
2 Theoretical and Experimental Background	3
2.1 State of the Art of Submicron In-Situ Loading Tests	3
2.1.1 Experimental Mechanics by Scanning Probe Microscopy	4
2.1.2 Micro Deformation Measurement Techniques	6
2.1.3 The Combination of SPM Methods and Digital Image Correlation	8
2.2 The Method of Digital Image Correlation	9
2.2.1 Cross Correlation Algorithms on Gray Scale Images	9
2.2.2 Subpixel Analysis for Enhanced Resolution	12
2.2.3 Results of Digital Image Correlation	12
2.2.4 Accuracy	13
2.3 Fracture Mechanics Approach	14
2.3.1 Crack Tip Field Analysis	15
2.3.2 K-Concept	16
2.3.3 Energy Release Rate	18
2.4 Numerical Fracture Mechanics Utilizing Integral Concepts	19

3	Testing and Results	22
3.1	Polymeric Materials	22
3.1.1	Mechanical Behavior of Polymeric Materials	22
3.1.2	Cyanate Ester Thermosets	25
3.1.3	Tested Material Systems	28
3.2	Viscoelastic Material Characterization	28
3.2.1	Viscoelasticity	28
3.2.2	Modeling of Viscoelasticity	30
3.2.3	Time-Temperature-Superposition	31
3.2.4	Experimental Setup and Data Acquisition	31
3.2.5	Results of Viscoelastic Material Characterization	32
3.3	Advanced Fracture Analysis for Polymers	32
3.3.1	Optical Crack Tracing (OCT) Technique	33
3.3.2	Measurement of the <i>R</i> -curve in Comparison to ASTM D5045	35
3.3.3	Results of OCT	37
3.4	Crack Field Analysis by In-Situ AFM Measurements - nanoDAC	38
3.4.1	General Aspects of Scanning Probe Microscopy	38
3.4.2	Instrumentation of AFM measurements	40
3.4.3	Stability Aspects of SPM Measurements	41
3.4.4	Results of In-Situ AFM Measurements	52
3.5	Fractography by SEM and SPM methods	58
4	Discussion - Comp. of Experiment and Simulation	62
4.1	Crack Opening Displacement Analysis	62
4.2	Finite Element Model	64
4.3	Crack Front Curvature	66
4.3.1	Effect of Crack Front Curvature on R-Curve	68
4.3.2	Effect of Crack Front Curvature on Crack Tip Field	69
4.4	Influence of Viscoelasticity on Crack Tip Field	69
4.5	Influence of Plasticity on Crack Tip Field	70
4.6	Adaptation Strategies - Simulation and Experiment	73
4.6.1	Adapted Finite Element Concept	73
4.6.2	Mesh Transfer from FEA to Experiment	75
4.6.3	Results Platform	77
4.6.4	Verification Algorithm	77
4.6.5	Concluding Remarks on Adaptation Concept	84

CONTENTS

v

5 Conclusions and Outlook

85

Bibliography

88

Lebenslauf

98

Abbreviations and List of Symbols

Abbreviations

AFAM	Atomic force acoustic microscopy
AFM	Atomic force microscopy
APDL	ANSYS parametric design language
BMI	Bismaleimide
DCBA	Bisphenol-A dicyanate
DGBA	Diglycidyl ether of bisphenol-A
DIC	Digital image correlation
CE	Cyanate ester resin
COD	Crack opening displacement
CT	Compact tension (specimen)
FEA/FEM	Finite element analysis/method
FIB	Focused ion beam
HVEM	High voltage electron microscopy
IC	Integrated circuit
LEFM	Linear elastic fracture mechanics
LFM	Lateral force microscopy
LSM	Laser scanning microscopy
MEMS/NEMS	Micro/nano electronic mechanical systems
micro-/nanoDAC	Micro/nano deformation analysis by means of correlation algorithms
OCT	Optical crack tracing
OIM	Optical interference microscopy
OLS	Organically modified layered silicates
PES	Polyethersulfone
P-T	Phenolic triazine
PMMA	Polymethyl-methacrylate
PMR	Polymerizable monomeric reagents
PSPD	Position-sensitive photodetector
PSU	Polysulfone
PVC	Polyvinylchloride
PZT	Lead zirconate titanate
ROI	Region of interest
SEM	Scanning electron microscopy
SFM	Scanning force microscopy
SPM	Scanning probe microscopy
STM	Scanning tunneling microscopy
TEM	Transmission electron microscopy
UFM	Ultrasonic force microscopy

List of Symbols

α	Normalized crack length
Γ	Contour
ΔT^*	ΔT^* -integral
δ_{jk}	Kronecker's delta
ϵ	Strain
η	Fluid viscosity
θ	Angle of cylindrical coordinate-system at crack tip
κ	Factor
μ	Shear modulus
ν	Poisson's ratio
Π	Potential energy
ρ	Radius of process zone
ρ	Rotation angle
σ	Stress
τ	Relaxation time
A	Area
a	Crack length
a_T	Temperature shift factor
B	Thickness of CT-specimen
C	Fitting parameter
$C_{1,2}$	Fitting parameters
C^*	C^* -Integral
D	Creep compliance
d	Pin displacement
E	Young's modulus
F	Force
f	Function
$f(\alpha)$	Geometry function
\mathcal{G}	Energy release rate
I	Intensity, gray scale value
K_I	Stress intensity factor (mode I)
K_{Ic}	Critical stress intensity factor (mode I), fracture toughness
$K_{i',j'}$	Cross correlation coefficient
k	Subpixel shift resolution
l	Image size in pixel
J	J -integral
\hat{J}	\hat{J} -integral
J_G	Generalized J -Integral

M_I	Average gray value
m	Image resolution
R	Radius of K-dominated zone
r	Radius of cylindrical coordinate-system at crack tip
r_p	Radius of inelastic zone
T	Traction vector
T	Temperature
T_m	Melting temperature
T_g	Glass transition temperature
t	Time
u	Displacement
V	Volume
W	Width of CT-specimen
W	Strain energy
w	Strain energy density

Chapter 1

Introduction and Motivation

Today, nanotechnology is a motor for the development of new products with the term nanotechnology itself being used for developments in sometimes very different research fields. A lot of the ideas popping up whether they are published by semi-scientist or more serious research groups have to be understood in an interdisciplinary way. Scientists from physics, chemistry, biology, and engineering have to cooperate closely to develop and establish highly innovative nanotechnological products.

As broad as the term nanotechnology can be defined as many application fields for nanotechnological products can be found. They range from aerospace, medicine, microelectronics, automotive applications to sports equipment. A key for the success of a new product or a new production technology, such as the often mentioned self assembling manufacturing technologies [1] is not only the functionality of the design but also the reliability of the product.

Especially in automotive application, massive reliability problems arise with the growing amount of microelectronic devices per vehicle. Newly developed sensing, actuating, and monitoring devices for active safety systems, motor and emission management, active steering or even for entertainment systems have brought new reliability issues to the agenda. Advanced micromechanical crack initiation and propagation, fatigue and failure models are the most important instruments for reliability evaluation of such microsystems.

With ongoing miniaturization from micro electronic mechanical systems (MEMS) towards nano electronic mechanical systems (NEMS), there is a need for new reliability concepts making use of meso-type (micro to nano) or fully nanomechanical approaches. For the development of theoretical descriptions and their numerical implementation on the basis of simulation tools experimental verification will be of major interest. Therefore, there is a need for measurement techniques with capabilities of determination and evaluation of strain fields with very local (nanoscale) resolution.

In nanotechnological research the objects of interest can be very different. For example, the need for higher operational frequencies and higher component integration of microelectronic devices leads to ultrathin layers only a few layers of atoms thick. Another research field is materials filled with nanoparticles, nanotubes or inherent nanophases resulting into completely different material behavior compared to a unfilled or microstructured material. Both of these technological research fields have in common that material interface will play

a predominate role. The understanding of nanomechanical effects during the formation of micro- or nanocracks or defects will be the key for the definition of nanomechanical design rules.

The aim of this work is the development of an in-situ deformation measurement technique which allows displacement measurements at the micro and nanoscale.

Therefore, the so-called digital image correlation (DIC) method which was established as a micromechanical analysis tool by the group of Michel [2] will be adapted to scanning probe microscopy (SPM) images.

In a second step of this work, deformation measurement results at a crack tip will be used to evaluate fracture mechanical properties of a polymeric material. The analyzed polymer is a cyanate ester resin which is a typical material in microelectronics applications. The group of Bauer developed extensive data base on this type of thermoset material [3]. This enables the comparison of more or less macroscopic properties to the nanoscaled measurements of this work.

Finally, concepts of combined finite element/experiment approaches will be introduced. The approaches are to point out possible strategies for answering nanotechnological reliability problems.

Chapter 2

Theoretical and Experimental Background

A promising approach for future reliability concepts for newly developed nanomaterials and micro/nano-electronics devices is the combination of experimental and numerical techniques. With the driving force of nanotechnology the development of innovative experimental methods and simulation technologies has become major tasks for current research.

At the present time, there is a variety of measurement techniques which are able to provide data for reliability determination or the development of thermomechanical material models. In the following, the most important measurement approaches will be introduced and analyzed by their capability for nanomechanical analysis of materials and nanodevices. The main emphasis is laid on measurement techniques focusing on the detection and characterization of material defects and cracks.

Within the frame of this work, the experimental concepts are verified by numerical simulations based on the finite element method (FEM). Therefore, an overview of the applied numerical concepts is given in this chapter. It has to be noted that the general question of applicability of FEM to nanomechanical issues is also a broad field of research which will not be addressed in this work.

2.1 State of the Art of Submicron In-Situ Loading Tests

The methods of choice for determination of thermomechanical material properties on the submicron scale are scanning probe microscopy (SPM), high voltage electron microscopy (HVEM), or transmission electron microscopy (TEM) measurements. HVEM in-situ loading is carried out by several research groups [4–6]. The method is well suited for the measurement of deformation fields. However, it will not be used within the frame of this work because a 3-D measurement technique which is seen as a target for in-situ loading tests is easier to acquire with SPM methods. TEM has the disadvantages that only very thin specimens can be analyzed and that extensive specimen preparation is required.

Moreover, the thin film effects dominate the deformation behavior at the crack tip. Nevertheless, loading of specimens in the TEM is carried out by several research groups [7–9]. This work concentrates on SPM methods. With an appropriate loading device, in-situ thermomechanical loading of complete electronic components is the key for understanding the relevant failure modes on the submicron scale.

In the following, an overview of the present research activities on defect and crack analysis on the basis of SPM techniques is given. Furthermore, the technique of digital image correlation (DIC) is discussed. Following the trends discussed above, the work of other research groups on SPM based image correlation is also presented.

2.1.1 Experimental Mechanics by Scanning Probe Microscopy

Reliability concepts for technological systems are based on the understanding of failure mechanisms within a material or material interface. Material defects and micro- or nano-cracks caused by manufacturing processes or during thermomechanical cycling over the lifetime of a system are the starting points for crack propagation finally resulting in a failure of the system. Therefore, the understanding of crack initiation and propagation is a vital issue for reliability determination of newly developed micro- or nanotechnological systems. Due to the fact that the running of a crack is driven by the stress/strain field at the crack tip detailed experimental studies at the vicinity of the crack tip are essential.

Most of published experimental approaches on thermally and/or mechanically induced deformation characterization are qualitative and semi-quantitative analyses making use of surface profiles taken from SPM topography scans. Without claiming for completeness, some of the relevant research activities are given exemplary thereby addressing different material classes.

The development of slip bands and protrusions in strain controlled fatigue tests on polycrystalline copper and stainless steel was studied by Cretegnny et al. [10, 11]. A criterion for crack nucleation was developed based on the length, height, count, and orientation of surface features taken from atomic force microscopy (AFM) images of copper specimens.

In-situ AFM straining experiments on magnetic thin films under tension were carried out by Bobji et al. [12, 13] showing nucleation and growth of microcracks in magnetic tapes. Crack width and crack spacing were measured from AFM scan data.

Near-tip stress field of a crack in hot-pressed silicon carbide during 3-point bending was examined by Kinoshita [14]. The topographies obtained in the AFM observations indicated that the near-tip stress singularity produced a depression which can be used as a measure for stress singularity.

Komai et al. [15] analyzed fracture surfaces of single-crystal silicon microelements subjected to quasi-static and fatigue three-point bending tests. Height profiles of AFM topography scans were used for crack detection.

The effect of the curing temperature on the morphology of a thermoplastic modified cyanate ester resin was studied by Marieta et al. [16]. A bisphenol-A dicyanate (DCBA) resin was modified with bisphenol-A polysulfone (PSU) at a concentration of 15wt%. Mixtures,

postcured at the same conditions, were precured at various temperatures. Fracture surfaces of three-point bending tests were analyzed by different SPM modes. Thermoplastic phases and the thermoset matrix were easily to be distinguished in images taken by friction or phase mode. In another paper [17] Marieta et al. applied these imaging techniques to a diglycidyl ether of bisphenol-A (DGEBA) epoxy matrix modified with polymethylmethacrylate (PMMA) showing similar results.

Creuzet et al. [18] studied the fracture behavior of soda lime glass. The role of plasticity at the crack tip is shown to demonstrate the need for a modification of the Griffith criterion. Intrinsic defects acting as stress concentrators could not be identified by AFM analysis.

An AFM analysis of the atomic structures of unloaded and loaded crack tips in the (001) surface of muscovite mica was carried out by Guan et al. [7]. A disorder zone with a width of about 8nm ahead of a loaded crack tip was observed. Outside the disorder zone a normal elastic region was found. The question whether the dislocations emitted from the crack tip or not is not solved in the paper. Critical stress intensity factors are evaluated with the equation of Göken [19].

Crack tip blunting by dislocation emission and unstable crack propagation of NiAl single crystals in the AFM was studied by Göken et al. [19, 20]. NiAl serves as a model alloy for the mechanical behavior of intermetallic compounds. A model of plastic crack opening displacement (COD) was used for fracture toughness evaluation, but the calculated values for the stress intensity factor were not in good agreement with comparable measurements of other research groups. The estimation by plastic COD generally led to lower values than those obtained from load-displacement curves [20]. The depression in front of the crack tip was also calculated on the basis of analytical equations and no good agreement was found to AFM measurements. It was shown that three-dimensional FE calculations were necessary [21]. Vehoff et al. [22] show that for single crystals dynamic computer simulations for the prediction of toughness do not agree with the measured toughness. For the measured slip plane length the simulations predict a much larger toughness.

In addition, Göken et al. [23] used optical interference microscopy (OIM) which has a larger lateral scale than AFM but a similar vertical resolution for measurements of the vertical depression at the crack tip. The results were compared to FEM calculations. Stress intensity factors were determined from the elastic displacements in vertical direction around the crack tip. However a complete comparison and discussion of the FEM data and the measurements is not published so far.

Parallel to the research at in-situ loading experiments, advanced SPM modes such as atomic force acoustic microscopy (AFAM) [24–26] and ultrasonic force microscopy (UFM) [27–30] are becoming powerful techniques for the determination of material properties on the nanoscale.

Summarizing one can say that a satisfying model for the crack tip behavior in the very vicinity of the crack tip is not available for most of the discussed material classes. There is a need for deformation measurement technique especially for crack tip analysis.

2.1.2 Micro Deformation Measurement Techniques

As discussed in the previous section, the determination of stress/strain fields at the crack tip is the key for a successful description of a failure mechanisms of a technological system. Thus, the measurement of stresses and strains at the surface of materials is a widely developed field in material science. Today, a variety of deformation measurement techniques are available, such as photoelasticity [31–34], Moiré and speckle interferometry [35], stereo imaging techniques [36, 37] and digital image correlation [2, 38]. Most of these techniques are highly specialized in specific research fields or make use of an extraordinary experimental setup. The imaging techniques vary from video or CCD cameras, optical microscopy, white light microscopy, scanning electron microscopy (SEM), laser scanning microscopy (LSM) to scanning probe microscopy (SPM).

Nowadays, for the special case of microelectronic applications three methods of in-situ measurement techniques are successfully employed by several research groups i.e. Moiré, speckle techniques and digital image correlation. In the following, the principles of these methods are discussed the emphasize being laid on the method of digital image correlation which is the method of choice in this work.

Moiré and Speckle Techniques

In the application of the *Moiré* technique it has to be distinguished between *geometric* and *interferometric Moiré*. Geometric Moiré is the intensity superposition phenomenon when two Ronchi gratings are superimposed whereas interferometric Moiré is the amplitude and phase interference of two coherent light beams emanating from a diffraction grating on the specimen surface. While the basic phenomena are different, the form of the resulting field equations are identical [39]. Both Moiré methods resort to the deviation from a reference grating pitch as a measure of deformation. If deformed gratings are superimposed with corresponding reference gratings, Moiré fringes result. With the knowledge of the grating parameters displacement contours can be calculated from the fringes.

Matsumoto [40] originally proposed the use of Moiré interferometry in 1972. But its development and application did not begin until the 80s and was initiated by Post [41] using optical Moiré techniques. In the following, Moiré methods were established in scanning electron microscopy [42, 43]. Today the development of the Moiré method towards nanometer resolution is carried out by Asundi and co-workers [35, 44–46]. Gratings of 10^6 lines/mm are applied to generate AFM Moiré. First applications were shown at integrated circuit (IC) packages. Furthermore, the lattice of mica atoms is utilized as gratings for nano Moiré measurements. The latest development is a deformation measurement Moiré approach based on focused ion beam (FIB) images [47].

Speckle methods utilize a random pattern of speckles to register deformation. Information in terms of displacement is obtained through correlation between two speckle patterns. It is sometimes referred to as the speckle Moiré method, because the speckle pattern may be considered as a random grating with all orientations and a band limited spectrum of grating pitch [48]. Through the process of optical (or digital) spatial filtering in form of Fourier decomposition, an equivalent grating pitch with a specific orientation can be evaluated.

Regarding the speckle techniques it has to be distinguished between coherent [49] and incoherent methods. Coherent speckle patterns results from the illumination of an optically rough surface with a coherent laser light whereas incoherent speckles are artificially produced. For example, it can be created by spraying black paint from an aerosol onto a white surface.

Summarizing the application of Moiré and Speckle techniques to actual questions of material research it can be concluded that their capability is also given for submicron measurements. However, due to the fact that digital image correlation techniques are easier to handle they become a powerful deformation measurement technique.

Digital Image Correlation

The digital image correlation technique is a method of digital image processing. Digitized images of the analyzed objects in at least two or more different states (e.g. before and after mechanical and/or thermal loading) have to be obtained with an appropriate imaging technique. Displacement fields are extracted by computer aided comparison of gray scale images (or image segments) by means of the application of a correlation algorithm.

Generally, correlation algorithms can be applied to images extracted from various sources. Digitized photographs or video sequences but also images from e.g. optical microscopy, SEM, LSM or SPM are suitable for the application of digital image correlation.

The method was introduced by Peters and Ranson [50] and Sutton et al. [38] who used digital image correlation on laser speckle images. Improvements of the method were published in several papers [51–53]. By the application of stereo imaging an extension towards three-dimensional displacement fields was developed by Luo et al. [36].

During the last two decades digital image correlation methods were established by several research groups. Examples from different fields of applications can be found in various publications, e.g. in [52–65]. Early attempts to acquire high resolution SEM images for subsequent deformation analyses were made by Davidson [66] with the application of the so-called DISMAP system which allowed the digitizing of photographic micrographs. In modern SEM equipment however images are already "captured" digitally so that correlation algorithms are applied directly to them. This approach has been chosen by various research labs and is described in several publications [2, 37, 67–69]. In the group of Michel the application of SEM images for deformation analysis on thermomechanically loaded electronics packages was established as the so-called **microDAC** method i.e. **micro Deformation Analysis** by means of **C**orrelation algorithms [2].

The latest development of the DIC methods is the extension towards nanometer scale measurements. The application of scanning probe microscopy for image acquisition is used by the group of Knauss [64, 70–72] and Michel and co-workers [73–76] who named their technique **nanoDAC**. Details will be discussed in Sect. 2.1.3.

The reason for the success of the DIC method, especially in the comparison to laser interferometric or Moiré methods, is based on several advantages:

- In many cases, only relatively simple low-cost hardware is required (optical measurements) or already existing microscopic tools like SEM and SPM can be utilized without any changes.

- Once implemented in a well designed software code, the correlation analysis of gray scale images is user friendly and easy to understand in the measuring and post-processing process.
- For optical micrographs, no special preparation of the objects under investigation is needed at all. For low magnifications, required standards for the experimental environment (e.g. vibration isolation, stability of environmental parameters like temperature) are not as high as in laser based measurements.
- The application and cumbersome preparation of object grids is not necessary.
- According to its nature the method possesses an excellent down-scaling capability. By using microscopic imaging principles, also very small objects can be investigated.

Therefore, correlation analysis of gray scale images is predestinated for qualitative and quantitative measurement of micro and nanomechanical properties.

2.1.3 The Combination of SPM Methods and Digital Image Correlation

The development of a deformation measurement technique based on scanning tunneling microscopy (STM) and digital image correlation was introduced by the group of Knauss [77]. For the measurements, a new STM system was designed to be coupled to a mechanically deforming specimen. Based on the two-dimensional DIC algorithm developed in the publications of Sutton and Luo et al. [36, 38, 51, 78] a modification of the DIC method towards three-dimensional deformation measurement was established [77]. Accuracy tests show that an in-plane displacement error of ± 0.08 pixel or ± 2.4 nm and an out-of plane displacement error of ± 0.75 nm could be achieved by the STM-DIC method. On an STM image of $10 \times 10 \mu\text{m}$ the total possible in-plane displacement resolution of the technique was 4.8 nm, whereas the total out-of plane displacement resolution was 1.5 nm [79]. STM-DIC based results were published on the deformation of a uniaxial stressed PVC specimen [70]. The combination of atomic force microscopy and digital image correlation was developed by the research groups of Knauss and Michel. The first results were reported on crack tip field measurements of a thermoset material by Vogel and Michel [73, 80] followed by an article of Chasiotis and Knauss [64] on uniaxial tensile tests on polycrystalline silicon. An overview of the progress of the group of Knauss is given in [72].

From the above mentioned publications the following facts on AFM based digital image correlation can be summarized:

- The AFM is a suitable image acquisition tool for the application of digital image correlation. With the application of the AFM for micro- and nanomechanical deformation analysis the foundation is laid for a detailed evaluation of the limits and possible break down of continuum mechanics in the nanometer region.

- Problems encountered during data acquisition are the long scanning times hysteresis and creep effects of the piezo scanning tube. Nevertheless, new developments on scanning probe techniques and DIC software tools due to the demand in nanotechnology research will provide new measurement features enlarging the potential of the SPM based DIC analysis.

With the development of SPM-based DIC techniques, future failure and reliability problems on nanoscaled particles and material interfaces will be addressed. Thereby, the trend from micro electronic mechanical systems towards nano electronic mechanical systems is supported by an appropriate measurement technique.

2.2 The Method of Digital Image Correlation

The basic idea of the DIC algorithms results from the fact that images commonly allow to record local and unique object patterns within the more global object shape and structure. These patterns are more or less stable if the objects are deformed by mechanical or thermal loads. Figure 2.1 and 2.2 show two examples of images taken by scanning electron microscopy and scanning force microscopy.

Markers indicate typical local pattern of the images. In most cases, these patterns are of stable appearance, even when severe load is applied to the specimens. In spite of the presence of strong plastic, viscoelastic or visco-plastic material deformation, local patterns can be recognized after loading, i.e. they can function as a local digital marker for the correlation algorithm.

2.2.1 Cross Correlation Algorithms on Gray Scale Images

The cross correlation approach is the basis of the DIC technique. A scheme of the correlation principle is illustrated in Fig. 2.3. Images of the object are obtained at a reference load state 1 and at a different second load state 2. Both images are compared with each other using a cross correlation algorithm. In the image of load state 1 (reference) rectangular search structures (kernels) are defined around predefined grid nodes (Fig. 2.3, left). These grid nodes represent the coordinates of the center of the kernels. The kernels themselves act as gray scale pattern from load state image 1 that have to be tracked, recognized and determined by its position in the load state image 2. In the calculation step the kernel window ($n \times n$ submatrix) is displaced inside the surrounding search window (search matrix) of the load state image 2 to find the best-match position (Fig. 2.3, right).

This position is determined by the maximum value of the cross correlation coefficient, K , which is calculated for all possible kernel displacements within the search matrix. The computed cross correlation coefficient K compares gray scale intensity patterns of load state images 1 and 2. K is equal to

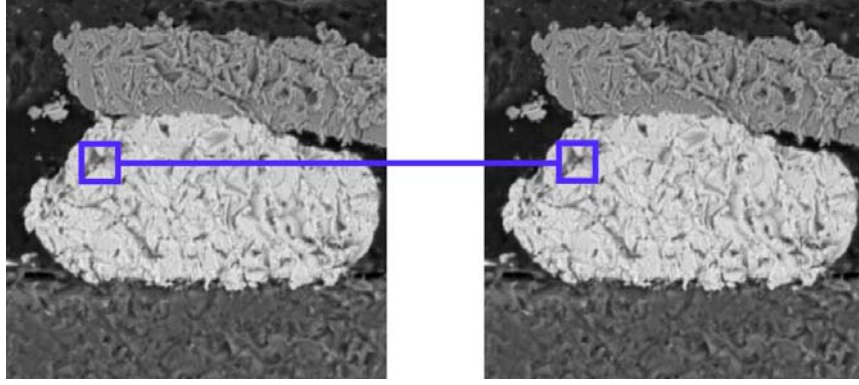


Figure 2.1. Appearance of local image structures (patterns) during specimen loading; SEM images of flip chip gold bump image size $100 \times 100 \mu\text{m}$; (**left**) at room temperature, (**right**) at 125°C .

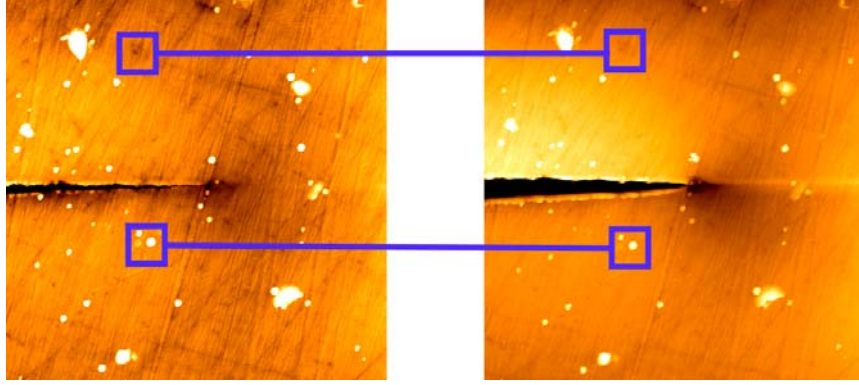


Figure 2.2. AFM topography image of a crack in a thermoset polymer material for different crack opening displacements, scan size $15 \times 15 \mu\text{m}$.

$$K_{i',j'} = \frac{\sum_{i=i_0}^{i_0+n-1} \sum_{j=j_0}^{j_0+n-1} (I_1(i,j) - M_{I_1}) (I_2(i+i',j+j') - M_{I_2})}{\sqrt{\sum_{i=i_0}^{i_0+n-1} \sum_{j=j_0}^{j_0+n-1} (I_1(i,j) - M_{I_1})^2 \sum_{i=i_0}^{i_0+n-1} \sum_{j=j_0}^{j_0+n-1} (I_2(i+i',j+j') - M_{I_2})^2}} \quad (2.1)$$

where $I_{1,2}$ and $M_{I_{1,2}}$ are the intensity gray values of the pixel (i, j) in the load state images 1 and 2 and the average gray value over the kernel size, respectively. The kernel displacement within the search matrix of load state image 2 is indicated by i' and j' . Assuming quadrangle kernel and search matrix sizes $K_{i',j'}$ values have to be determined for all displacements given by $-(N-n)/2 \leq i', j' \leq (N-n)/2$. The described search algorithm leads to a two-dimensional discrete field of correlation coefficients defined at integer pixel coordinates (i', j') . The discrete field maximum is interpreted as the location, where the reference matrix has to be shifted from the first to the second image to find the

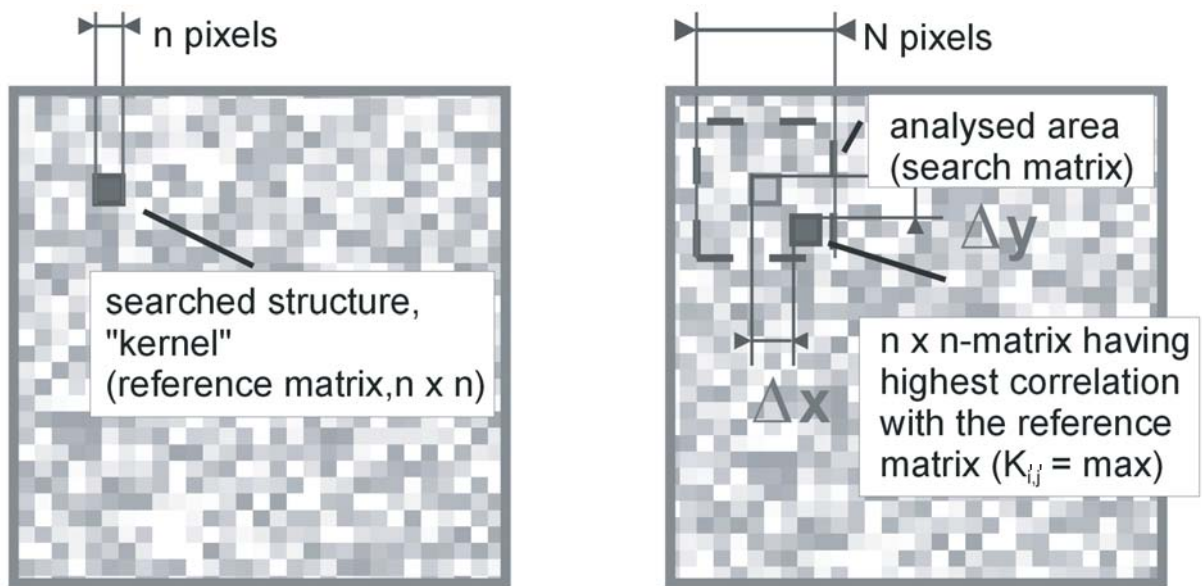


Figure 2.3. Displacement evaluation by cross correlation algorithm; **(left)** detail of a reference image at load state 1; **(right)** detail of a image at load state 2; [81].

best matching pattern. Figure 2.4 shows an example of the correlation coefficients inside a predefined search window.

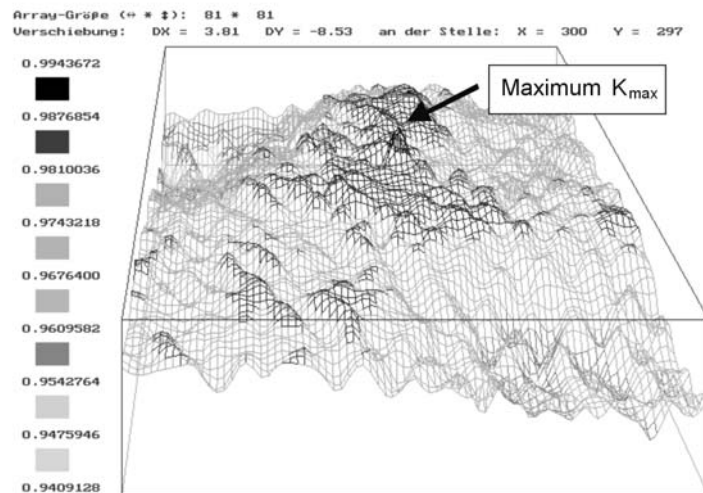


Figure 2.4. Discrete correlation function $K_{i',j'}$ defined at integer (i', j') coordinates; the maximum of the coefficient of correlation is marked by an arrow [81].

With this calculated location of the best matching submatrix an integer value of the displacement vector is determined.

2.2.2 Subpixel Analysis for Enhanced Resolution

As described in the previous section, the cross correlation algorithm determines the displacements in the form of integer pixel coordinates. For the calculation of the displacement field with a higher accuracy, the displacement evaluation has to be improved. Different research groups [72, 73] reported the application of algorithms improving the accuracy of the cross correlation technique. In a second calculation step, special subpixel algorithms are used to achieve higher displacement value resolution. The presumably simplest and fastest procedure to find a value for the non-integer subpixel part of the displacement is implemented by parabolic fitting. The algorithm searches for the maximum of a parabolic approximation of the discrete function of correlation coefficients in the close surrounding of the maximum coefficient $K_{max,discrete}$. The approximation process is illustrated in Fig. 2.5

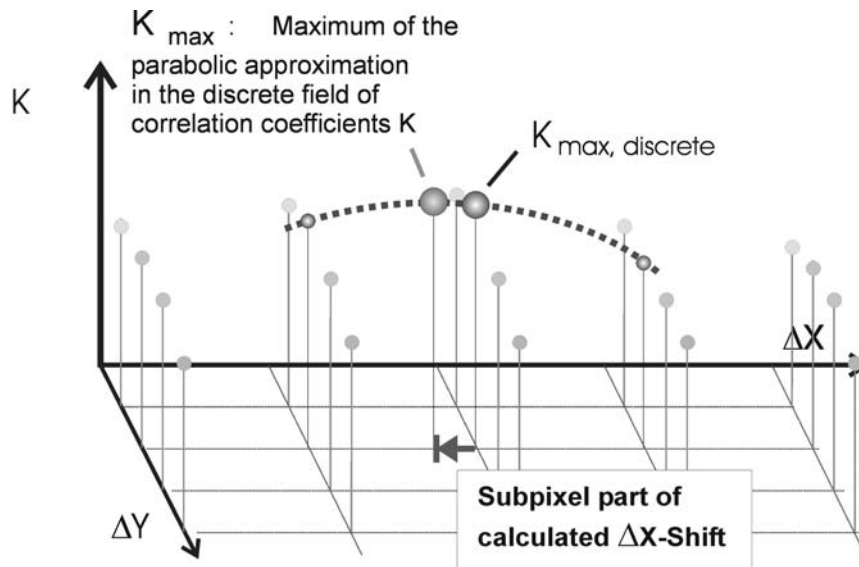


Figure 2.5. Principle of the parabolic subpixel algorithm [81].

The location of the maximum of the parabolic function defines the subpixel part of the displacement. In most cases (on CCD camera and SEM images) this algorithm allows to get a subpixel accuracy of about 0.1 pixel. With more advanced algorithms accuracies of up to 0.01-0.02 pixel for common 8 bit digitized images are possible [81]. However, it has to be stated that the overall accuracy depends on the image source, signal noise, stability during image caption and on the contrast of the pixels of the correlation kernel to a large extent.

2.2.3 Results of Digital Image Correlation

The results of the two-dimensional cross correlation and subpixel analysis in the surroundings of a measuring point primarily are the two components of the displacement vector.

Applied to a set of measuring points (e.g. to a rectangular grid of points with user defined pitches), this method allows to extract a complete in-plane displacement field. In the simplest way the results can be displayed as a numerical list which can be post-processed using standard scientific software codes. Commonly, graphical representations such as vector plots, superimposed virtual deformation grids or color scale coded displacement plots are implemented in commercially available or in in-house software packages. Figure 2.6 shows two typical examples of graphical presentations of the results at an AFM image.

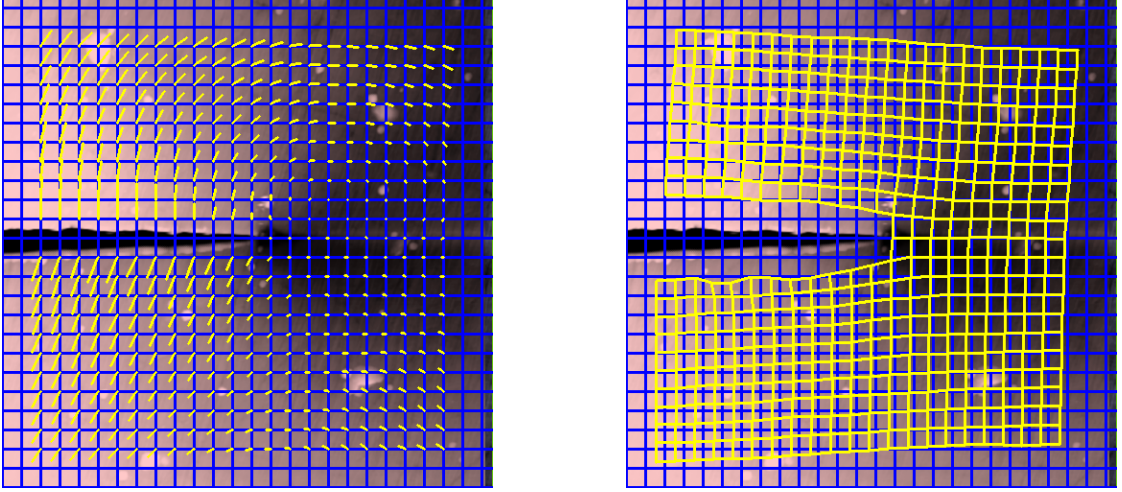


Figure 2.6. *Digital image correlation results derived from AFM images of a crack tip, scan size $15 \times 15 \mu\text{m}$; (left) Image overlaid with user defined measurement grid and vector plot of displacements; (right) Image overlaid with user defined measurement grid and deformed measurement grid; (displacement vector and deformed grid presentation are enlarged with regard to the image magnification).*

Finally, taking numerically derivatives of the obtained displacement fields $u_x(x, y)$ and $u_y(x, y)$ the in-plane strain components ε and the local rotation angle ρ are determined:

$$\varepsilon_{xx} = \frac{\partial u_x}{\partial x}, \quad \varepsilon_{yy} = \frac{\partial u_y}{\partial y}, \quad \varepsilon_{xy} = \frac{1}{2} \left(\frac{\partial u_x}{\partial x} + \frac{\partial u_y}{\partial y} \right), \quad \rho_{xy} = \frac{1}{2} \left(\frac{\partial u_x}{\partial x} - \frac{\partial u_y}{\partial y} \right) \quad (2.2)$$

Derivation is included in some of the available correlation software codes or can be performed subsequently with the help of mathematical software packages.

2.2.4 Accuracy

The accuracy of the displacement measurement is defined by the imaged area dimensions at the object in horizontal x - and vertical y -direction, $l_{x,y}$, the pixel resolution of the image in x - and y -direction, $m_{x,y}$ and the subpixel shift resolution k . It is given by, [81]:

$$\delta u_{x,y} = (l_{x,y}/m_{x,y})k \quad (2.3)$$

The subpixel shift resolution k is a measure for the available displacement resolution and strongly depends on the experimental conditions, the quality of the images obtained in the experiment (e.g. noise, sharpness of pixel information) and the quality of the applied software algorithms. The value for k varies in most of the relevant cases between 1/4 to 1/100 pixel [81]. For calculation results obtained by statistical evaluation of multiple point measurements (e.g. rigid body displacement calculated as the mean value of shifts measured at multiple points, linear elastic strain calculated from the slope of a regression line) resolution equivalents to 0.01 pixel and better are reached, although the correlation software itself does not provide this level of accuracy. Assuming values of a SPM large scale scan size of $l_x, l_y = 50 \mu\text{m}$, a scan resolution $m_x, m_y = 512$ and a measurable subpixel shift $k = 0.2$ (estimated), a measurement resolution of a single one-point displacement value down to 20 nm can be obtained with scanning probe microscope applications (Eqn. 2.3). With a scansize of $2.5 \mu\text{m}$, a resolution of 1 nm is a realistic value.

2.3 Fracture Mechanics Approach

From a macroscopic, continuum mechanics point of view a crack is defined as infinitely sharp and is, therefore, a geometric singularity. The loading of a crack can be applied by three different *modes*, as illustrated in Fig. 2.7.

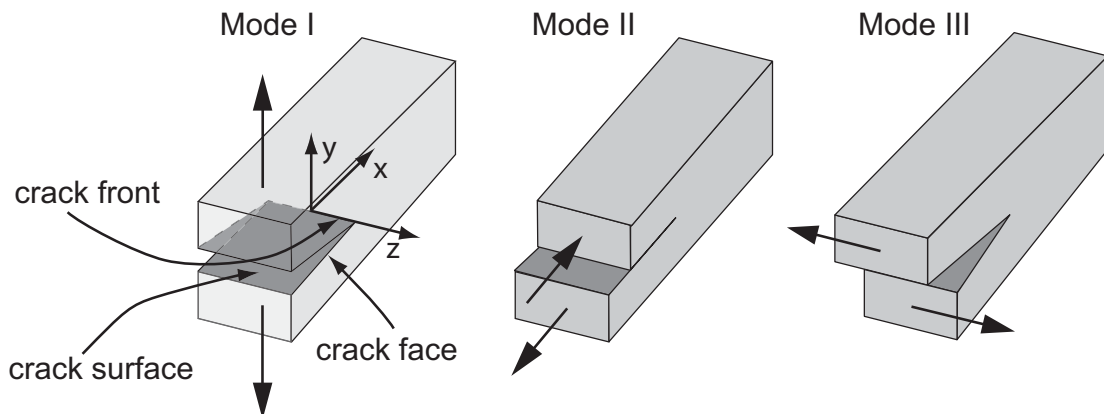


Figure 2.7. Principle loading modes that can be applied to a crack.

In mode I, the load is applied normal to crack plane introducing a symmetric separation of the upper and lower crack surfaces. Mode II can be described as in-plane shear loading and mode III as out-of plane shear. The crack can be loaded in one of these modes or in a mixture of two or three modes. In an actual application, especially at a crack of a microelectronic component, these modes are difficult to separate from each other. Moreover, the mode type may change during a single load cycle, over service time or during crack growth.

For the linear elastic fracture mechanics approach (LEFM) on the basis of continuum mechanics the size of the *process zone* is of great significance. The process zone is the region

in the vicinity of the crack front (2D: crack tip) were micro or nanoscopically small damage and reordering processes prevail. Metals, for example, deform plastically which causes crack tip blunting. The occurring yielding process is dominated by dislocation motion along slip planes. Polymers, however, have a different microscopic fracture behavior. Depending on the molecular structure of the polymer chain scission, disentanglement of polymer chains, shear yielding and crazing are dominating processes at the highly stressed crack tip (a detailed discussion on polymer fracture is given in Sect. 3.1). Nevertheless, the behavior of the process zone cannot be described by continuum mechanics theory. For the consistent description of the stress state by LEFM it has to be assumed that the process zone is sufficiently small compared to the macroscopic geometry of the cracked body.

Fundamental for understanding fracture behavior of a cracked body is the crack tip field i.e. the stress-strain field in the surrounding of the crack tip. Especially in the area of microelectronics where the dimensions of functional and passive layers or other components are becoming smaller with every newly developed process technology the understanding of the deformation field around a defect or crack is of primary interest.

Therefore, the crack tip field of a cracked body with isotropic and linear elastic material behavior under static load will be addressed in the following section.

2.3.1 Crack Tip Field Analysis

A two-dimensional body with a straight crack as illustrated in Fig. 2.8 can be analyzed assuming a plane strain or plane stress configuration. For the mathematical derivation of the crack field it is convenient to introduce a polar coordinate system (r, θ) with its origin at the crack tip. The derived stress/strain field description can be transferred to cartesian coordinates (x,y) by coordinate transformation. For this case the stresses at an area element is defined as illustrated in Fig. 2.8.

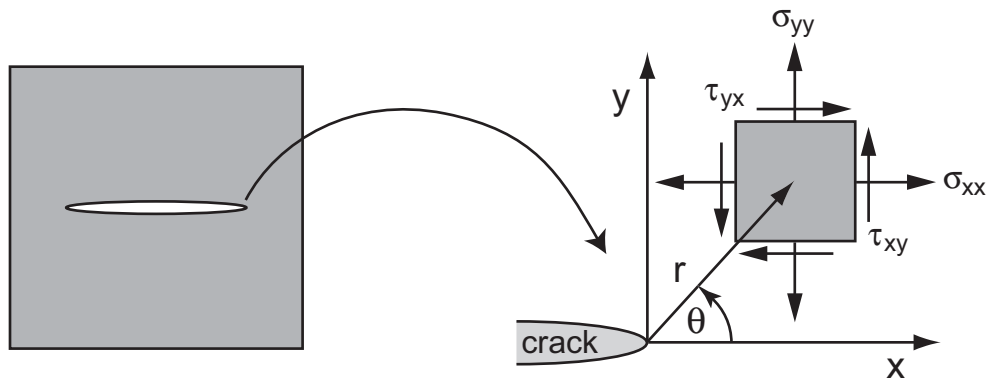


Figure 2.8. Body with through-thickness crack; definition of coordinate axes in cartesian coordinate system (x,y) .

A specific crack tip loading according to the defined modes produces a $1/\sqrt{r}$ stress singularity at the crack tip with a mode depended stress intensity factor, K . Thus the asymptotic stress fields at a crack tip can be written as [82]:

$$\lim_{r \rightarrow 0} \sigma_{ij}^{(n)} = \frac{K_n}{\sqrt{2\pi r}} f_{ij}^{(n)}(\theta) \quad (2.4)$$

where K_n describes the stress intensity factors according to the relevant loading mode n (I, II or III), and f_{ij} is a dimensionless function. For mode I crack opening the displacement field at the crack tip is described by:

$$u_x = \frac{K_I}{2\mu} \sqrt{\frac{r}{2\pi}} \cos \frac{\theta}{2} \left(\kappa - 1 + 2 \sin^2 \frac{\theta}{2} \right) \quad (2.5)$$

$$u_y = \frac{K_I}{2\mu} \sqrt{\frac{r}{2\pi}} \sin \frac{\theta}{2} \left(\kappa + 1 - 2 \cos^2 \frac{\theta}{2} \right) \quad (2.6)$$

where μ is the shear modulus of the material and κ is defined as

$$\kappa = 3 - 4\nu \quad \text{for plane strain, and} \quad (2.7)$$

$$\kappa = (3 - \nu)/(1 + \nu) \quad \text{for plane stress,} \quad (2.8)$$

where ν is the Poisson's ratio.

In most of the practical cases of a cracked body, the three-dimensional description of the fracture problem is necessary. In general, a curved crack front has to be treated in a three-dimensional manner. Examples are penny-shaped inner crack problems or semi-elliptical surface cracks. An exact description of a crack with a straight crack front in a plate of finite thickness also requires a three-dimensional analysis because the state of stress varies along the z -coordinate of the crack front (compare to Sect. 4.3).

2.3.2 K-Concept

Fundamentals

We consider the most relevant crack loading configuration which is the pure mode I crack opening. As described in the previous section, the crack tip field is characterized by the stress intensity factor K_I . However Eqn. 2.4 leads to an infinite stress value if the distance from the crack tip, r , reduces to 0. Real materials do not withstand infinite stress. Metals respond with the formation of a plasticity zone where polymers show crazing in order to achieve a relaxation of the stresses. The K -concept is only valid if the size of that *inelastic* region in the surrounding of the crack tip is sufficiently small. Then the K -dominated area lies within an inner radius, r_p , and an outer radius, R as illustrated in Fig. 2.9.

Outside the radius R higher order terms of the stress solution have to be taken into account. The inner bound of the K -dominate zone is given by r_p where the increasing stresses cause plastic deformation. Described in a more general term, the material reacts with an *inelastic deformation* compared to the elastic deformation (linear elasticity theory) of the K -dominated zone, [83].

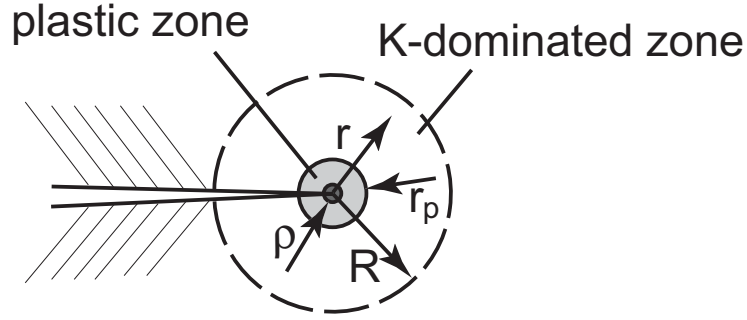


Figure 2.9. Crack tip behavior under the assumption of the K -concept [83].

With the assumption that the region of the inelastic and process zone (indicated by the radius ρ) is small compared to the K -dominated zone ($\rho, r_p \ll R$) the behavior at the crack tip can be described by the K -factor. This is the underlying theory of the K -concept. The stress intensity factor allows the definition of a fracture criterion: The crack extension occurs if a material dependent critical stress intensity factor, K_c , prevails at the crack tip. The critical stress intensity factor is called the fracture toughness. It is a material property and, therefore, independent of the geometry of the specimen or structure.

Measurement of K-Factor

For the measurement of the stress intensity factor the singularity at the crack tip of a test specimen have to be equivalent to the underlying theoretical approach. Most of the closed-form K solutions directly derived from stress functions are only valid for cracks in infinite plates. For usual test specimens with finite dimensions and crack sizes similar to the boundary geometries of the specimen closed-form solutions are not available. However, the influence of the geometry on the stress field can be corrected by appropriate geometry functions.

In this work the standardized CT-specimen (CT: compact tension) corresponding to ASTM 5045, [84], was used for the experimental fracture tests. The CT-specimen and the nomenclature of the geometry parameters are illustrated in Fig. 2.10.

The stress intensity factor for the CT-specimen is defined by:

$$K_I = \frac{F}{B\sqrt{W}} f(\alpha) \quad (2.9)$$

where F is the applied load and f is the geometry function of the non-dimensional crack length, α , with $\alpha = a/W$

$$f(\alpha) = \frac{2 + (\alpha)}{(1 - \alpha)^{3/2}} = [0.866 + 4.64(\alpha) - 13.32(\alpha)^2 + 14.72(\alpha)^3 - 5.6(\alpha)^4] \quad (2.10)$$

The specimens have to be prepared with a pre-crack initiated by a cyclic loading (typically used for metals) or tapping of a razor blade (for brittle polymers). The thickness, B , of the

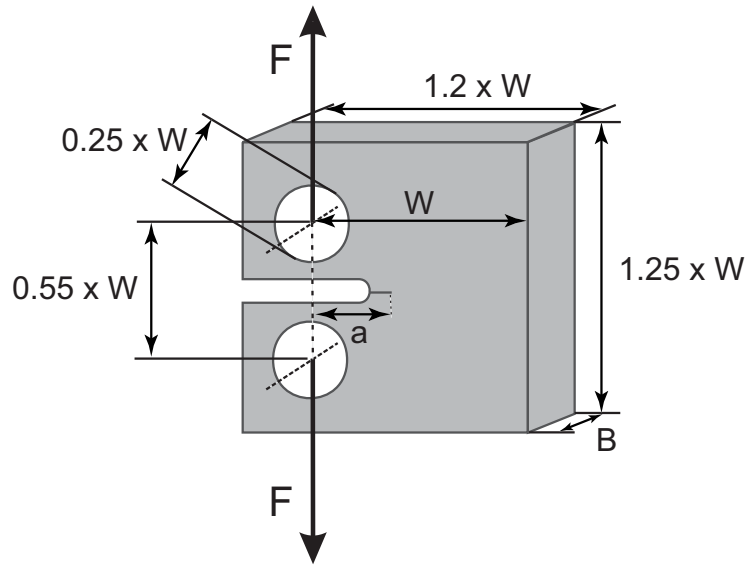


Figure 2.10. *CT-specimen with geometry according to ASTM D5045 [84].*

specimen have to be sufficiently large to ensure a state of plane strain over a sufficiently large portion of thickness B .

2.3.3 Energy Release Rate

Irwin [85] has introduced the concept of energy release rate \mathcal{G} which is the available energy dW for an increment of crack extension dA :

$$\mathcal{G} = -\frac{d\Pi}{dA} \quad (2.11)$$

\mathcal{G} is the change of potential energy Π with the crack area A during crack extension. The energy release rate is a measure for the crack tip load and the tendency of crack extension. It is the basis for numerical determination of fracture mechanical properties utilizing fracture mechanical integral concepts developed by Rice [86].

In case of a through crack in an infinite plate subjected to a tensile stress and linear elastic material behavior the energy release rate can be related to the stress intensity factor through:

$$\mathcal{G} = \frac{K_I^2}{E} \quad (2.12)$$

For plane strain configurations E have to be replaced by $E/(1 - \nu^2)$.

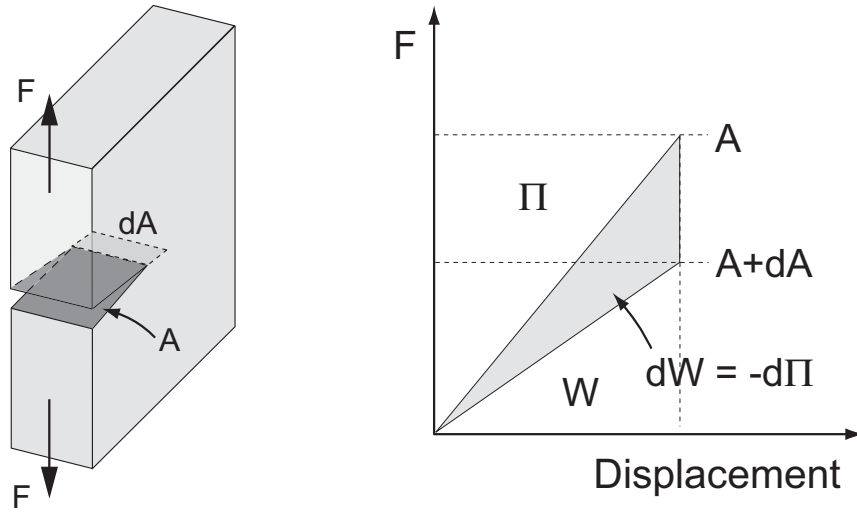


Figure 2.11. Energy release rate.

2.4 Numerical Fracture Mechanics Utilizing Integral Concepts

Besides the K -factor and the energy release rate \mathcal{G} the J -integral is another parameter describing the fracture behavior of a material. For linear elastic fracture mechanics \mathcal{G} and J are equivalent and K can be determined from \mathcal{G} or J . Despite the K - and \mathcal{G} -concept the J -integral is also valid for inelastic material behavior.

The J -integral was proposed by Rice [86] and is defined by:

$$J = \int_{\Gamma} \left(w dy - T_i \frac{\partial u_i}{\partial x} ds \right) \quad (2.13)$$

where Γ is a counter-clockwise path around the crack tip, w is the strain energy density, T_i are components of the traction vector and ds is a length increment of the contour Γ . The strain energy density is defined by

$$w = \int_0^{\varepsilon_{ij}} \sigma_{ij} d\varepsilon_{ij} \quad (2.14)$$

where σ_{ij} and ε_{ij} are the stress and strain tensors, respectively, and the components of the traction vector are given by

$$T_i = \sigma_{ij} n_j \quad (2.15)$$

where n_j are the components of the unit vector normal to Γ .

Another advantage of the J -integral is its invariant behavior according to the chosen contour around a crack tip, so that a relatively coarse mesh can be used in finite element based simulations. With the assumption of elastic material behavior the J -integral can be related to the K -concept by the equation:

$$J = \frac{1}{E}(K_I^2 + K_{II}^2) + \frac{1}{2\mu}K_{III}^2 \quad (2.16)$$

where E is the Young's modulus and μ is the shear modulus.

For the numerical calculation of the J -integral different methods were developed. Parks [87] and Hellen [88] suggested a virtual crack extension method which is based on a stiffness derivative formulation of selected elements surrounding the crack tip. The problem of this method is that the calculation involves cumbersome numerical differencing. Moreover, it is not suited to problems including thermal strain [82].

Another definition of the J -integral which is excellently suited for FEA was proposed by de Lorenzi [89, 90]:

$$J = -\frac{d\Pi}{dA} = \frac{1}{\delta A} \int_V \left[(\sigma_{ij}(F_{jk} - \delta_{jk}) - w\delta_{ik}) \frac{\partial \Delta x_k}{\partial x_i} \right] dV \quad (2.17)$$

where δA is an increase in the crack area generated by a virtual crack advance, V is the volume of the body, F_{jk} are the body forces, δ_{jk} Kronecker's delta and Δx_k is a mapping function which maps the body containing the crack into a body with a slightly increased crack length.

Figure 2.11 illustrates an incremental virtual crack extension. In a three-dimensional problem the J -integral may vary along the crack front (compare to Sect. 4.3).

The application of the J -integral as defined in Eqn. 2.13 is limited to elastic or plastic behavior, the deformation has to be monotone and cyclic loading is not allowed. For the description of inelastic material behavior (plasticity, creep) several integral concepts were developed. Table 2.1 summarizes the most important integral concepts for experimental material characterization and FE-based fracture mechanical problems on the field of microelectronics.

The C^* integral is defined by replacing strains of Eqn. 2.13 with strain rates, and displacements with displacement rates, where \dot{w} is the stress work rate (power) density. The C^* parameter is only valid for crack growth in the presence of global steady state creep. Materials with a sufficiently slow crack growth compared to growing creep zones spreading out throughout the specimen can be characterized by C^* [82].

Ghavifekr [91] proposed the generalized J -integral proposing a separation between elastic and inelastic (plastic, creep and thermal) components of the deformation gradient. The idea of this type of integral is the assumption that the crack can only be driven by an elastic process and only elastic energy can be released during crack propagation.

Table 2.1. *Advanced integral concepts*

Concept	Integral	Material
C^* [92, 93]	$C_1^* = \int_{\Gamma} (\dot{w}dy - T_i \frac{\partial \dot{u}_i}{\partial x} ds)$ $\dot{w} = \int_0^{\varepsilon_{kl}} \sigma_{ij} d\varepsilon_{ij}$	viscoplastic Goldman, Hutchinson, Landes, Begley 1975
\hat{J} [94]	$\hat{J}_1 = \int_{\Gamma} t_i \frac{\partial u_i}{\partial X_1} ds - \int_{\nu} \sigma_{ij} \frac{\partial u_{i,j}}{\partial X_1} d\nu$	plastic, viscoplastic Kishimoto, Aoki Sakata 1980
ΔT^* [95, 96]	$\Delta T^* = \int_{S-S_0} [\Delta W n_1 - (t_i + \Delta t_i) \Delta u_{i,1} - \Delta t_i u_{i,1}] ds$ $+ \int_{V-V_0} [\Delta \sigma_{ij} (\varepsilon_{ij,1} + \frac{1}{2} \Delta \varepsilon_{ij,1})] d\nu$ $- \int_{V-V_0} [\Delta \varepsilon_{ij} (\sigma_{ij,1} + \frac{1}{2} \Delta \sigma_{ij,1})] d\nu$	plastic, viscoplastic Atluri 1983

The generalized J -integral is given by

$$J_G = -\frac{d\Pi}{dA} = \frac{1}{\delta A} \int_V \left[(\sigma_{ij} (F_{jk}^{El.} - \delta_{jk}) - w^{El.} \delta_{ik}) \frac{\partial \Delta x_k}{\partial x_i} \right] dV \quad (2.18)$$

where only the elastic energy and the elastic deformation is considered in the calculation of the J_G -integral.

Chapter 3

Testing and Results

The experimental approach to nanostructured materials and components is the key for successful design of microelectronic devices of the future. Therefore, well established measurement techniques for the determination of material properties have to be combined with new highly specialized strategies. Macroscopic material properties determined from measurements at bulk materials are becoming more and more ineffective for FE-based prediction of life-time and system reliability.

In the following chapter, material testing by standard testing procedures and a newly developed deformation measurement technique on the micro to nanoscale will be discussed. The results are presented in correspondence with the applied testing techniques and methods.

Section 3.1 gives an introduction to the chosen polymeric material system which is employed as a model material for the experimental approaches. In Sect. 3.2 the viscoelastic material characterization is shortly described together with the obtained material description. The main emphasis of this chapter is laid on newly developed experimental methods which were the motivation of this work. Namely, the development and application of the *nanoDAC* method for micro- and nanoscaled deformation measurement (Sect. 3.4) and the research on the *Optical Crack Tracing* (OCT) system providing an advanced measurement technique for fracture mechanical parameters of polymers (Sect. 3.3) are discussed.

3.1 Polymeric Materials

3.1.1 Mechanical Behavior of Polymeric Materials

The mechanical behavior of polymers depends on various characteristic properties, such as the degree of polymerization, molecular weight, polydispersity, and the molecular structure. These measures can be controlled by production process parameters (time, temperature) and by added catalysts, compatibilizers, etc.

The possible molecular structures of the polymer chains which have a significant influence on the mechanical properties are illustrated in Fig. 3.1. Thermoplastic polymers consist of linear and branched chains. Typically, the polymer chains in an elastomer are organized in lightly cross-linked structures and are, therefore, capable to withstand large elastic strains.

Thermosets are highly cross-linked polymers consisting of a three-dimensional network structure. During the curing process the polymer chains solidifies into a cross-linked lattice. In contrast to a thermoplastic material this process is irreversible. Thermoset materials cannot be formed into a different shape after curing.

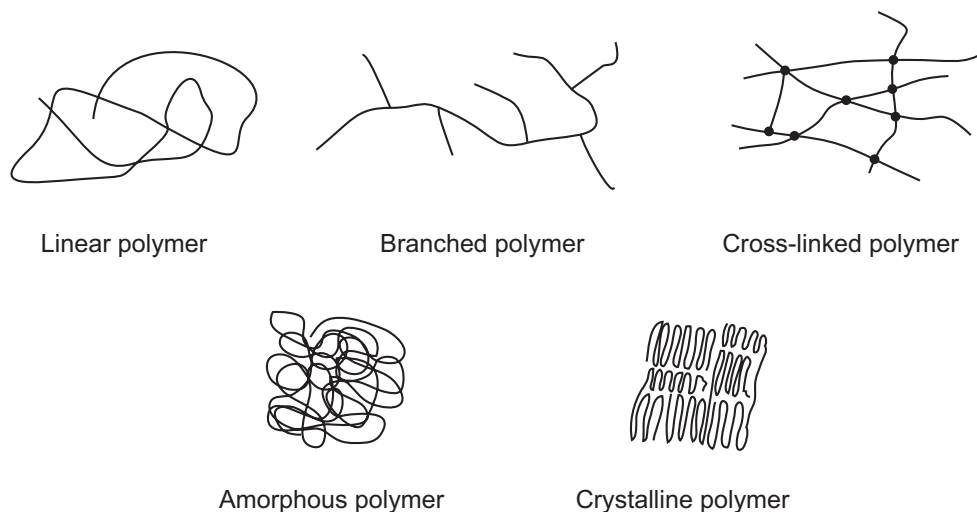


Figure 3.1. *Polymer chains and arrangements of molecules in polymers.*

Another significant aspect for the mechanical behavior is whether the polymer chains are arranged in a crystalline or amorphous structure (Fig. 3.1). Under specific conditions thermoplastic polymers contain regions of crystalline structures where the polymer chains arrange themselves in a crystalline order. These semicrystalline polymers consist of a mixture of crystalline and glassy arrangements. The appearance of semicrystalline state strongly depends on the structure of the macromolecules [97].

If crystalline polymers are cooled down from liquid state, an abrupt volume decrease can be observed at the melting temperature, T_m . An amorphous polymer remains in viscous state until it reaches the glass transition temperature, T_g . At the time the relative movement of the molecules becomes restricted the free volume is frozen and the polymer forms a glassy state. The value of T_g depends on the chemical structure of the polymer. In general it reflects the ease with which the molecules can move in the liquid state and so is increased if the polymer has a rigid backbone and/or bulky sidegroups [98]. In addition T_g strongly depends on the cooling rate so that a rapid cooling goes hand in hand with an increase of T_g .

The discussed molecular structures of polymers are the reason for their viscoelastic behavior. The deformation of the entangled or cross-linked chains or changes in conformation caused by mechanical loading and the recovery of the molecules into their original structure after unloading is driven by thermal motion. The thermodynamic equilibrium is not achieved spontaneously but with a delay. Therefore, polymers show the typical viscoelastic processes of creep and relaxation. Details on the measurement of viscoelastic properties are given in Sect. 3.2.

The fracture process of polymer is primarily dominated by two types of bonds i.e. covalent bonds between atoms of the molecular chain and secondary van der Waals forces between molecule segments. Secondary bonding forces act between adjacent molecules or segments of the same (folded) molecule. For the formation of new surfaces during the fracture process the covalent bonds have to break. Nevertheless, the van der Waals forces play a significant role during the deformation process before the ultimate fracture. The factors that govern the toughness and ductility of polymers include strain rate, temperature, and molecular structure. At high loading rates or low temperatures (relative to T_g) polymers show a brittle behavior, because there is insufficient time for the material to respond to stress with large-scale viscoelastic deformation or yielding. Highly cross-linked polymers are also incapable of large scale viscoelastic deformation [82]. For cross-linked polymers van der Waals forces are not significantly involved in the fracture process. For these materials breakage of primary bonds is necessary to enable large scale deformations.

Especially for ductile polymers plastic deformation is dominated by the following mechanisms:

1. **Shear yielding:** This is a large scale deformation at constant volume leading to a permanent change in specimen shape. The formation of shear bands is possible at specific strain rates and temperatures. Shear yielding is activated by a translation of molecules past each other when a critical shear stress is reached. In semicrystalline polymers it takes place through slip, twinning and martensitic transformation. In glassy polymers highly localized shear bands or diffuse shear deformation zones are formed [98].
2. **Crazing:** Glassy polymers subjected to tensile loading often yield by crazing, which is a highly localized deformation that leads to cavitation (void formation) and strains on the order of 100 % [82]. In contrast to shear yielding crazing is accompanied by a change (increase) in specimen volume. Crazes are generally nucleated at imperfections in polymer specimens such as surface flaws or dust particles. Multiple crazing can lead to general yielding and act as a toughening mechanism in polymers. Polymers with a second phase are specially prepared to take the advantage of this toughening mechanism [98].

Crazing and shear yielding are competing mechanisms; the dominating behavior depends on molecular structure, stress state and temperature [82].

An increase of toughness of a material can be achieved by enlarging the deformation ability. This task is related to realization of higher strength and strain values.

Increase of material strength can be obtained by [99]:

- Decrease of regions of local stress concentration to minimize the tendency of micro-crack initiation. Therefore, highly homogeneous materials are necessary requiring cost-intensive production processes.

- Increase of local strength by orientation of macromolecules. This concept is realized in fibers, liquid-crystal polymers and fiber reinforced polymers. However, the drawback of such materials is the requirement of special production processes and the anisotropy of the material with poor strength values perpendicular to the orientation direction.
- Rapid fluctuation of local stress concentrations by relaxation in order to minimize the tendency for crack formation. This requires local areas of high molecular mobility in the immediate neighborhood of stress concentrations or microcracks to guaranty stress relaxation or crack arrest. The described concept requires the application of heterogeneous multiphase polymer systems.

Increase of strain can be realized by [99]:

- Decrease of yield stress by increasing molecular mobility. This concept is known as softening which goes hand in hand with a decrease in strength.
- Realization of numerous local (microscopic) yield regions achievable by an appropriate material heterogenization.

The last statement implies that processes of local energy absorption have to take place in such a large volume of polymer material that the required energy absorption can be realized. Possible energy absorbing processes are small scale yielding, plastic zone formation, crazing, shear yielding or molecule chain scission [99].

Nevertheless, it has to be noted that an increase of a specific mechanical property often has an influence on other properties. The price for an increase in fracture toughness often goes to a decrease in mechanical module.

3.1.2 Cyanate Ester Thermosets

In the past, the growing demand for high performance, high temperature resistant, and easy-to-process matrix resins in fibre-reinforced composites and electronic applications has encouraged research on several thermosetting polymeric materials. The most significant group is the epoxy resins which are broadly used among other fields of applications in structural parts of aerospace vehicles and for encapsulant material and IC-board matrix material of electronics industry. For higher service temperatures epoxies cannot be used and other candidates such as cyanate ester resins have to be investigated to fulfil this role [100].

A comparison of conventional high performance thermoset matrix resins with cyanate ester resins (CE) is given in Fig. 3.2.

Developments in molecular architecture have produced second generation cyanate ester resins with performance in the T_g range 190-290°C with inherently more toughness than either epoxies or bismaleimides (BMI), lower moisture absorption and lower dielectric-loss properties [100].

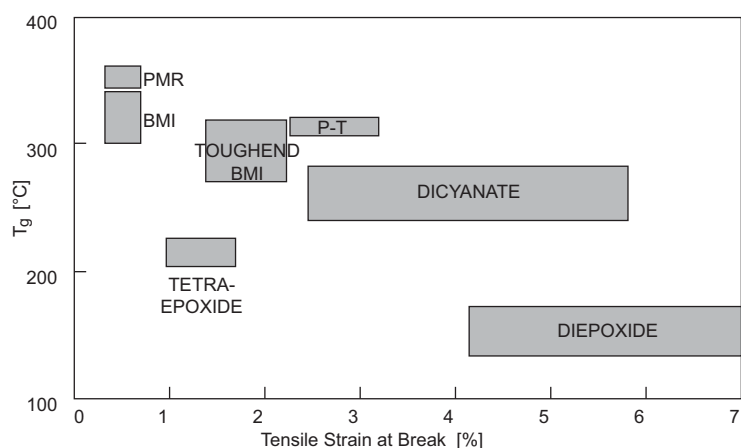


Figure 3.2. Relationship of T_g and tensile strain-at-break for several families of commercial thermoset resins [101].

The chemical composition of a cyanate ester monomer is given in Fig. 3.3 containing the reactive ring-forming cyanate ($-\text{O}-\text{C}\equiv\text{N}$) functional groups. Chemically this family of thermosetting monomers and their prepolymers are esters of bisphenols and cyanic acid. The R in the structural model of Fig. 3.3 may be a range of functional groups, e.g. hydrogen atoms, methyl or allyl groups, and the bridging group may be simply an isopropylidene moiety or an extended aromatic or cycloaliphatic backbone etc. [100].

Cyanate ester monomers polymerize by a cyclotrimerization reaction to a cyanurate linked network polymer. A description of this step-growth reaction would go beyond the scope of this work. Details can be found in various publications [3, 102].

Cyanate esters comprise the properties of high thermal stability, low outgassing, and radiation resistance [103], low dielectric constant (2.5 – 3.1), dimensional stability at soldering temperatures (T_g : 250-290°C) and low moisture absorption 0.6 – 2.5% with the processability of epoxy resins. These properties make cyanate ester resins a material of choice for high speed printed circuit boards. An encapsulant material for bare mounted chips was formulated by blending of AroCy L-10 with RTX-366 (both of them are CEs) [101]. A snap cure application for electronic packaging on the basis of a combination of CE and encapsulated hardener particles was reported by Bauer [104]. The single largest use for

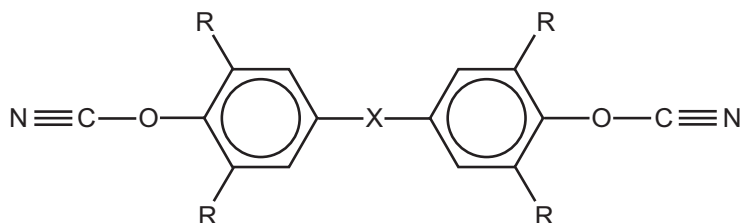


Figure 3.3. General structure of commercial cyanate ester monomers.

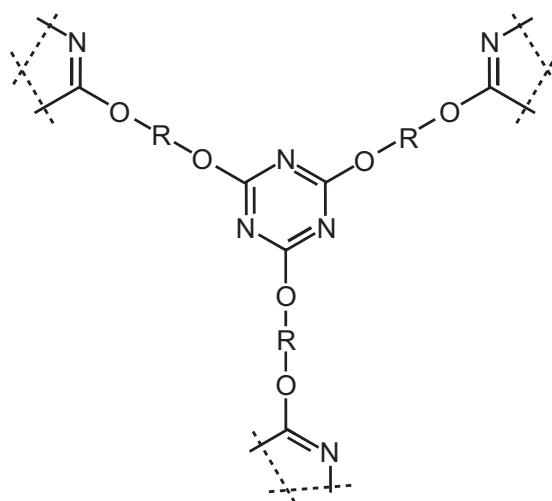


Figure 3.4. *Structure after cyclotrimerization.*

CEs is the lamination of substrates for printed circuits and their assembly via prepreg adhesives into high density, high speed multi-layer boards [105]. High frequency circuits for wireless communication and tracking systems with frequencies up to 12 GHz are the fastest growing use [101]. Fast growing application of CEs are dispatcher radios, pagers, cellular phones, global positioning, satellite broadcast, and radar tracking systems. Cyanate esters are likely to find applications in photonics, as optical wave guides, and in nonlinear optics [106,107].

Besides, electronics CEs are also applied in aerospace applications where their advantages in comparison to other resins are predominating factors and cost is only of secondary concern. Primary and secondary structures in military aircraft, radome and satellite applications are important fields of application. Low out-gassing, minimal dimensional changes during thermal cycling, good long term stability, self adherent properties to honeycomb and foam cores, good electrical properties and high service temperatures are the key advantages for their applications in aerospace [101].

A drawback of highly cross-linked thermosets, such as cyanate esters, is their brittleness and low impact resistance. Although a cured cyanate resin has a relatively high toughness compared to a cured BMI or a crosslinked epoxy resin, it still requires suitable modification to improve toughness without reducing the intrinsic physical strength for structural applications. The uncured cyanate resins are compatible with a number of amorphous thermoplastic polymers, including copolyester, polysulfones, polyether sulfones, polyacrylates and polyether imides [16]. In the course of curing, most of the mentioned polymers phase-separate into micron or sub-micron sized domains exhibiting a co-continuous or phase-inverted morphology at concentrations $> 15\text{wt}\%$ because of the high molecular weight of the thermoplastic [106].

Kinloch and Taylor [108] report on toughening of CEs with polyether sulfone (PES) which can increase the fracture energy of up to 800 %. In current research the application of nanofillers is becoming a promising approach. Ganguli et al. [109] developed nanocompos-

ites by dispersing organically modified layered silicates (OLS) into a cyanate ester resin. With an inclusion of 5% by weight the modulus and the toughness was increased by 30 %.

3.1.3 Tested Material Systems

A commercially available cyanate ester monomer AroCy B-10 (Ciba Geigy) was used for the production of test panels. The chemical structure of the monomer is equivalent to Fig. 3.3 where R are hydrogen atoms and the bridging group X is a isopropylidene moiety.

The elastomer used for modifying of the neat resin was the polycaprolactone-siloxane copolymer Tegomer H-Si6440 (Goldschmidt). In the mixture of 10wt% Tegomer and 90wt% B-10 a two-phase morphology with a structure in nanometer range can be expected.

The curing cycle was identical for the neat and rubber modified resin and was carried out at several isothermal temperature steps to achieve a void free material. The maximum curing temperature was 250°C which was applied for 1h. The typical conversion of the functional groups for such a curing cycle is in the range of 95%.

Table 3.1 summarizes the used polymer systems of this work and defines a nomenclature which is referred to throughout this thesis.

Table 3.1. *Materials*

Resin	wt%	Modifier	wt%	Code
AroCy B-10	100			CE-B10
AroCy B-10	90	Tegomer H-Si6440	10	CE-B10-M

3.2 Viscoelastic Material Characterization

3.2.1 Viscoelasticity

Polymer materials show loading rate dependent viscoelastic deformation. The viscous behavior is caused by the ability of the molecules to move relative to each other. For this process the molecules need sufficient time. At faster strain rates, however, the forced molecular motion produces friction and higher stresses are necessary to deform the material, [110].

Under constant stress, the creep strain in a viscoelastic material may be divided into three components (Fig. 3.5 (left)) [110]:

1. *Instantaneous elastic strain* $\varepsilon_e(0^+)$. In a polymeric material, this part of the strain is caused by bond stretching and bending including the deformation of van der Waals bonds between molecular chains. This strain is reversible and disappears on removal of the stress.

2. *Delayed elastic strain* $\varepsilon_d(t)$. The rate of increase of this part of strain decreases steadily with time. It is also elastic, but, after removal of the load, it requires time for complete recovery. In a polymeric material, the delayed elastic strain is caused, for instance, by chain uncoiling.
3. *Viscous flow* $\varepsilon_v(t)$. It is an irreversible component of strain which may or may not increase linearly with time of stress application. In a polymeric material it is caused by interchain slipping.

Phenomenologically, two aspects of viscoelastic behavior can be observed i.e. creep response under a constant stress and stress-relaxation response under constant strain.

A linear viscoelastic material have to meet two conditions: proportional stress/strain behavior and superposition of subsequent loading regimes is possible. Figure 3.5 (right) illustrates the principle of superposition.

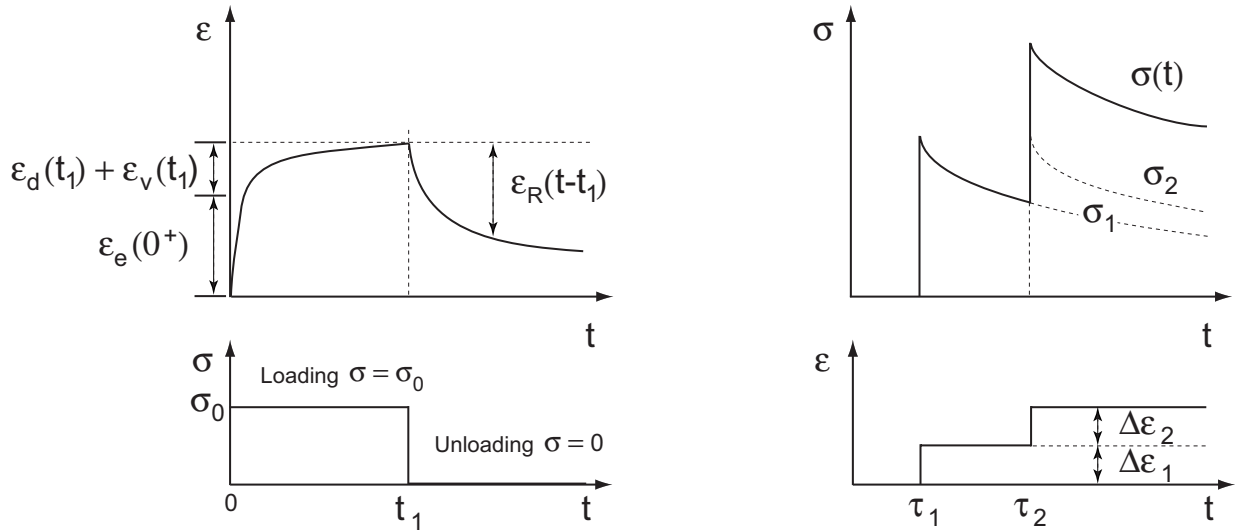


Figure 3.5. Viscoelasticity; **(left)** Creep and recovery of a viscoelastic specimen subjected to a constant stress until time t_1 ; **(right)** Superposition of stresses, σ , caused by two Heaviside step functions in strain ε_1 and ε_2 .

The response to single straining steps can be superposed to form the solution $\sigma(t)$. For a continuous description the constitutive equation is given by:

$$\sigma(t) = \int_{-\infty}^t E(t-t')\dot{\varepsilon}(t')dt' \quad (3.1)$$

The creep and relaxation function are related via the integral:

$$\int_{-\infty}^t E(t-t')D(t')dt' = t \quad (3.2)$$

The relaxation modulus, $E(t)$ and the creep compliance, $D(t)$ fully describe the time-dependent response of viscoelastic materials. For the measurement of viscoelastic behavior either the relaxation modulus or the creep compliance can be derived from tensile tests with fixed strain or stress, respectively:

$$E(t) = \frac{\sigma(t)}{\varepsilon_0} \quad D(t) = \frac{\varepsilon(t)}{\sigma_0} \quad (3.3)$$

3.2.2 Modeling of Viscoelasticity

The physical representation of a viscoelastic material is commonly established by a combination of spring/dashpot models [110]. The basis are Maxwell elements with a spring and a Newtonian dashpot in series and Kelvin-Voigt elements with a parallel arrangement of spring and dashpot. A generalization of the material model can be defined by a combination of several Kelvin-Voigt and/or Maxwell elements. Due to the fact that the experimental derivation of the viscoelastic behavior was carried out by stress relaxation experiments, in the following the emphasis is laid on the description by Maxwell elements. This leads to a straightforward approach for the functional description of the relaxation function as illustrated in Fig. 3.6. Details on other modelling approaches can be found in various textbooks on polymer mechanics [97, 110, 111].

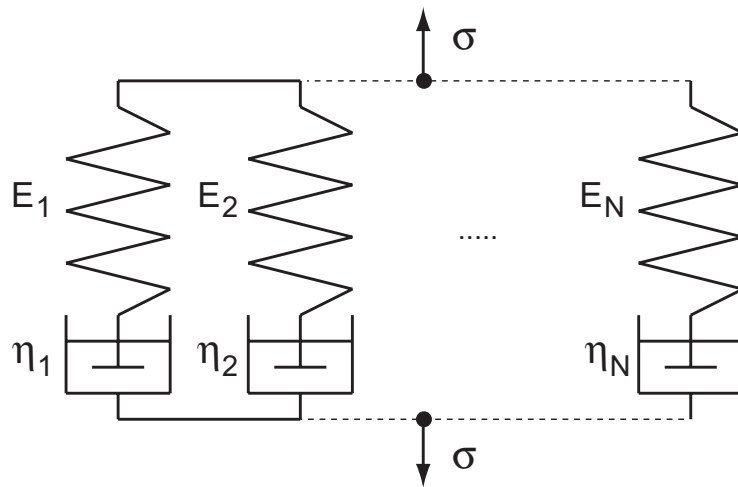


Figure 3.6. *Generalized Maxwell model for viscoelastic material.*

All of these N Maxwell elements are described by the differential equation:

$$\sigma + \tau \dot{\sigma} = \eta \dot{\varepsilon} \quad (3.4)$$

where η is the fluid viscosity in the dashpot element and $\tau = \eta/E$ is the relaxation time. The solution of this differential equation is the relaxation function:

$$E(t) = E \exp\left(-\frac{t}{\tau}\right) \quad (3.5)$$

The relaxation function of the generalized system of parallel Maxwell elements is given by the Prony series:

$$E(t) = \sum_{i=1}^N E_i(t) = \sum_{i=1}^N E_i \exp\left(-\frac{t}{\tau_i}\right) \quad (3.6)$$

For the numerical implementation of viscoelastic material properties usually Prony series as given by Eqn. 3.6 are implemented in available FE codes, so that the stress-relaxation is described by a series of exponential functions with experimentally fitted parameters.

3.2.3 Time-Temperature-Superposition

In the mechanical behavior of polymer materials an equivalence in the material reaction to loading at high temperatures and after long time intervals was found. This was the basis for Williams, Landel and Ferry [112] developing a semi-empirical equation which allows the shifting of relaxation curves measured at different temperatures to a single modulus-time master curve. They defined the shift factor, a_T as:

$$\log a_T = \log \frac{t_T}{t_{T_0}} = \frac{C_1(T - T_0)}{C_2 + T - T_0} \quad (3.7)$$

where t_T and t_{T_0} are times to reach a specific modulus at temperatures T and T_0 , where T_0 is a reference temperature (usually defined at the glass transition temperature, T_g), and C_1 and C_2 are material fitting parameters. Time-temperature-superposition is the basis for straightforward material characterization by simple stress relaxation test at various (sufficient) temperatures.

3.2.4 Experimental Setup and Data Acquisition

The measurement of the viscoelastic material properties was carried out through stress relaxation tests at specified temperatures. A standard testing machine (Zwick Z 1446) equipped with a temperature chamber was used for the measurements. The chosen specimens were "dogbone" shape specimens according to DIN 53504 [113]. The specimens were machined as defined by the geometry *S3A* (overall length of the specimen: 50 mm, parallel length: 16 mm, thickness: 2 mm). During loading the strain was measured direct at the specimen surface using Zwick's universal extensometer "Multisens". The load was applied with a velocity of 5 mm/min until a strain value of 0.2 % was reached. Then, the crosshead of the machine was stopped and a stress relaxation test i.e. force measurement was carried out for one hour. The relaxation tests were only carried out at the temperatures of 25 and 150°C . Due to the fact that the loading experiments of Sect. 3.4.4 are carried out in approximately one hour these two temperatures are sufficient for the viscoelastic description of the polymer material.

3.2.5 Results of Viscoelastic Material Characterization

Figure 3.7 shows the results of the neat CE in a logarithmic plot, including the fitted master curve. The master curve has to be understood as fitting function of the relaxation curve. A complete material characterization ranging over large time/temperature regime was not necessary in this work.

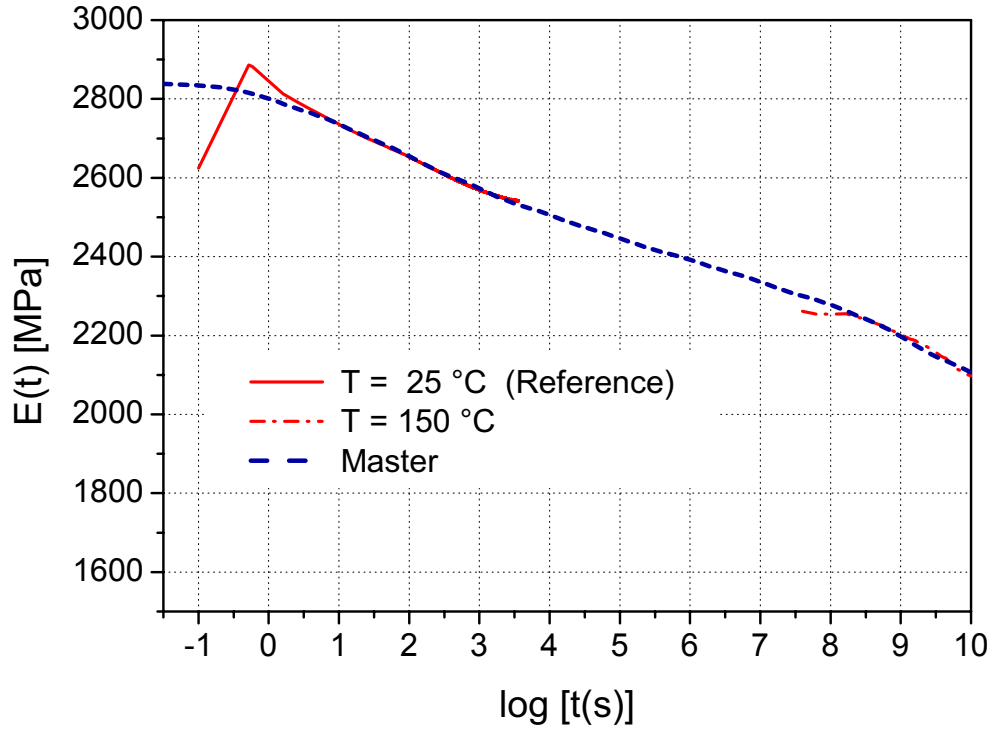


Figure 3.7. Master stress-relaxation curve of cyanate ester resin.

The fitted Prony series of the cyanate ester resin is given by:

$$\begin{aligned}
 E = & 2070 + 100 e^{\frac{t}{10^{10}}} + 100 e^{\frac{t}{10^9}} + 50 e^{\frac{t}{10^8}} + 60 e^{\frac{t}{10^7}} + 50 e^{\frac{t}{10^6}} \\
 & + 60 e^{\frac{t}{10^5}} + 60 e^{\frac{t}{10^4}} + 80 e^{\frac{t}{10^3}} + 90 e^{\frac{t}{10^2}} + 70 e^{\frac{t}{10}} + 50 e^t \text{ [MPa]}
 \end{aligned} \tag{3.8}$$

The Prony-type description of viscoelastic material is suited for the application in finite element software. FE calculations of Sect. 4.4 refer to the material model given by Eqn. 3.8.

3.3 Advanced Fracture Analysis for Polymers

The group of Bauer developed the Optical Crack Tracing (OCT) system which is a technique of automatic determination of fracture toughness, K_{Ic} , by means of optical crack tip

localization [114,115]. The system allows the measurement of the R -curve, i.e. the fracture toughness for crack initiation and propagation. With the measurement of the R -curve instead of the fracture toughness according to the standard ASTM D5045 [84] a better understanding of the fracture behavior is achieved. The benefits of the OCT method can be summarized as follows:

- Information on the type of crack propagation such as steady state, stick-slip and intermediate between steady state and stick-slip can be extracted.
- The influence of time dependent phenomena on the fracture behavior of polymers can be analyzed.
- Prevention of overestimation of fracture toughness induced by non-ideal pre-cracks is established.

In the following, a short description of the system the measurement principle and the extracted results are given. A detailed discussion of the technique can be found in the papers of Uhlig, Kahle, Keller and Bauer et al. [114–116].

3.3.1 Optical Crack Tracing (OCT) Technique

The Optical Crack Tracing system (LaVision OCT) includes hardware and software components to record crack length at the beginning and during crack propagation by video recording and subsequent digital image analysis. The set-up of the system is shown schematically in Fig. 3.8.

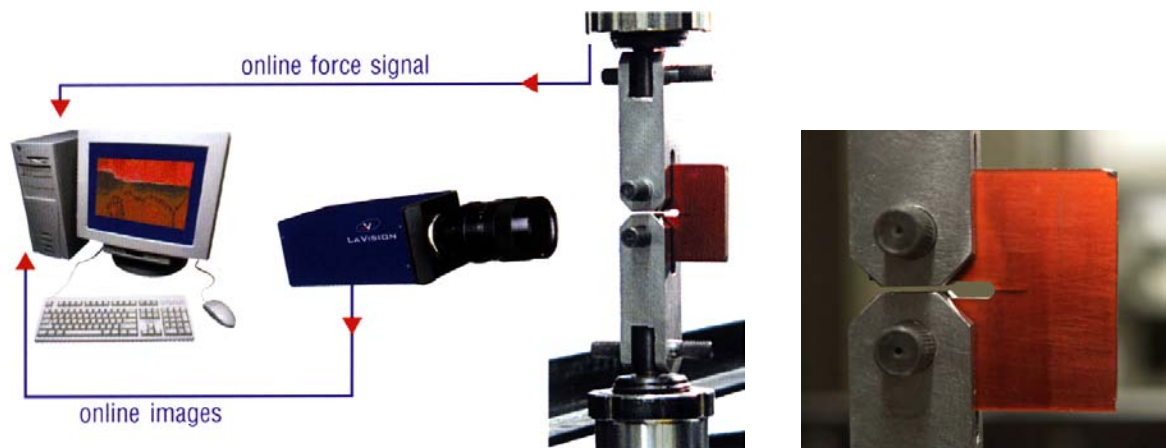


Figure 3.8. Scheme illustrating the experimental set-up of OCT.

During the fracture test the video images and the force signal from the testing machine are stored in the RAM of a personal computer. After the test the series of images is analyzed by image analysis software. Digital filter algorithms filter the maximum gradient in brightness and by subsequent setting of brightness threshold other structures in the image are removed

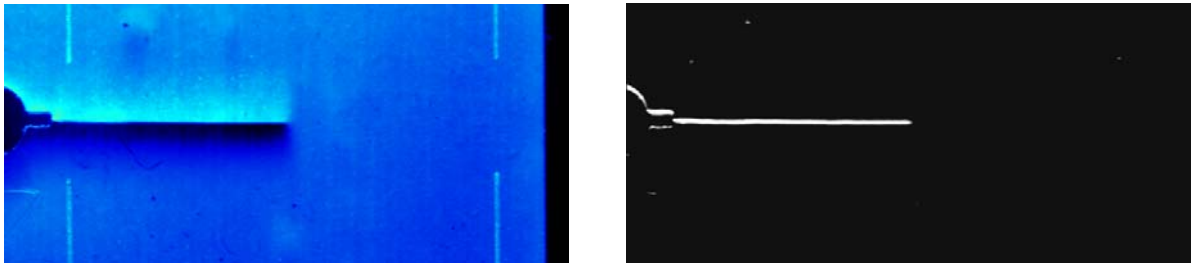


Figure 3.9. Image before and after image analysis used for crack length determination; *(left)* original image showing a brightness gradient at the crack face; *(right)* filtered image showing the structures with maximum brightness gradient values.

so that only the crack is retained. An example of such an image analysis is shown in Fig. 3.9.

A step gradient in brightness of the crack is achieved by lightening the specimen at an inclined angle. This technique can be applied to transparent and non-transparent materials. In the case of a non-transparent material a 10-bit CCD camera with a resolution of 1024×768 pixel should be used to achieve optimized brightness gradients at the crack face. The analysis software identifies the crack by segment routines (the longest segment found is identified as the crack) and the crack tip location is determined in pixel coordinates. A scaling procedure which utilizes markings (compare to Fig. 3.9 (left)) on the specimen transforms the pixel coordinates directly into crack length data. By simultaneously measuring the load/displacement curve and crack-length/displacement curve the OCT software calculates the stress intensity factor K_I from relationships known for standard geometries of crack test specimen (Eqns. 2.9, 2.10). A typical set of measured data and results is shown in Figs. 3.10 and 3.11.

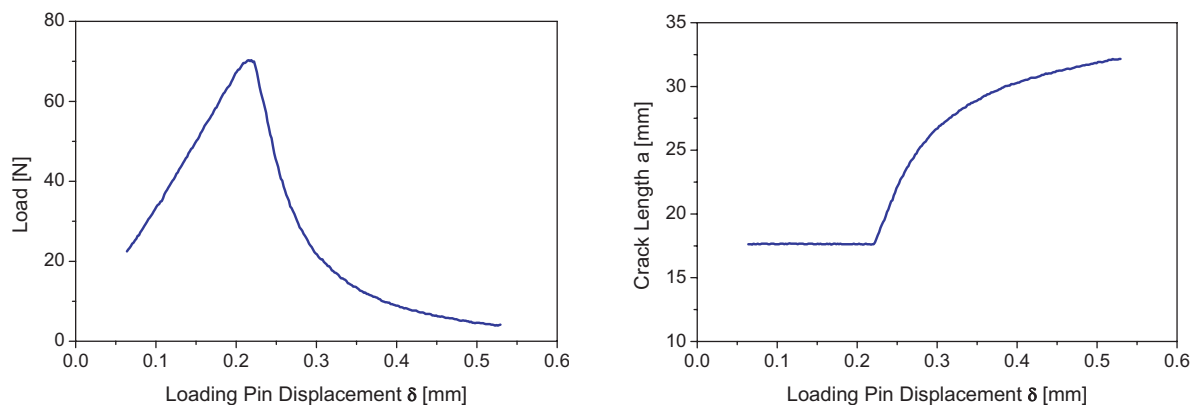


Figure 3.10. Example for a typical set of load vs. displacement and crack length vs. displacement diagrams measured by Optical Crack Tracing.

In the following, the merits of measuring the R -curve rather than calculating only the initiation fracture toughness from the load at fracture and the initial crack length (measured

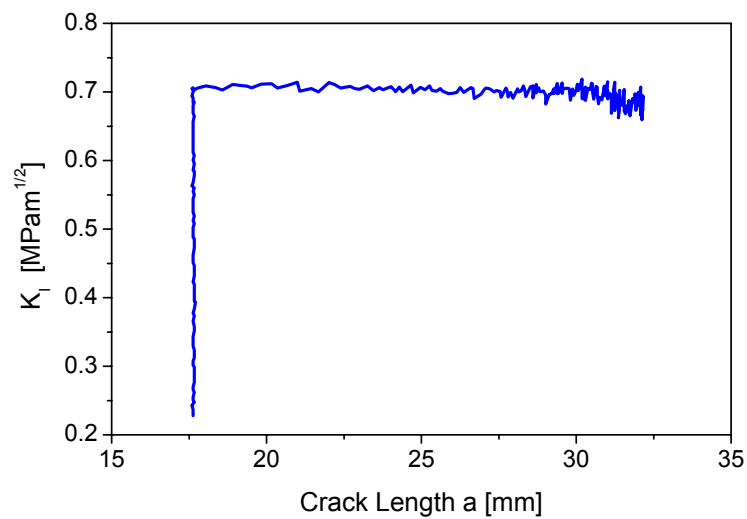


Figure 3.11. Results of the fracture mechanical analysis: R -curve (K_I , at crack initiation and propagation).

by analyzing the crack front as is described in the standards) shall be discussed.

3.3.2 Measurement of the R -curve in Comparison to Standard ASTM D5045

The typical case of an R -curve for stable fracture which can be described by linear elastic fracture mechanics is shown Fig. 3.11. In this example, the fracture toughness is the same for crack initiation and propagation, which can be expected for the case of linear elastic fracture mechanics. The procedure described in the A.S.T.M standard [84], which calculates only a single value for crack initiation and the measurement of the R -curve would lead to identical values.

However, the standard for the determination of crack initiation fracture toughness requires an ideal pre-crack, i.e. an initial crack that is ideally sharp and lies in the plane of symmetry of the specimen. This so-called *self-similar* crack cannot be guaranteed by the usual method of tapping in a sharp razor blade to generate a pre-crack.

Non-ideal pre-cracks are cracks which lead to an increase of crack initiation stress intensity factor i.e. the fracture toughness. In the cases where the crack front is not parallel to the plane of symmetry because it is twisted or there are steps in the pre-crack front a significant increase of the crack initiation stress intensity factor is found. Under this conditions the crack opening mode I is superposed by mode II behavior (compare to Sect. 2.3) inducing a higher resistance to fracture than a pure mode I crack opening.

Accurate quantitative analysis by mapping the fracture surfaces of a large number of specimens confirmed the visual observation. As an example, the analysis of the crack surface of a specimen with a step-like initial crack front is shown in Fig. 3.12. To analyze

the influence of the step height Δy is introduced as illustrated in Fig. 3.12. The value of step height Δy is decreasing during crack propagation until a plane crack front is formed.

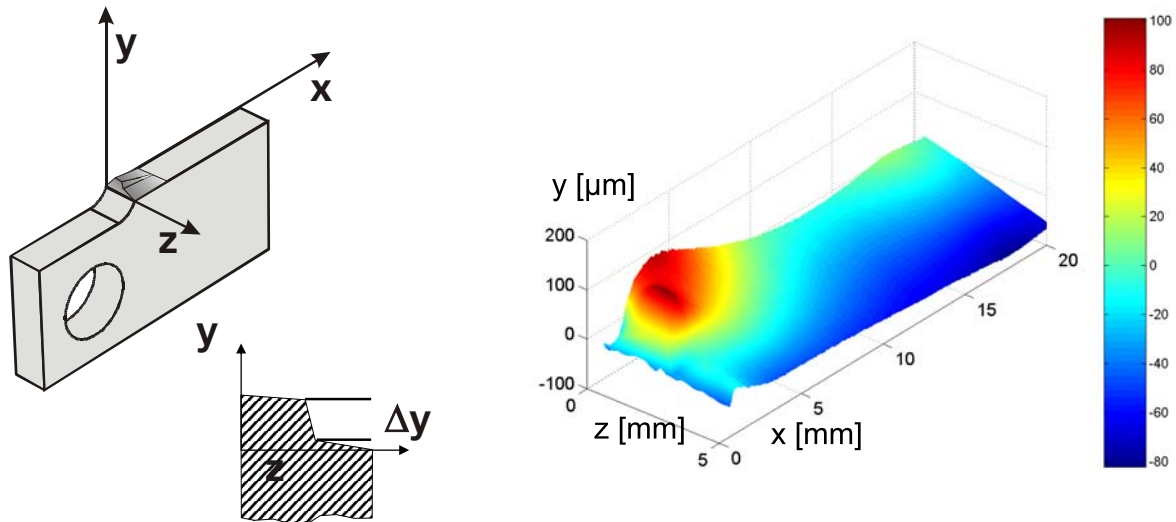


Figure 3.12. (left) CT-specimen with non-ideal pre-crack; (right) topographical (y)-map of crack surface; note: the x -coordinate at the axis is not identical to the crack length a of the CT-specimen.

In Fig. 3.13 the effect of a non-ideal pre-crack on the R -curve is illustrated. The critical stress intensity factor and the step height Δy as defined in Fig. 3.12 are plotted vs. the crack length.

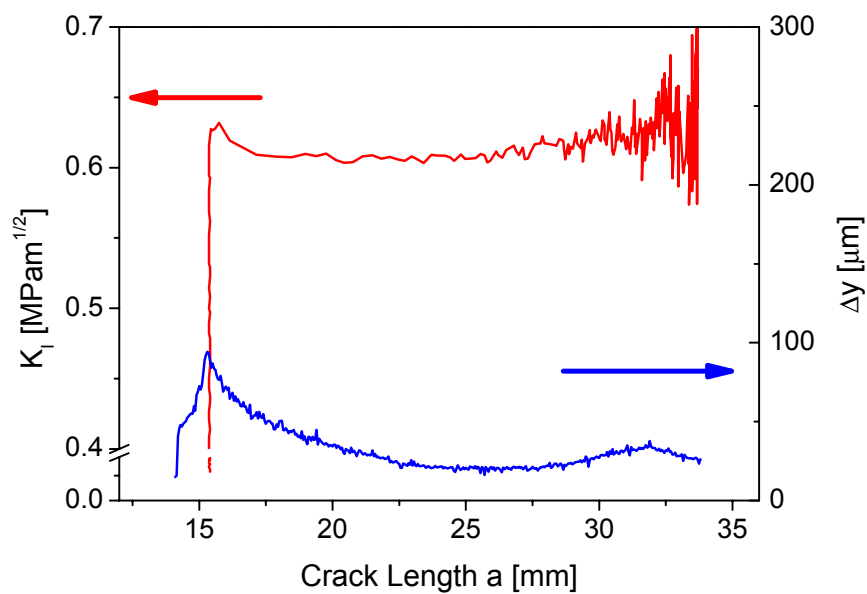


Figure 3.13. R -curve and step height Δy vs. crack length.

The shape of the R -curve at the beginning of the crack propagation can be easily understood because in the case of a step-like crack front there is also a mode II component included and the fracture toughness in mode II is significantly higher than that in mode I. By the same argument it can be understood that the crack approaches the plane of symmetry during crack propagation and consequently fracture toughness approaches the true mode I value for the material as can be seen in Fig. 3.13. Thus in cases of non-ideal pre-cracks still the true mode I fracture toughness can be obtained if the R -curve is measured [117].

3.3.3 Results of OCT

The measured R -curve of the neat cyanate ester resin and the rubber modified resin system is shown in Fig. 3.14. The results clearly show the effect of the rubber modification on the fracture behavior. On the one hand the fracture toughness is increased from 0.5 to a value of $0.9 \text{ MPam}^{1/2}$, on the other hand the fracture occurs in a stick-slip type.

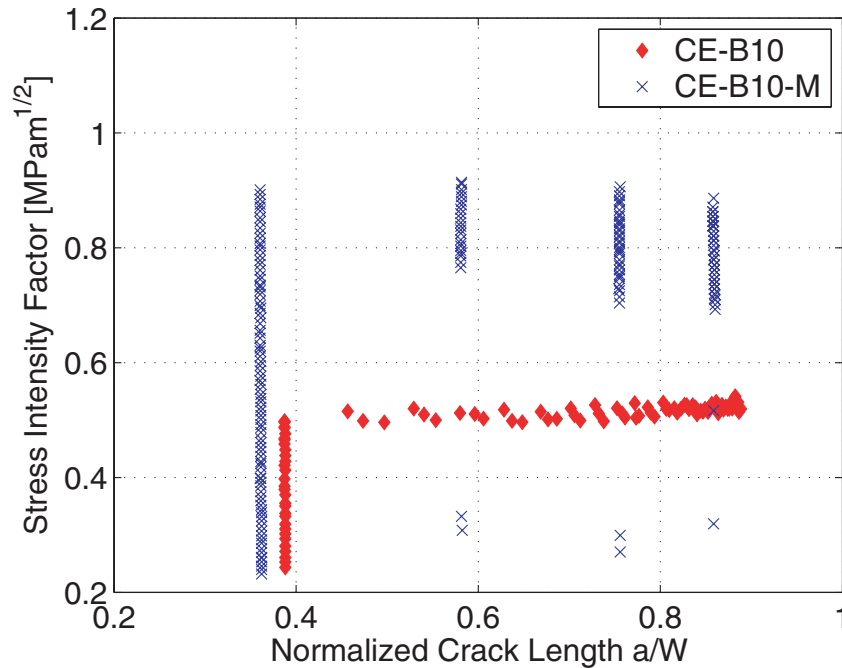


Figure 3.14. R -curve of unmodified and rubber modified cyanate ester resin.

Table 3.2. *Fracture toughness and Young's modulus*

Material	E [MPa]	K_{Ic} [MPam ^{1/2}]
CE-B10	2800	0.5
CE-B10-M	2700	0.9

From the obtained results from OCT based fracture toughness testing the following questions arise:

- Does the stick-slip behavior correlate with micro- or nanoscopic morphology of the neat and rubber modified polymers (process zone)?
- Does crack tip blunting prevail in the process zone of the rubber modified system?

In Sect. 4.3 Fig. 4.4 an example of stick-slip behavior is illustrated by fractographical microscopy image.

3.4 Crack Field Analysis by In-Situ AFM Measurements - nanoDAC

The measurement and evaluation of deformation processes on the micro- and nanoscopic range by the combination of SPM equipment and the technique of digital image correlation is a task requiring special prerequisites on the technical equipment. Three main issues have to be discussed if digital image correlation is supposed to be applied on SPM data:

- suitable specimen loading devices must be designed or adapted to the SPM equipment,
- high level scanning stability and reproducibility have to be provided,
- concepts for correction of scanner drifts have to be developed.

Following these objectives the utilized apparatus and arisen stability problems and their solution have to be discussed.

3.4.1 General Aspects of Scanning Probe Microscopy

With the development of the scanning tunneling microscope (STM) [118] and the atomic force microscope (AFM) [119] the foundation was laid for fundamental and technology orientated research on the nanoscale. Nowadays, the development of new scanning probe microscopy (SPM) techniques is a vital task for the nanotechnology driven product development. SPMs have been developed for various applications. These include – STM,

AFM, friction (or lateral) force microscopy (FFM or LFM), scanning electrostatic force microscopy (SEFM), scanning force acoustic microscopy (SFAM) (or atomic force acoustic microscopy (AFAM)), scanning magnetic microscopy (SMM) (or magnetic force microscopy (MFM)), scanning near field optical microscopy (SNOM), scanning thermal microscopy (SThM), scanning electrochemical microscopy (SEcM), scanning Kelvin Probe microscopy (SKPM), scanning chemical potential microscopy (SCPM), scanning ion conductance microscopy (SICM), and scanning capacitance microscopy (SCM). A good starting point for further reading and related papers on this SPM techniques is the "Handbook of Nanotechnology", [120].

A complete description of the various techniques would be beyond the scope of this thesis. Therefore, only the significant details of the applied SPM instruments and the utilized imaging techniques are discussed in the following.

The AFM used in this work (ThermoMicroscopes (VEECO), Autoprobe M5) is designed as illustrated in Fig. 3.15.

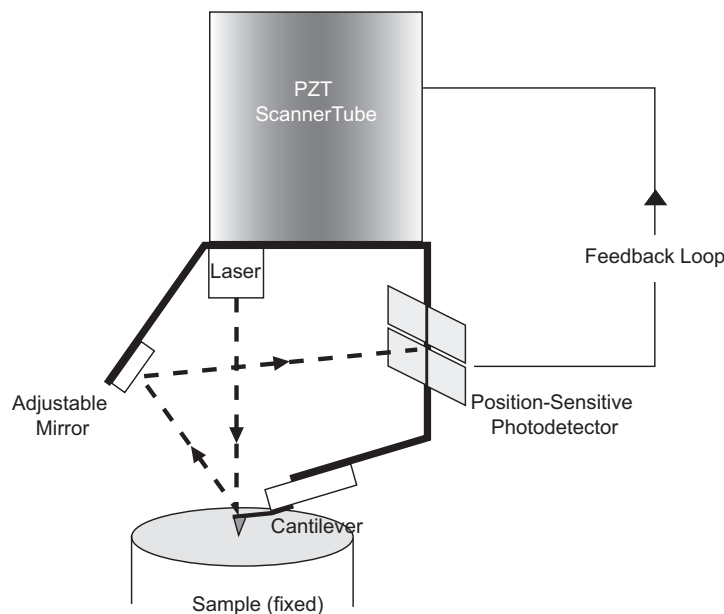


Figure 3.15. *Principle of AFM.*

The drive of the cantilever in the scanning- (x, y) and height- (z) direction is achieved by a piezoceramic tube scanner ($100 \times 100 \mu\text{m}$ large area scanning unit). The height information of the scanned surface is picked up by a so-called beam bounce detection system [121]. A laser beam is reflected from the back of the cantilever onto a position-sensitive photodetector (PSPD) via an adjustable mirror. As the cantilever bends the position of the laser spot on the PSPD changes resulting in a voltage shift which is a measure for the cantilever deflection. With the feedback-loop the scanning tube is adjusted to the actual height of the surface, so that a constant deflection of the cantilever is guaranteed during scanning. For atomic flat surfaces the system can also be driven in constant height mode where the cantilever is held at a constant height and the variation of the cantilever

deflection is recorded. The signal for the drive of the scanner tube in z -direction is called error-signal. It is derived from the difference of the last to the actual value of the PSPD.

The usage of piezoceramics as scanning units for the x - and y -directions have the disadvantage of high nonlinearities in the behavior of the applied voltage to the resulting strain of the PZT material. Therefore, the so-called scan master which can be understood as a linearization matrix enables correct positioning of the cantilever [121]. Due to the fact that piezoceramics also show time dependent material properties calibration routines in x , y and z -direction have to be carried out from time to time.

The AFM can be used either in a static or dynamic mode. In the static mode, also known as repulsive mode or contact mode the cantilever tip is brought in contact with a sample surface. During contact, the cantilever experiences a very weak (repulsive) force caused by the electronic orbital overlap of the atoms at the end of the tip with the atoms in the sample surface. The force acting on the tip causes a cantilever deflection which is measured by the PSPD. In the dynamic mode of operation for the AFM, also referred to as attractive force imaging or noncontact imaging mode, the tip is brought in close proximity (within a few nm) to the sample so that very weak van der Waals attractive forces are present at the tip-sample interface. The cantilever is vibrated either in amplitude modulation [122] mode or frequency modulation [123] mode. In contact mode, the interaction force between tip and sample is measured by measuring the cantilever deflection. In noncontact mode, the force gradient is obtained by vibrating the cantilever and measuring the shift of resonant frequency or the change of vibration amplitude.

To obtain topographic information of the scanned surface, the interaction force is either recorded direct, or used as a control parameter for a feedback loop that maintains the force or force derivative at a constant value [120]. To overcome the limitations of contact mode (influence of friction on topographic image) and to analyze the surfaces of soft materials the AFM can also be operated in the so-called tapping mode [124]. In this cantilever vibrates close to its resonance frequency and the tip lightly taps the surface rather than getting into contact with fully repulsive interaction. In addition to topographic imaging the tapping mode can also be used for the analysis of surface mechanical properties. Generally, the tip-sample interaction causes a change in the amplitude, the phase and the resonance frequency of the vibrating cantilever. The spatial variation of these changes can be presented in interaction (amplitude, phase or frequency shift) images [125].

3.4.2 Instrumentation of AFM measurements

The installation of thermal and/or mechanical loading stages in the SPM is mainly a question of compact design of loading stages, free access for SPM cantilevers to the specimen and a probe actuation instead of a specimen actuation. The available SPM equipment (Autoprobe M5) and loading stages required the installation of additional spacers between the scanning head and the ground plate. The tension/compression loading device as illustrated in Fig. 3.16 is attached to x - y -stages with positioning accuracies of ± 10 nm in one direction and ± 1 nm in the other direction. In addition, fine adjustment in the nanometer range can also be performed by the piezo drive of the AFM. In order to minimize scanning instabilities and different thermomechanical drifts (compare to Sect. 3.4.3) common tools

of environmental isolation are installed. This comprises active vibration compensation of equipment tables and acoustic enclosures against ambient sound.

The employed tension/compression testing module is designed for in-situ SEM and SPM measurements (Fig. 3.16). For the case of the crack tip deformation field measurements at CT-specimens the module is equipped with a pin holder. For tension/compression tests on standard tension specimens micro-vices are available in various configurations. In addition standard tension/compression specimens can be thermally loaded with a contact heating system which is placed under the specimen. Figure 3.16 shows the module with an inserted CT-specimen, where Fig. 3.17 shows the set-up of the loading device with the CT-specimen under the SPM scanning head as it is installed during SPM measurements.



Figure 3.16. *Tensile module with CT-specimen.*

3.4.3 Stability Aspects of SPM Measurements

In comparison to DIC-based measurements treating optical or SEM images, some more essential difficulties have to be overcome for SPM-based imaging. They relate to the extreme magnification of SPM techniques. Since SPM image scans are taken over a time interval from one to several minutes, even minor system drifts can cause significant artificial object deformations. Classifying different drift sources it can be distinguished between:

- SPM scanner drifts, which are related to time dependent behavior of the piezo tube,
- relative movements between the scanning head and the sample fixture, mainly caused by temperature changes,
- drift of sample loading parameters (temperature, forces, load paths, etc.) within testing stages installed at the microscope, and

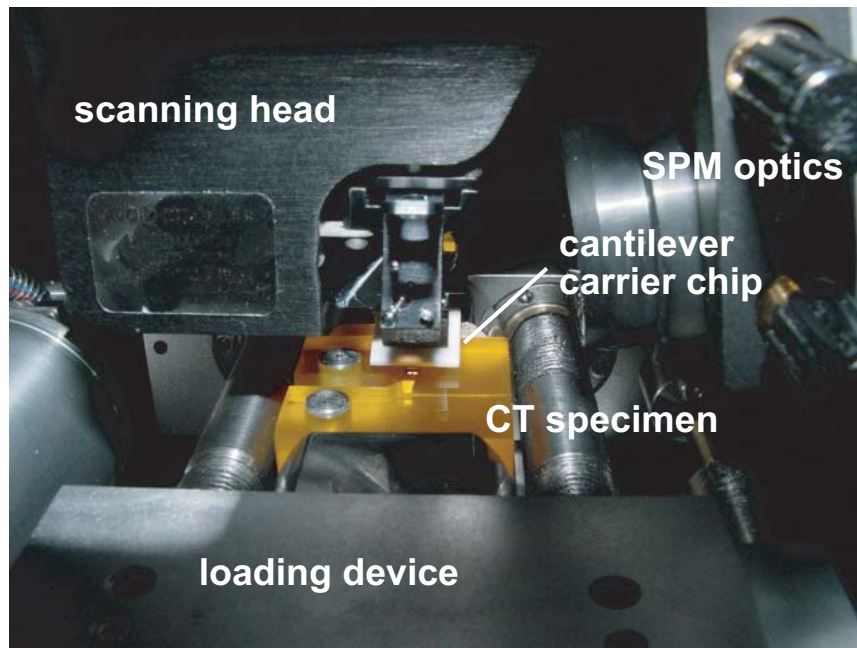


Figure 3.17. *In-situ loading of CT-specimen under SPM.*

- incremental object deformations originating from viscoelastic material behavior of test specimens, i.e. time dependent object deformations which take place even under constant loading parameters.

Substantial concerns regarding stability and reproducibility originate from drifts of the SPM scanner piezo and the variation of thermomechanical loading parameters over time. As a consequence, the accurate selection of SPM equipment and loading stages is a crucial issue. Moreover, the development and implementation of methods of drift control and compensation may be essential for particular applications.

In practical operation serious problems arise from the fact that the drift effects described above are not evident from a single image achieved at a specific load state of the specimen. In some cases severe drift effects come to light by digital image correlation of several images acquired at the same load state. For example, significant pseudo displacements occur when the scanner is adjusted to a new position of its scanning range either by the zooming-in capability of the SPM control software or user based definition of the new scanning range or scanning position. The application of DIC to images taken just after such positioning processes show large pseudo displacements caused by scanner creep. In some cases, this artifact is visible at a single image without the aid of a DIC analysis. The initial part of the scan range of a test pattern would appear distorted as illustrated in Fig. 3.18.

An example of the creep effect, with a pseudo strain in the vertical y -direction being clearly visible without the application of the DIC method is given in Fig. 3.19.

The images show a region of $15 \times 15 \mu\text{m}$ of an unloaded and stable mounted object with a metallic surface where the fast scanning is in the horizontal direction and the y -direction

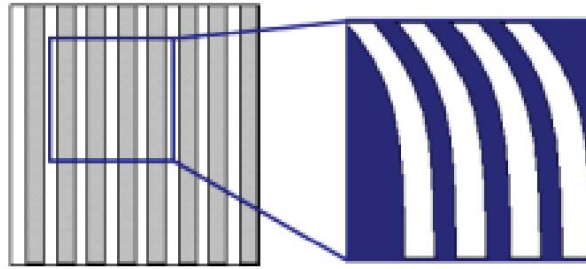


Figure 3.18. After a region of a sample is scanned with the AFM it is common to zoom into a small section of the image to get a higher magnification of an image. Scanner drift will cause the image to appear distorted at the beginning of the scan [126].

is scanned from top to bottom. The images are taken in noncontact mode and the data is extracted from one scan direction only to suppress artifacts caused by scanner hysteresis. The images are acquired directly after each other using the repeat function of the SPM software. The black polyline added to the topography images has the same size and position in both images but the particle marked with an arrow is not in the same position relative to the polyline. This implies a straining of the second (right) image relative to the first (left) image which should result in a large pseudo-strain if DIC method is applied to these images.

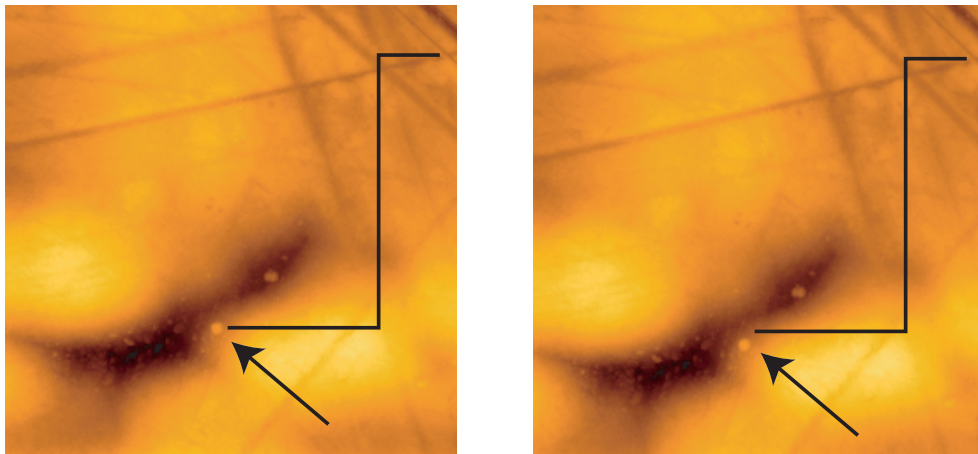


Figure 3.19. Two scans of a steel surface directly after repositioning of scanning range; the pseudo strain of the image at the right hand side compared the other image is visible by the different location of the particle marked with an arrow; image properties: $15 \times 15 \mu\text{m}$, 256×256 pixel, z-range: 213 nm.

To underline the creep effect of the scanner, a DIC displacement analysis is performed on the images of Fig. 3.19. In this case, only the y -direction of the displacement vector is of interest and the determined results are shown together with the image source in Fig. 3.20. The displacement results are given in pixel coordinates (1 pixel ≈ 59 nm). The first

conclusion is that there is a general drift of several pixels across the vertical dimension of the image. Secondly the displacement results clearly imply that there are larger strain values in the upper half of the image than in the lower half. This pseudo-strain effect is caused by the creep behavior of the piezo scanner. After a running-in phase it will converge into steady state scanning behavior. As a result the pseudo-strain mainly occurs in the upper part of the image.

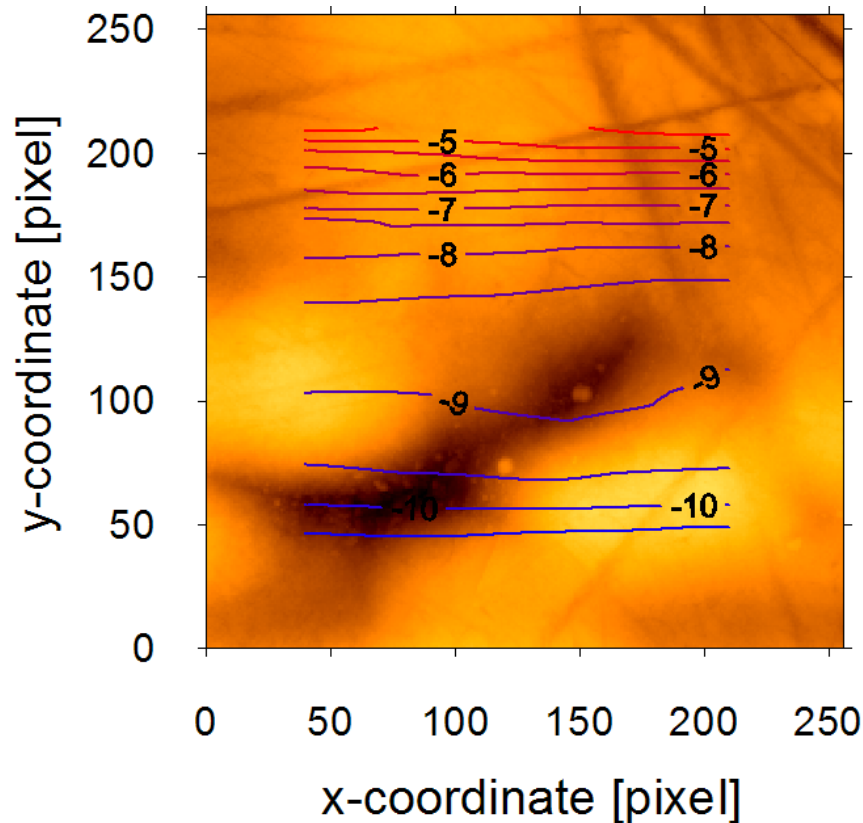


Figure 3.20. *Pseudo displacements in vertical direction u_y in [pixel], caused by scanner creep; contour lines of identical displacement are closer to each other indicating a larger strain level in the upper part of the image.*

The presented example emphasizes the requirements of stable scanning behavior to avoid artificial object deformation. As mentioned above, another important aspect is the thermal drifts of the apparatus including the AFM itself but also the specimen, loading device and its positioning system. Moreover, these different drift sources superpose so they cancel each other out or enlarge each other depending on the actual environmental and system immanent influences. Attempts about correcting the displacement by eliminating one specific stability source will always end up in the problem of the separation of the different sources.

Therefore, a feasible strategy would be the estimation of the actual drifts of the complete system in their summation rather than separating a single drift source. One possible way to follow this objective is the description of the drift by a functional and applying a

linearization to achieve an actual value for the system drift for a specific time period. A practicable way to determine the actual system drift would be to capture a series of 2-3 images at each of the load states to be compared. By a subsequent displacement analysis of each series utilizing the DIC code a mean drift value for each load state can be determined. If there is a difference between the mean drift at the specific load states, a correction has to be applied to the obtained DIC results between these load states. The described strategy can be tested by a series of scans on a fixed specimen. In the following, these test will be called "zero displacement test".

The displacements and their standard deviation determined from a zero displacement test are also a measure for the accuracy of the DIC concept on SPM images. According to [81] the applied DIC code has a pixel resolution of 0.1 for in-plane displacement components for CCD camera images. Assuming that the code performs similar on AFM topographs, a displacement resolution of 0.2 nm is to be expected for a $1 \times 1 \mu\text{m}$ scan and an image of 512×512 pixel (Eqn. 2.3). In practical operation, it is difficult to translate displace a macroscopic specimen with that accuracy. However, a zero displacement test and the resulting variation of the displacement is a measure for the precision of the measurements.

In the following section these zero displacement tests are discussed. Nevertheless, it has to be mentioned that new or somehow configured SPM and loading equipment should be tested for stability and accuracy. The presented results can only give a system description of the actual utilized equipment within this work. The trend of the SPM manufacturer to develop scanning equipment with increased line scan frequency can be very helpful to minimize the thermal and creep induced drift. Furthermore the application of closed-loop scanners comprising a positioning control unit will compensate scanning reproducibility problems.

Zero Displacement Tests

The zero displacement tests were performed by 256×256 pixel scans on a Ni-layer on silicon substrate with scans sizes of 10 and $2 \mu\text{m}$ and a line frequency of 1 Hz. The fast scan direction was the horizontal x -direction and noncontact topography data was picked-up in the positive x -direction only in order to eliminate scanner hysteresis effects. The scans were carried out in a series of 15 images using the "repeat" option of the AFM control software, so that non-stop scanning was performed for approximately 1 h on each specimen.

Figure 3.21 gives an impression of the observed system drifts for the sequence of the $2 \times 2 \mu\text{m}$ scans. The particle-like feature marked with an arrow clearly shows the prevailing drift over the image series.

A quantification of the drift can be easily performed by DIC techniques. The image sequences are analyzed by means of digital image correlation with each image being compared to the subsequent one. From the determined displacement fields the following statistical values are extracted:

1. Mean system drift determination over scan-time.

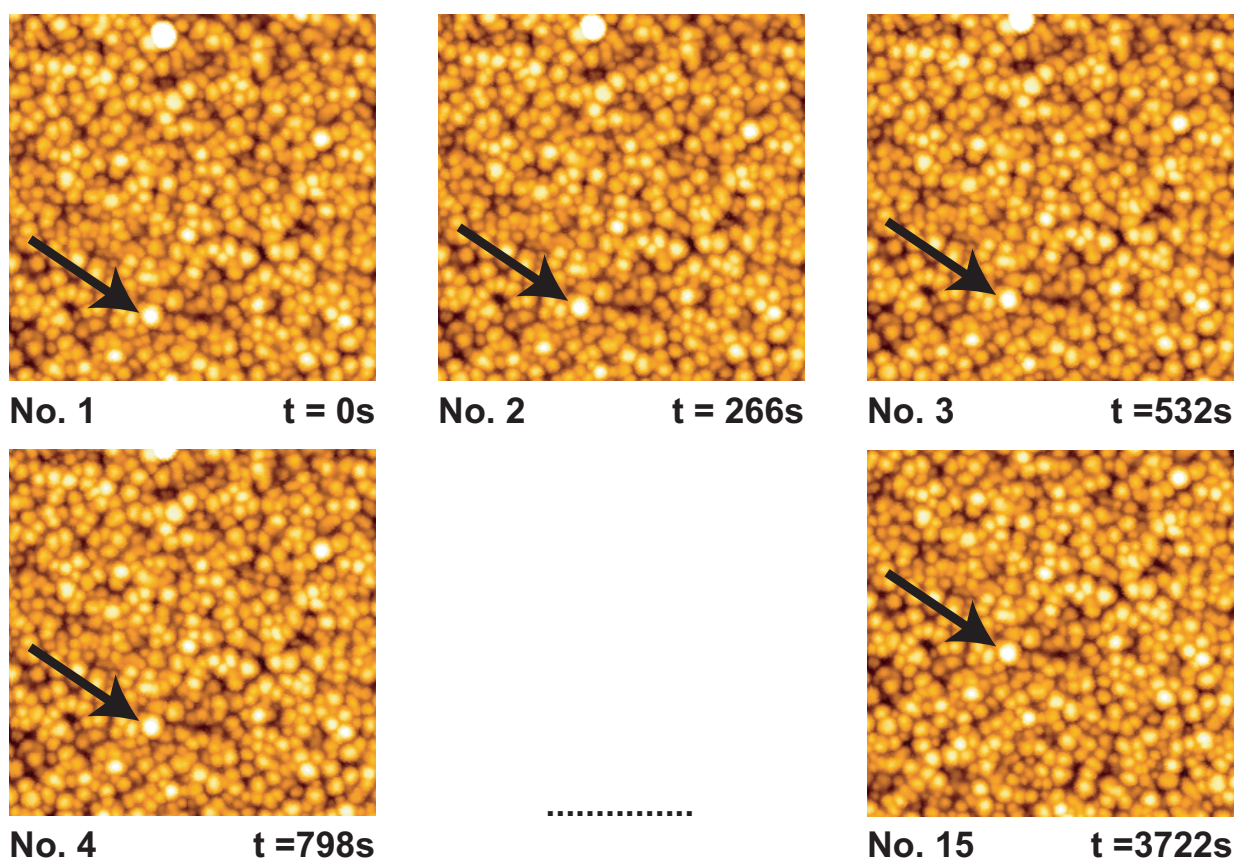


Figure 3.21. Sequence of "zero displacement test" for a $2 \times 2 \mu\text{m}$ scan; z -range: 47 nm .

2. Standard deviation of measured displacement in fast (x) and slow (y) scan direction.

The results of the analysis are presented in Figs. 3.22-3.25 where the evaluation of the mean displacement and standard deviation was carried out separately for the x - and y -direction. Mean displacement values of the analyzed image series over scanning time (Figs. 3.22 and 3.23) clearly emphasize that system drifts can be described with simple polynomial functions. The data was polynomial fitted with a degree of 4 where the graphs of the fitted functions are also shown. The extrapolation from 2 or 3 initial mean drifts to a subsequent image can be achieved with the obtained fitting function. With the calculated mean drift a strain component across the whole image can be calculated so that a pseudo-strain can be eliminated from the actual displacement measurements.

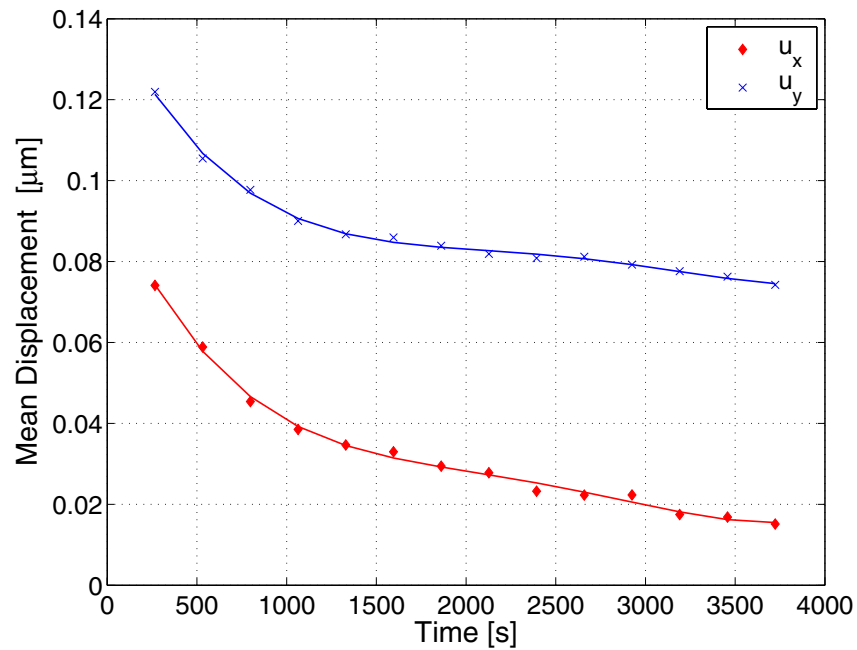


Figure 3.22. Mean displacement, u , in x and y -direction calculated from displacement field vs. scanning time; scansize of image $10 \times 10 \mu\text{m}$.

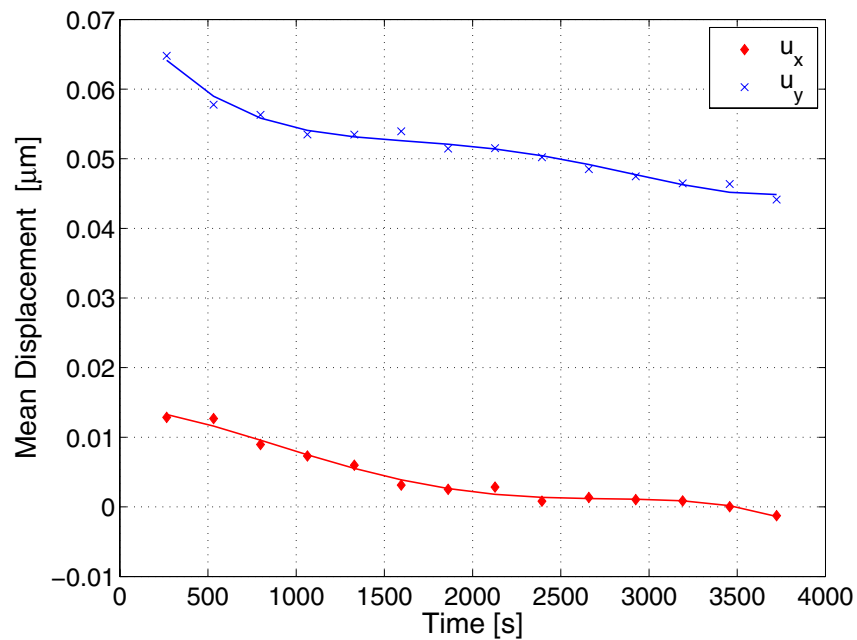


Figure 3.23. Mean displacement, u , in x and y -direction calculated from displacement field vs. scanning time; scansize of image $2 \times 2 \mu\text{m}$.

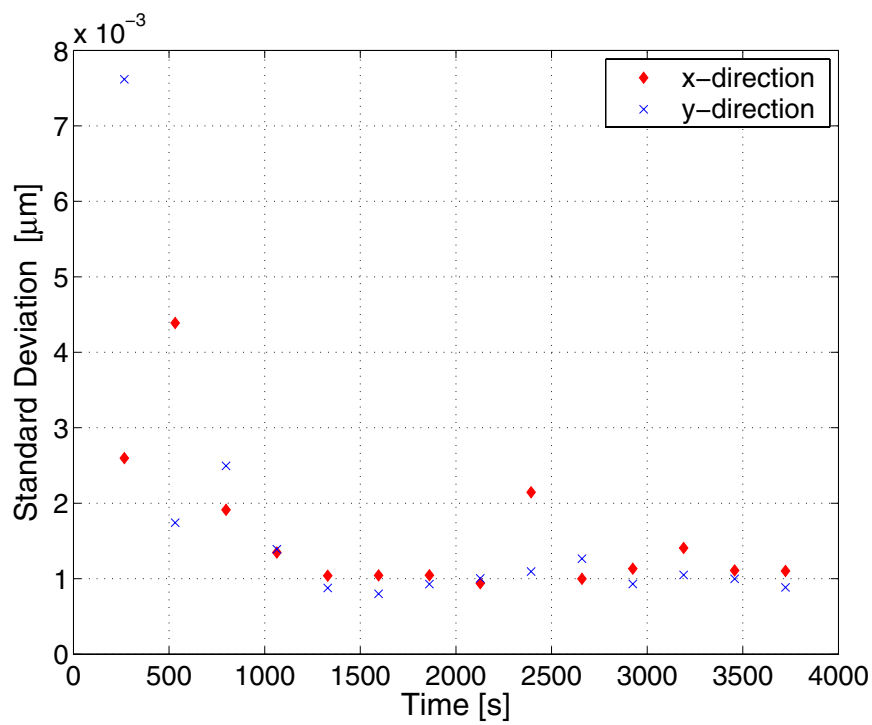


Figure 3.24. Standard deviation of u in x and y -direction calculated from displacement field vs. scanning time; scansize of image $10 \times 10 \mu\text{m}$.

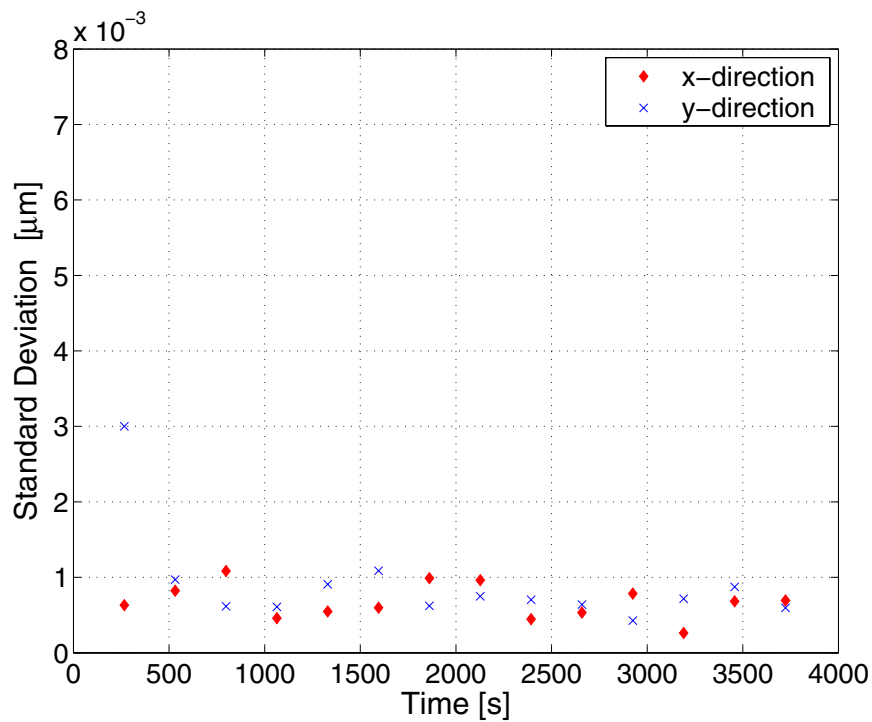


Figure 3.25. Standard deviation of u in x and y -direction calculated from displacement field vs. scanning time; scansize of image $2 \times 2 \mu\text{m}$.

The standard deviation calculation of the determined displacement values was also carried out separately for the x - and y -direction. Figure 3.24 shows that the relative error at the beginning of the $10 \times 10 \mu\text{m}$ zero displacement test is in the range of $\pm 7.5 \text{ nm}$ for the y - and $\pm 2.5 \text{ nm}$ for the x -direction. This is caused by creep effects of the piezo scanner and thermal instabilities. After 5 scans the error is minimized to $\pm 1 \text{ nm}$ for both directions. The outlying values at $\approx 530 \text{ s}$ and $\approx 2400 \text{ s}$ are caused by somewhat obscure scanning instabilities which cannot be explained. For the $2 \times 2 \mu\text{m}$ zero displacement tests (Fig. 3.25) the standard deviation has already decreased down to $\pm 1 \text{ nm}$ after 2 scans. For longer scanning times the error stabilizes between ± 0.25 and $\pm 1 \text{ nm}$.

The discussed results of the error analysis have to be compared to the general accuracy of the DIC analysis. The resolution of DIC for $10 \times 10 \mu\text{m}$ scans with 256×256 pixel is 7.8 nm as calculated by Eqn. 2.3. Zero displacement tests, however, reveal better results so that the value of k for this case of AFM images can be set to a value lower than 0.2 (compare to Sect. 2.2.4). However, it has to be noted that the value for k strongly depends on the experimental conditions (noise, image contrast, ...).

The presented results and the discussion lead to the following statements for system drift evaluation and compensation:

- By the application of the DIC analysis it is possible to quantify system drifts during in-situ loading tests.
- A system drift compensation can be done using the results from the drift analysis.
- Standard deviation values below 1 nm for a scan size of $2 \times 2 \mu\text{m}$ show that pseudo-deformation effects due to scanner instabilities are smaller than the DIC-software resolution.

Alternative AFM Modes for the Application of DIC

For the application of digital image correlation it can be more effective to use images based on error signal or phase detection rather than topography. The error signal is described in Sect. 3.4.1. The advantage of error images is the higher contrast for small scan sizes where "small" strongly depends on the surface roughness and on the signal noise which is responsible for the quality of the image. Within this work, the mechanically polished surfaces have a typical roughness of 15 nm average roughness R_a . The noise of the topography image is typically in the range of several \AA . Below $1 \mu\text{m}$ the error images may give better results for the digital image correlation. A qualified analysis of error image based image correlation is not carried out in this work. Rather than error images, here the emphasis is laid on phase detection microscopy images and their application to DIC. The advantage of the phase signal compared to the topography signal is the additional material stiffness contrast information which is the result of the interaction between the vibrating tip and the specimen surface (compare to Sect. 3.4.1). As for the error images the contrast of a phase image can be better suited for the application of DIC than the corresponding topography image.

Zero displacement tests (described in the previous section) were carried out with an appropriate specimen for phase imaging which is a particle filled polymer composite usually employed as an encapsulant material for electronic applications. Figure 3.26 shows the topography and phase scan of the SiO_2 filled epoxy resin system. The phase image shows relatively large bright areas representing the SiO_2 -components of the composite material.

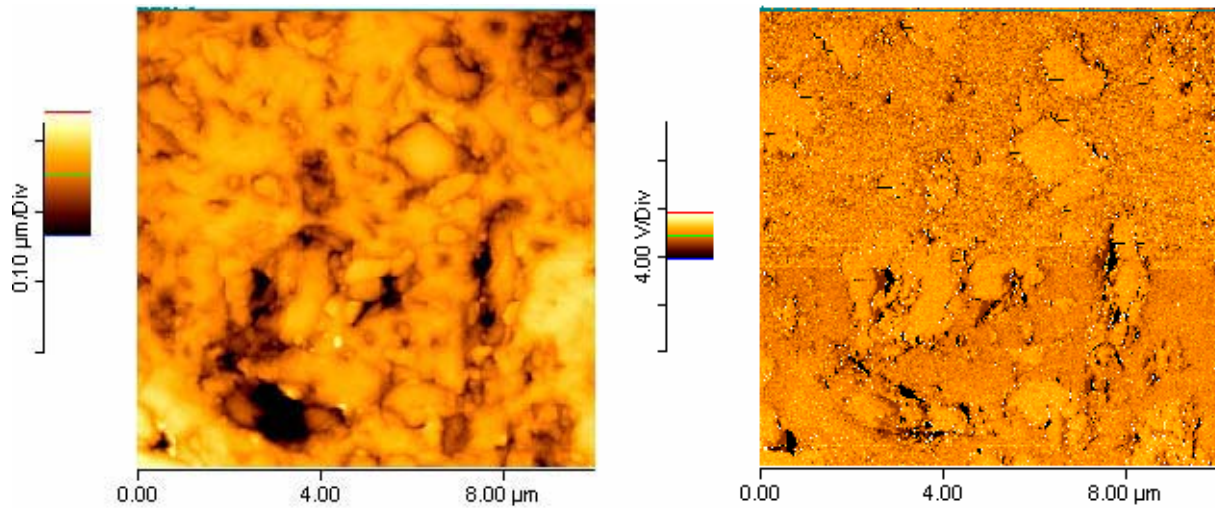


Figure 3.26. SiO_2 filled epoxy system; (*left*) topography image; (*right*) phase image.

The mean displacement values of 5 DIC calculations extracted from 6 subsequent AFM topography and phase scans are shown in Fig. 3.27. Figure 3.28 presents the corresponding standard deviation of the displacement values.

The results show that phase images are principally suited for the application of DIC. Unfortunately, the standard deviation is higher than that for the topography images. This is due to the fact that the stability of the phase signal is not comparable to the topography signal. Filtering techniques will probably improve the accuracy of the DIC application to phase images.

The presented results are discussed in more detail in the master thesis of Nguyen [127].

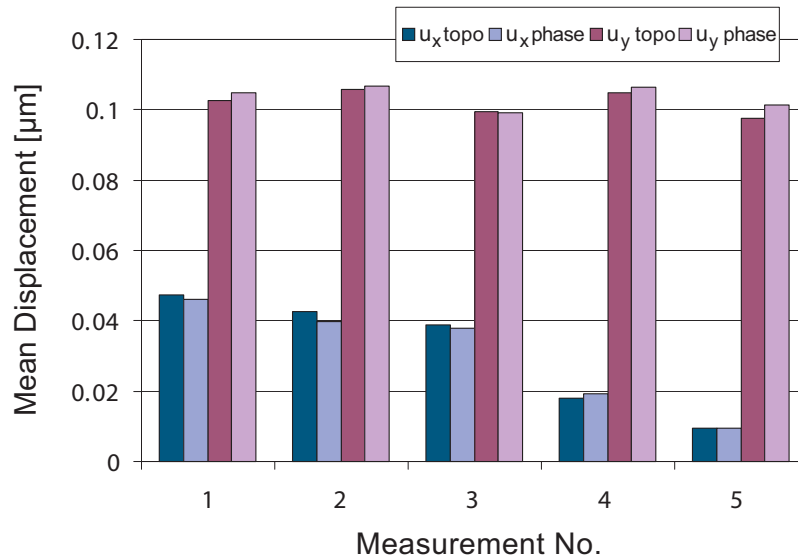


Figure 3.27. Mean displacement values of DIC results extracted from topography and phase images [127].

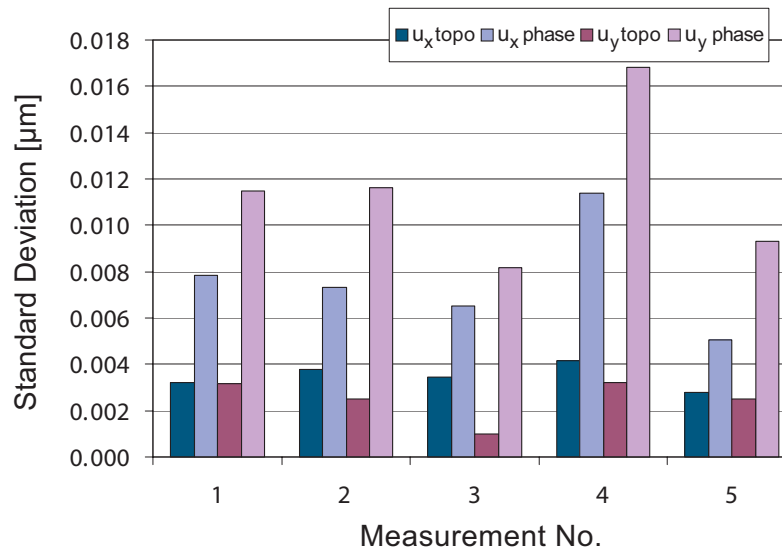


Figure 3.28. Standard deviation values of DIC results extracted from topography and phase images [127].

3.4.4 Results of In-Situ AFM Measurements

The analysis of crack tip behavior by means of AFM based deformation measurement technique should give new insights into the micro- and nanostructural behavior of polymeric materials during loading. For the investigated polymers the question whether continuum mechanics prevail or at what scale other concepts have to be taken into account should be answered with deformation measurements of varying AFM scan sizes. With the strategy of zooming into the vicinity of the crack tip micro- or nanostructural discontinuities of the materials should be detectable.

Therefore, in-situ AFM measurements were carried out at CT-specimens with a specimen width $W = 20$ mm in correlation to the geometry given by Fig. 2.10. The loading was applied in three load steps using the tension/compression testing module (Fig. 3.16). An overview of the load steps and the applied AFM scan sizes are given in Table 3.3.

Table 3.3. *Load steps and scansizes of in-situ AFM crack analysis.*

Load steps	$F_1 \rightarrow F_2$ [N]	Scan size [μm]
1	8.3 \rightarrow 16.4	15×15
2	16.4 \rightarrow 20.7	4.6×4.6
3	20.7 \rightarrow 24.4	2.5×2.5

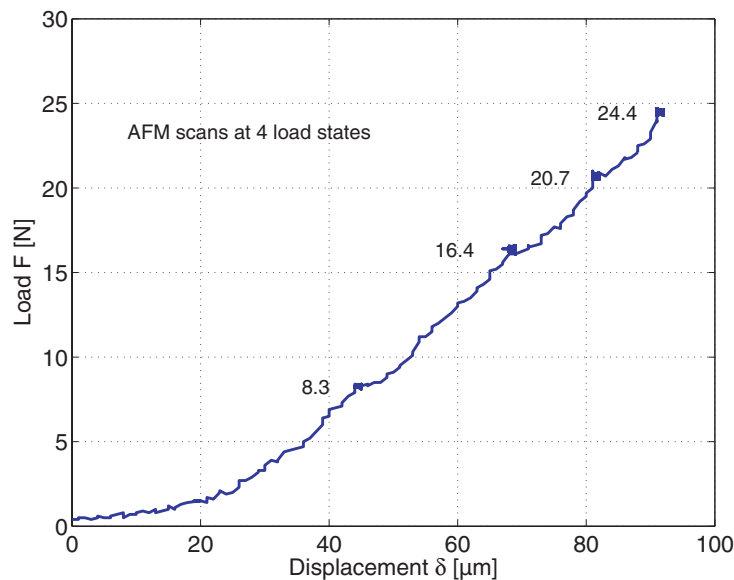


Figure 3.29. *Loading of cynate ester CT-specimen; load states are marked.*

During the AFM scans the drive of the motor was stopped while the load monitoring was carried on. Figure 3.29 shows the complete loading scheme.

Note that "running-in" at the beginning of the load-displacement curve is due to indentation of the loading pins. The graph shows that stopping of the loading process is not a problem for this kind of polymer material. The viscoelasticity has only a small effect on the loading curve so that the stress relaxation is negligible to a certain extent. Nevertheless, the effect of viscoelastic material behavior on the deformation field at the crack tip is analyzed by finite element analysis and a discussion of the results is given in Sect. 4.4.

In the following the crack opening displacement fields (displacement in y -direction) of the mentioned load steps are shown. Digital image correlation analysis of the AFM topography images of load steps 1, 2 and 3 result in the y -displacement fields which are illustrated in Figs. 3.30-3.32. For the load step 3 the DIC analysis was also applied to the error signal images (compare to Fig. 3.33).

The results show the principal capability of the method for crack tip field analysis. From the comparison of Figs. 3.30, 3.31 and 3.32, the down scaling capability is obviously proven. In addition to the presentation of the displacement results obtained from the various load states the crack opening fields are also directly compared to each other. With the assumption of linear elastic behavior the fields of the 2nd and 3rd load state are scaled (with a factor related to the applied loads) where the results originating from the 15 μm scans serve as the reference load state. Figure 3.34 shows the displacement fields from the 1st load state together with the adjusted field from the 2nd load state and Fig. 3.35 shows an analogous presentation of the 2nd and the 3rd field. It is obvious that a complete quantitative agreement of the displacement fields is not given. Possible reasons may be found in an inaccurate loading regime which still has the rotation around the x -axis as a restricted degree of freedom so that an accurate mode I crack opening cannot be achieved. Another source for the inconsistencies may be the existence of material inhomogeneities. In addition the DIC analysis using topographic AFM images of the same object but with different scan sizes are not fully comparable. Depending on the surface topography small images do often not render the required contrast for a high accuracy image correlation.

The comparison of the results of Fig. 3.32 and 3.33 shows that error images are also suited for the application of DIC. The extracted crack opening displacement field as shown in Fig. 3.33 is similar to field calculated from topographical images (Fig. 3.32). Error images of small size areas of surfaces with low roughness value reveal better contrasts than their corresponding topography images. This leads to more accurate results of the applied correlation algorithms. Nevertheless it has to be noted that it is difficult to give an a-priori statement on whether the error or the topography images are better suited for the DIC analysis. The decision has to be taken from case to case what type of analysis results are more trustworthy. For the complete understanding of the accuracy of SPM image based DIC technique, more detailed research will have to be carried out. However, rapid changes in SPM equipment will overcome several findings on this research field.

The presented results and the discussion leads to the following closing remarks for SPM based DIC analysis:

- A minimum variation of the gray values (in the case of topographic AFM images: surface roughness) across the image area is required for a high precision DIC analysis. Note that small kernel sizes can be more accurate for the detection of plastic

deformations than larger kernel sizes due to the fact that with increasing kernel sizes the integration effect will also increase. This means that plastic deformation effects can be smeared out with kernel sizes which are chosen too large.

- DIC results based on different scan sizes are not fully comparable. Data variation (in the case of topographic AFM images: surface roughness) should be similar.
- A complete description of the accuracy of a SPM image based DIC analysis will be a cumbersome procedure. The following parameters have to be taken into account: Data variation of the relevant imaging technique (topography, error, phase, etc.), tip shape, tip to surface interaction (contact or noncontact mode, height), reaction (gain) of feedback loop in z -direction, repositioning accuracy in x, y -direction (linearization problem of piezo)
- New generations of SPMs will overcome several of the described stability and accuracy problems.

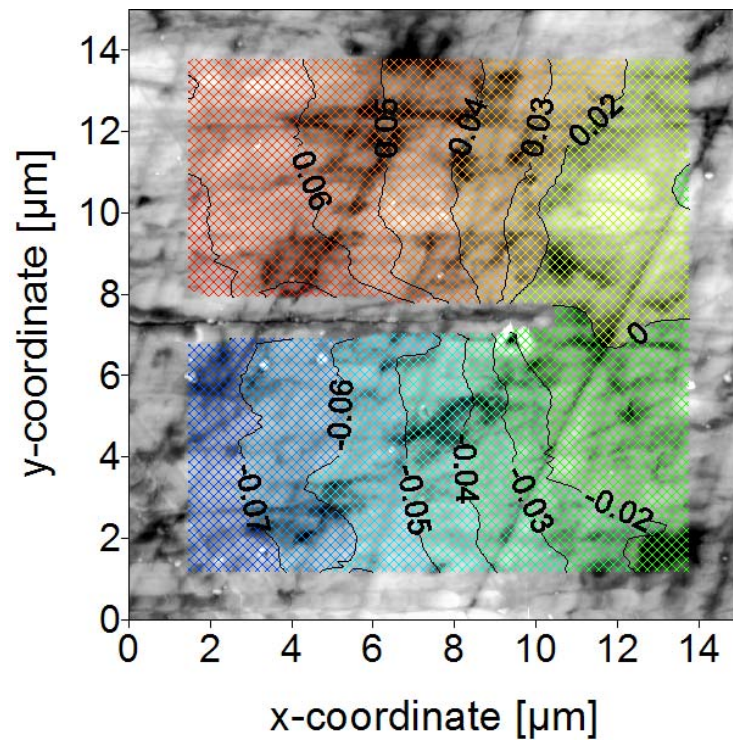


Figure 3.30. Displacement field in vertical direction, u_y , contour-line labels in $[\mu\text{m}]$; AFM image $15 \times 15 \mu\text{m}$, 256×256 pixel, z-range: 357 nm.

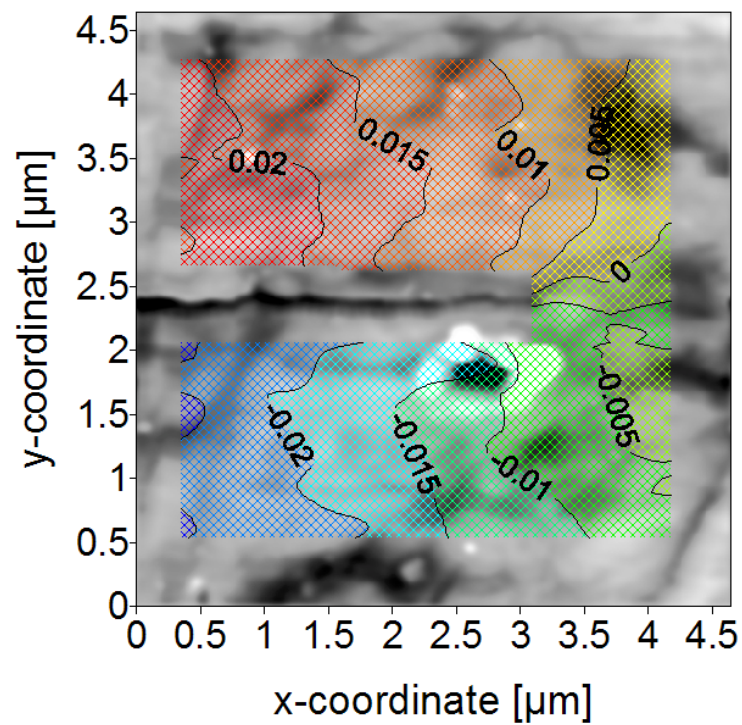


Figure 3.31. Displacement field in vertical direction, u_y , contour-line labels in $[\mu\text{m}]$; AFM image $4.6 \times 4.6 \mu\text{m}$, 256×256 pixel, z-range: 344 nm.

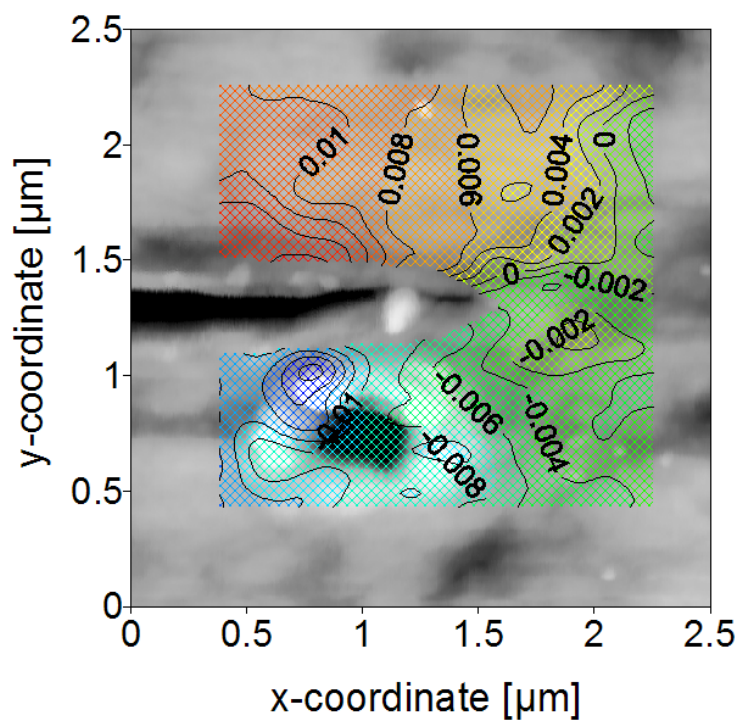


Figure 3.32. Displacement field in vertical direction, u_y , contour-line labels in $[\mu\text{m}]$; AFM image scan size $2.5 \times 2.5 \mu\text{m}$, 256×256 pixel, z -range: 306 nm.

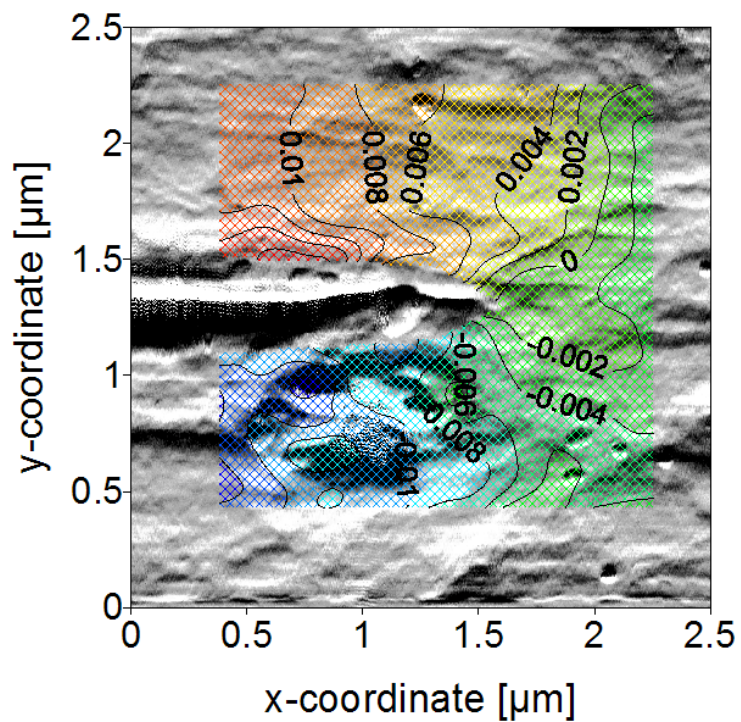


Figure 3.33. Displacement field in vertical direction, u_y , contour-line labels in $[\mu\text{m}]$; obtained by DIC analysis of error signal images; image is taken simultaneously to the topography of Fig. 3.32.

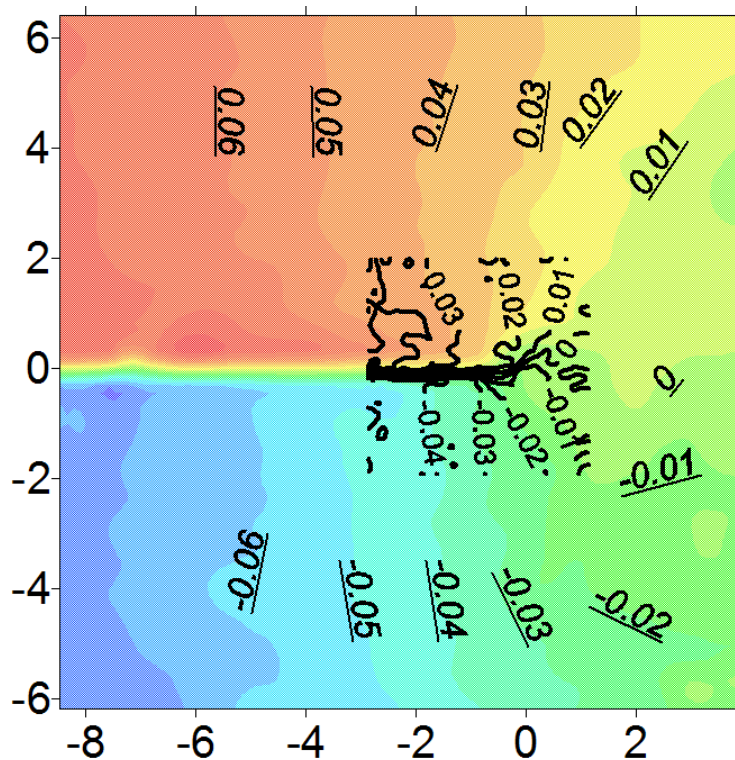


Figure 3.34. Displacement field, u_y , contour-line labels in $[\mu\text{m}]$, for $15 \times 15 \mu\text{m}$ and $4.641 \times 4.641 \mu\text{m}$ scan.

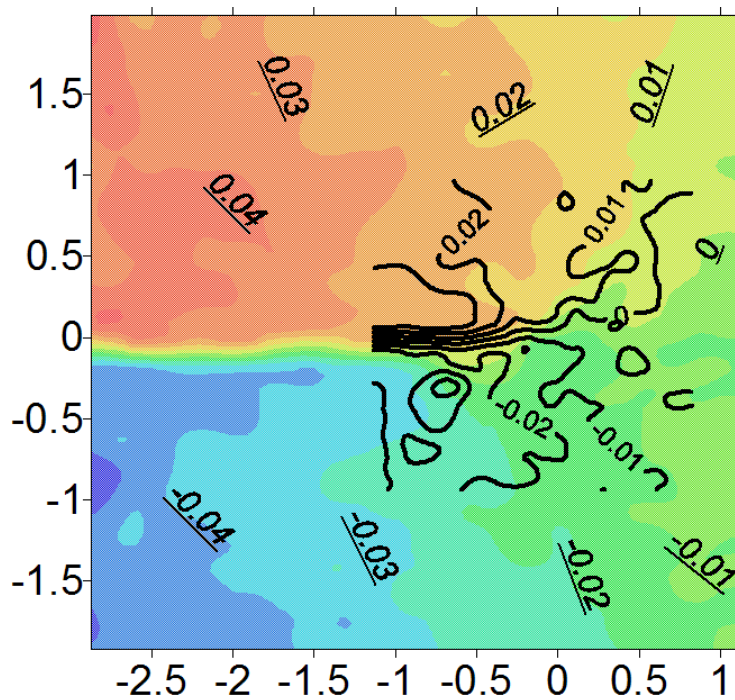


Figure 3.35. Displacement field, u_y , contour-line labels in $[\mu\text{m}]$, for $4.641 \times 4.641 \mu\text{m}$ and $2.5 \times 2.5 \mu\text{m}$ scan.

3.5 Fractography by SEM and SPM methods

In addition to the AFM topography analysis of the fracture surface SEM images were taken. SEM images give a better overview of the fracture processes occurred during crack propagation. Zones of slow or rapid fracture and crack arrest lines can be easily identified.

All SEM images are taken with a tilting angle of 20° to the fracture surface so that only the dimensions in horizontal direction are in correlation with the included scales. Figure 3.36 shows the fracture surface of a cyanate ester CT-specimen. In the image on the left hand side a region of cascade-like markings are observed. A detail of this region is given in Fig. 3.36 (right). This kind of fracture topography is the result of a crack propagation which is driven by a mixed mode loading due to a crack front deflection similar to Fig. 3.12.

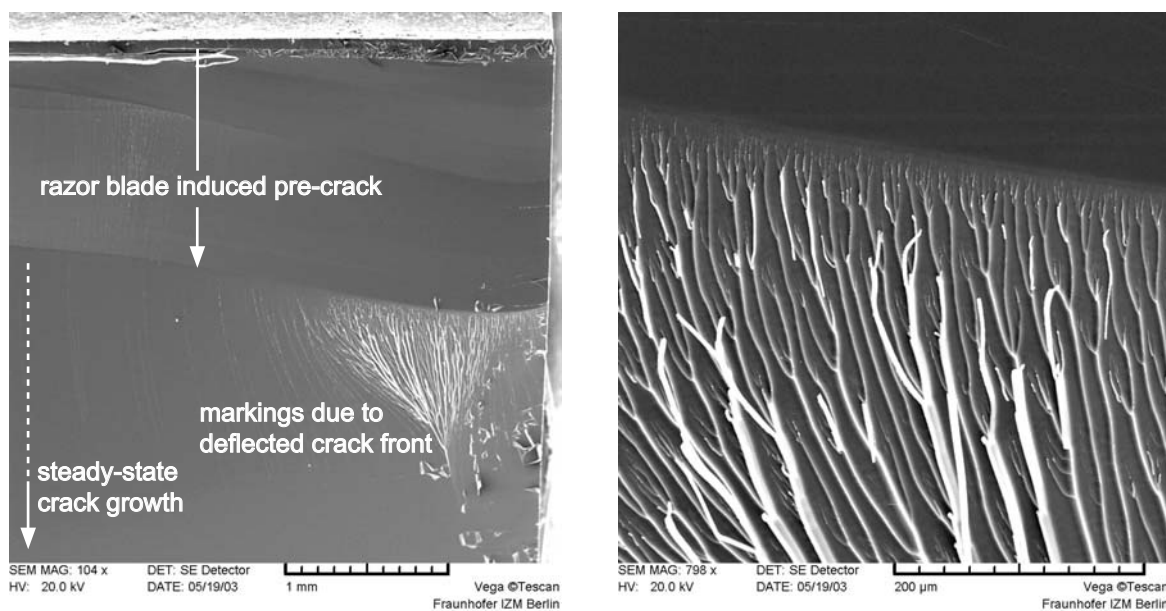


Figure 3.36. Fracture surface of CE CT-specimen; (**left**) overview of the crack initiation zone, steady-state crack propagation is achieved at the bottom of the image; (**right**) detail of markings caused by a deflection of the crack front in y -direction.

Figure 3.37 shows an overview (left) and a detail (right) of the fracture surface formed by steady-state fracture propagation. It has to be noted that the crack surface is very smooth. Topographical fracture features at the micro scale cannot be observed. In contrast to the smooth crack propagation of the neat CE resin the fracture surface of the rubber modified CE shows topographic features which are stretched in crack growth direction (compare Figs. 3.37 and 3.39). Although the crack propagation of the rubber modified CE occurs in a stick-slip type, there are no significant topographic differences between the surface formed during steady state crack propagation and that during crack jump.

SEM images of the crack tip opening taken just before the crack propagation clearly shows the difference between the neat and the rubber modified CE (Fig. 3.40). The response of

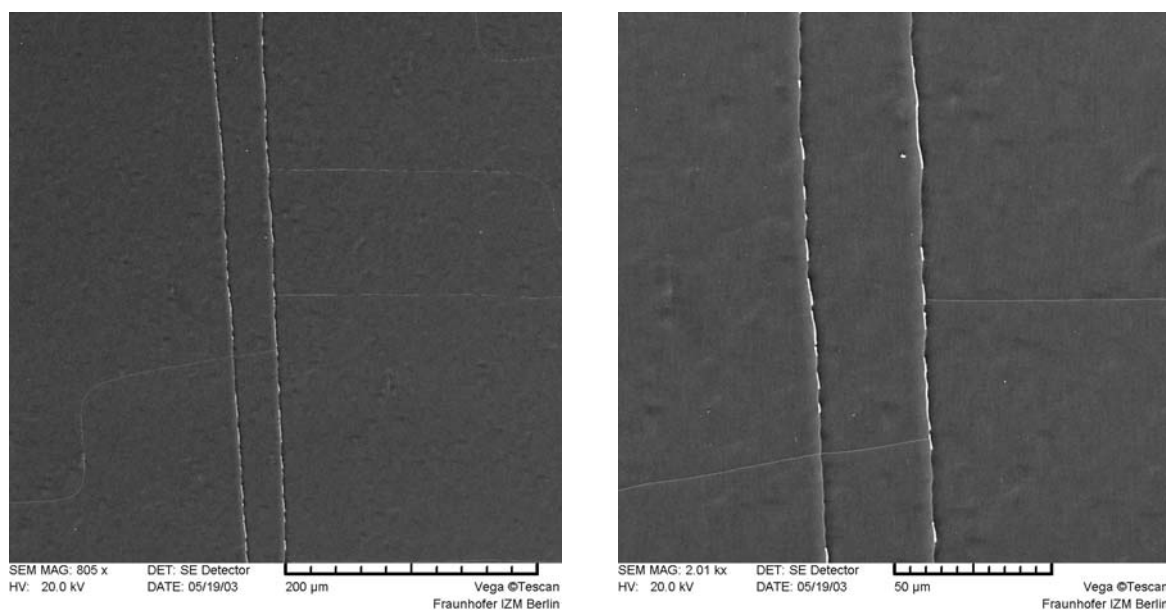


Figure 3.37. *Region of steady-state crack growth at CE fracture surface, note that the horizontal and vertical lines are not fracture features, but caused by cracks in the carbon sputtering layer; (left) overview; (right) detail.*

the blended thermoset system to the critical loading is accompanied by the effect of crack tip blunting. Traces of the blunting are also visible after a small crack propagation (Fig. 3.41). The microcracks at the crack faces may originate from residual stresses induced by mechanical polishing of the surface. They cannot be identified as crazes.

In addition to the SEM observations AFM tapping mode phase image scans were carried out at the crack surface of a neat and rubber modified CE specimen. Unfortunately, different phases could not be identified in a reproducible and reliable way so that the results are not shown in this work. The reason might be that the dimensions of the phases are too small (in the nm range) for a reliable SPM-based detection and/or the variation in mechanical properties of the two phases is too low to obtain a significant shift of the phase signal. Other researchers [16] identified different phases (in the micrometer range) by phase detection microscopy at fracture surfaces of similar material systems. Therefore, further research on fractography approach by SPM techniques has to be done. A variety of different SPM analysis modes such as AFAM or UFM are available from different manufacturers and research groups. Depending on the material class, the one or the other method will be promising. Nowadays, a universal SPM method for the determination of qualitative and quantitative mechanical properties is not established. Another promising approach for the detection of different phases of the discussed rubber modified CE is the application of transmission electron microscopy (TEM).

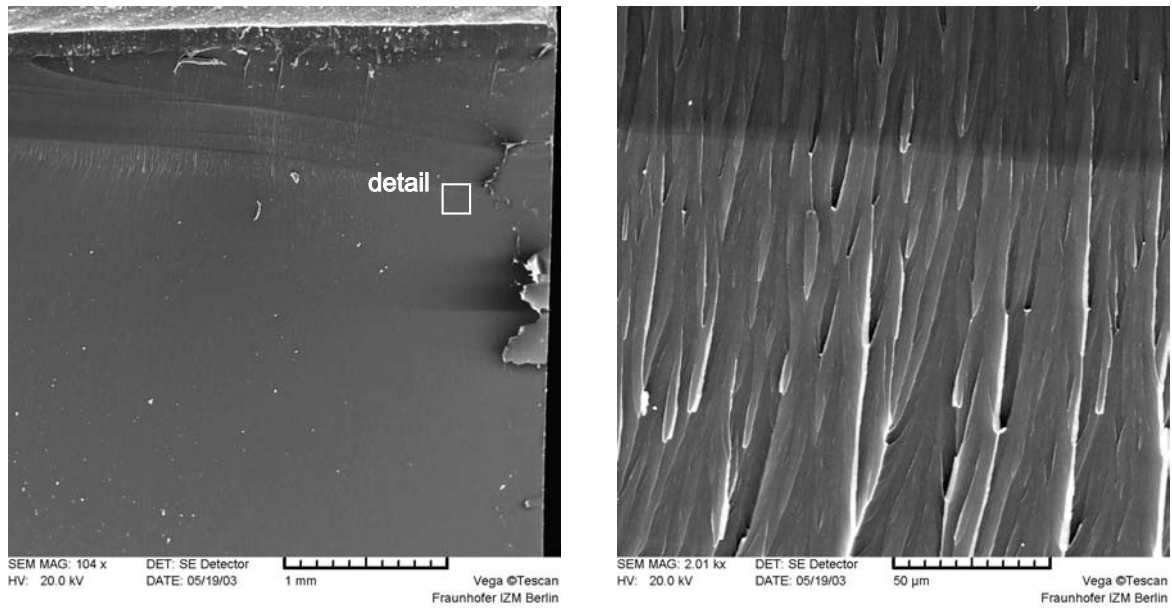


Figure 3.38. Fracture surface of rubber modified cyanate ester resin; (left) overview, several crack arrest lines from razor blade pre-crack are visible in the upper part of the image, the flake like features on the right hand side of the image are caused by cracks in the carbon sputtering layer; (right) detail, starting line of rapid fracture propagation.

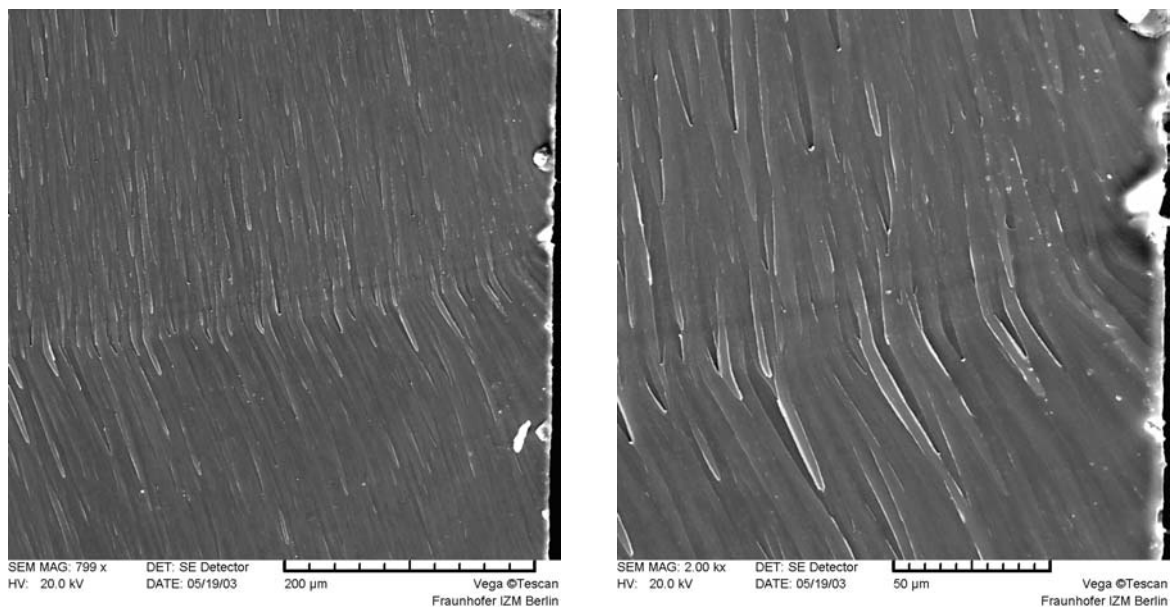


Figure 3.39. Fracture surface of rubber modified cyanate ester resin; crack arrest line, a small region of steady state crack growth and starting line of rapid crack growth are shown; (left) overview; (right) detail.

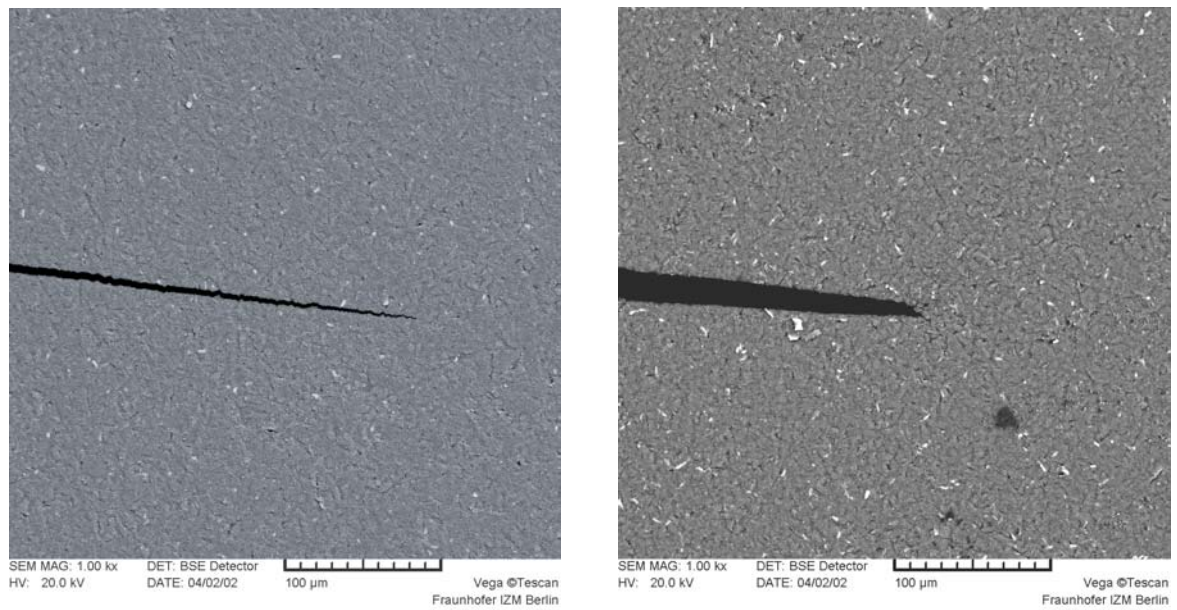


Figure 3.40. Crack tip opening before fracture of (*left*) neat cyanate ester resin and (*right*) rubber modified cyanate ester resin.

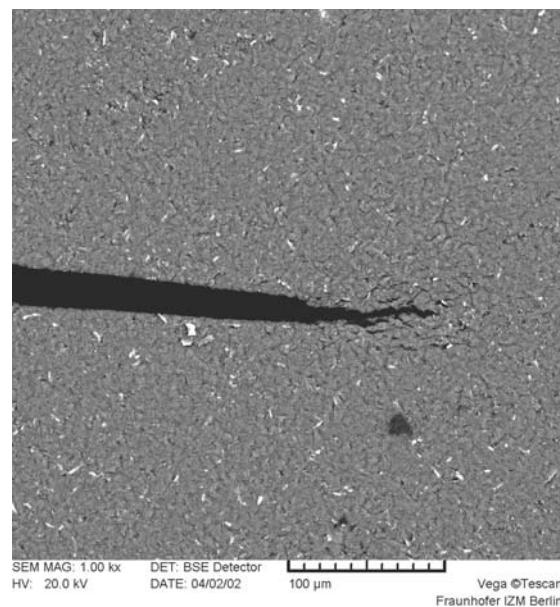


Figure 3.41. Crack tip after a small crack propagation of rubber modified cyanate ester resin; traces of crack tip blunting are visible; the microcracks at the crack faces are possibly caused by stresses induced by mechanical polishing of the surface.

Chapter 4

Discussion - Comparison of Experiment and Simulation

The verification of numerical reliability estimation of a microelectronic system by the application of experimental techniques is a fundamental task. Due to the fact that in many cases experimentally derived material properties are not available for structural components having one or more dimension in the range of nanometers the inversion of this approach is of major interest for nanotechnological devices of the future. If material properties of a system component cannot be validated by an appropriate measurement technique the DIC-based displacement analysis enables a better understanding of the thermomechanical material properties. For example a new technological process for the fabrication of thin films may change the material behavior dramatically (e.g. isotropic to anisotropic, linear elastic to plastic, etc.). In such cases, a comparison of FE-results with strain field measurements and recursive material model variation of the FE-model leads to improvements of the reliability simulation. The ongoing development of fully parameterized FE-modeling techniques will facilitate this approach [128].

Due to the fact that the importance of the combination of simulation and experiments will increase for future developments of microelectronic systems, MEMS and NEMS a powerful reliability assessment tool is necessary. Starting with an analytical crack evaluation concept (Sect. 4.1) the main focus of this chapter is laid on the definition and implementation of a hybrid analysis tool combining SPM based experimental displacement measurements and finite element concepts (Sect. 4.6). The basis of this strategy is an adaptation concept which will be discussed in detail.

Throughout this chapter, the developed concepts are consistently applied to the measurements carried out at the CT-specimen discussed in Sect. 3.4.4.

4.1 Crack Opening Displacement Analysis

The classical stress intensity factor K is conventionally determined by means of macroscopic fracture tests at standardized fracture specimens such as the CT-specimen. A straightforward approach for crack evaluation by means of AFM images is the technique of crack opening displacement (COD) determination.

In order to determine the mode I stress intensity factor K_I crack opening displacements u_y^u and u_y^l are measured along both the upper and lower crack boundaries.

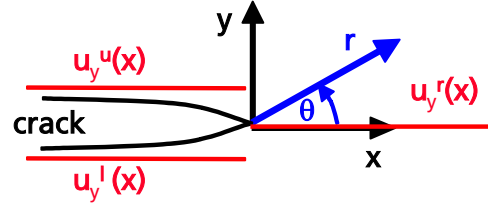


Figure 4.1. Crack opening displacement according to LEFM for infinite bulk material and mode I crack opening.

If determined by linear elastic fracture mechanics they must equal to

$$u_y^{u,l} = \pm \frac{K_I}{2\mu} \sqrt{\frac{x}{2\pi}} (\kappa + 1) \quad x \leq 0 \quad (4.1)$$

$$u_y^u = u_y^l = 0 \quad x > 0 \quad (4.2)$$

where μ is the shear modulus and κ is a function of Poisson's ratio, ν (compare to Eqns. 2.7 and 2.8). Taking the square of the difference of upper and lower displacements, we obtain a linear function of the x -coordinate or 0, depending on the position relative to the crack tip:

$$\left(\frac{u_y^u - u_y^l}{2} \right)^2 = Cx \quad x \leq 0 \quad (4.3)$$

$$= 0 \quad x > 0 \quad (4.4)$$

The expression of Eqn. 4.3 does not change if specimen rotation due to inaccurate loading is included into the considerations. In this case, equal rotational terms on both sides of the crack boundary are subtracted from each other. For the equation above, the crack tip is set at location $x = 0$. The crack tip location on the real specimen can be found at the interception of a linear fit of the curve Cx with the x -axis. The slope C allows to estimate the stress intensity factor K_I , which is a measure of the crack tip load. It is given by:

$$K_I = \frac{E}{1 + \nu} \frac{1}{\kappa + 1} \sqrt{2\pi C} \quad (4.5)$$

The discussed analysis is applied to the measurements presented in Sect. 3.4.4. The results for the $15 \times 15 \mu\text{m}$ scans are shown in Fig. 4.2.

The determined value for K_I with the application of Eqn. 4.5 and the assumption of the plane strain solution equals to $0.056 \text{ MPam}^{1/2}$. The value calculated from the applied loads is $0.085 \text{ MPam}^{1/2}$. The comparison shows that the value calculated from the specimen loading is 1.5 times higher than the value extracted from the crack opening field.

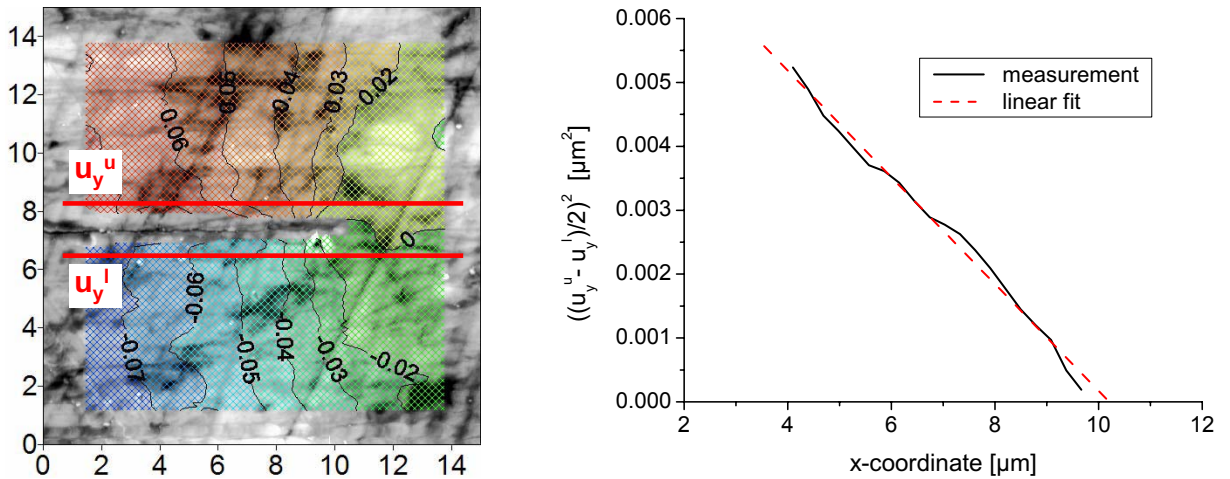


Figure 4.2. (left) AFM image of crack tip area (size: $15 \times 15 \mu\text{m}$) with overlaid displacement results in y -direction, u_y ; lines for the upper and lower crack face are also shown (right) evaluation of slope C for the calculation of the stress intensity factor K_I .

Possible reasons or error sources for the deviation are:

- the value of the measured Young's modulus is too low for this CT specimen so that the field determined K_I -value is also underestimated,
- the crack is not fully loaded at the surface of the specimen, due to the fact that (in this case) the crack front is a relatively straight line normal to the specimen surface,
- the evaluation of the slope Cx is based on displacements of the upper and lower crack face which are extracted from DIC results. The distance of the corresponding lines (compare to Fig. 4.2) to the crack face is not zero so that the calculated slope and the stress intensity factor is lower than the actual value.
- the plane stress or strain crack field solution is not accurate or is not completely predominating at the surface of the specimen.

Concluding the results discussed in this section, a detailed analysis of the crack tip behavior by FE simulation is necessary.

4.2 Finite Element Model

In order to compare SPM measurements with numerical solutions based on finite element method the problem of a wide range of element sizes (from the mm- to nm-scale) has to be taken into account. For modeling the surrounding of the crack tip a very fine mesh is necessary compared to the global size of the CT-specimen. Small element edges in the x - y -plane in combination with a coarse mesh in the z -direction will cause element shape

problems. For accurate numerical results an element edge size ratio not lower than 1/10 has to be achieved. The problem can be solved by the submodeling technique which was applied to several numerical calculations presented in this chapter. An illustration of the created FE model is given in Fig. 4.3.

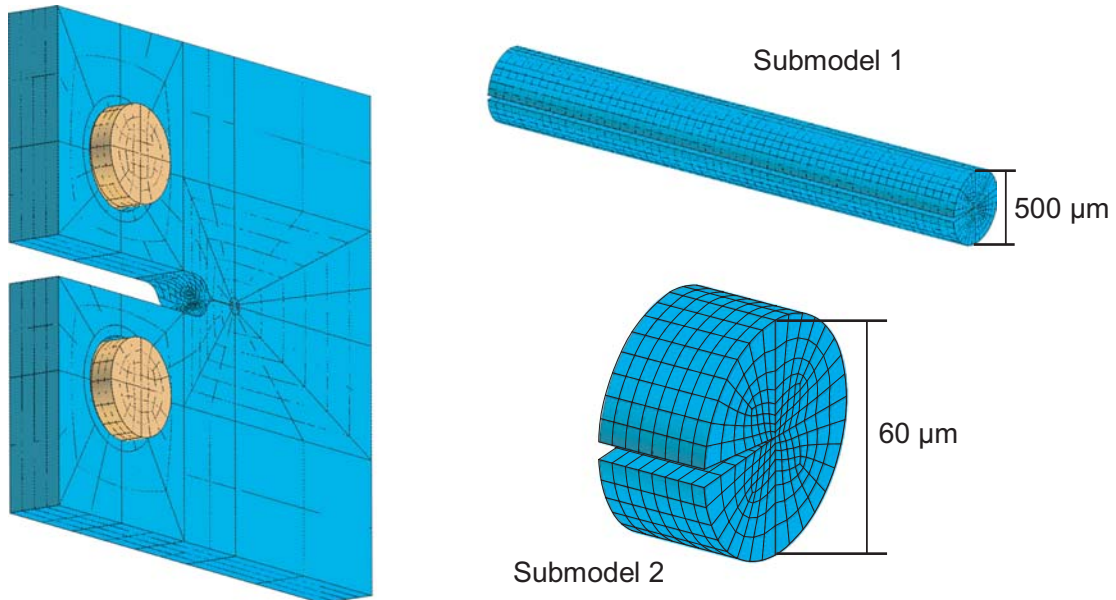


Figure 4.3. Principle of submodeling technique for accurate modeling of the crack tip, as applied to PATRAN/ABAQUS FE-models.

The CT-specimen is modelled in a global model with the relevant boundary conditions (force or displacement) applied to the loading pins and a solution is computed with the FE-solver (ABAQUS, ANSYS). A local model is built up in the surrounding of the crack tip using the same coordinate system as the global model. Afterwards, the cut boundary with the global model is determined and the nodal displacement solution of the global model (at the cut boundary) is transferred to the local model arranging the boundary condition for the second solution process. In general, the FE-software interpolates the displacement values from the coarse global mesh to the finer local mesh. This is the key for the implementation of a submodeling technique. A nesting of submodels can also be performed.

The actual FE approach of the CT-specimen is built up by two step submodeling. The first local mesh models the crack front boundary over the complete specimen thickness B . In a second submodel, only a small volume at the surface is redefined with a finer mesh (Fig. 4.3) enabling the adaptation of the FE-mesh to the in-situ loading experiments. A detailed description of the mesh interface for a quantified comparison of numerical and experimental approaches is given in Sect. 4.6.2.

In the following sections, several numerical results are presented basing on the discussed or slightly modified model. The applied modifications are summarized as follows:

- Variation of crack front curvature from a straight to a curved shape.

- Modification of material model from linear-elastic to viscoelastic.
- Modification of material model from linear-elastic to plastic.

The intention behind these modifications and the corresponding results are presented throughout Sect. 4.3 - 4.5.

4.3 Crack Front Curvature

The crack front of a CT-specimen with finite thickness tends to form a curvature such that the crack in the middle of the specimen is running ahead of the crack front at the edge of the specimen, Fig. 4.4 (left). This is the result of the three dimensional character of the crack tip stress field. At the edge of the specimen the material can expand in the z -direction whereas in the middle the expansion in z -direction is restricted to a large extent. This phenomenon is often [82] described as prevailing state of plane strain (in the middle of the specimen) and plane stress (at the surface of the specimen).

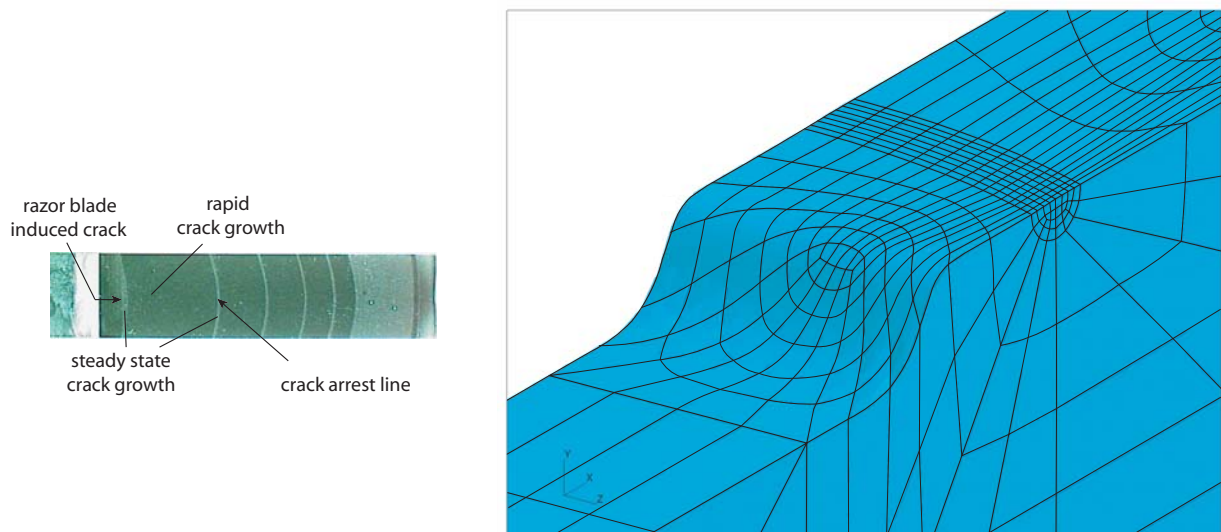


Figure 4.4. Curved crack front at CT-specimen (**left**) For a (rubber modified) thermoset material, crack initiation and crack arrest lines after rapid crack propagation are observed (stick-slip); (**right**) FE-model of CT-specimen with curved crack front.

The effect of the crack front curvature is analyzed by a modified FE-model as illustrated in Fig. 4.4 (right). The global boundary conditions of the FE model are not modified. The curvature is modelled by a polynomial function of order 2, with the x -direction of the crack tip at the specimen surface for straight and curved crack front being identical. In the middle of the specimen the crack front is running 0.5 mm ahead compared to the specimen surface. This value was typical for the modified cyanate ester resins as it is illustrated in Fig. 4.4 (left).

In an FE-analysis the effect of the formation of the crack front curvature can be analyzed by means of energy based integral calculations such as the J -integral (Eqn. 2.17). Figure 4.5 shows the value for the J -integral over the thickness coordinate z (compare to Fig. 2.7) for a straight and a curved crack front.

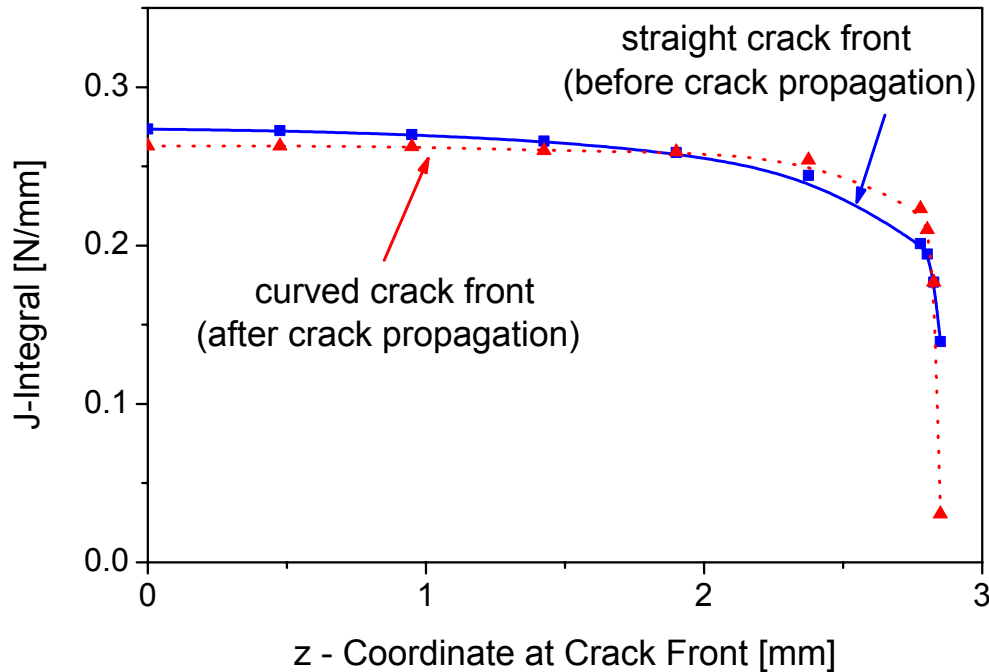


Figure 4.5. J -integral vs. z -direction for a straight and a curved crack front.

For both numerical solutions the J -integral varies with the location at the z -direction of the specimen. The largest value is observed in the middle of the specimen ($z = 0$) from where it is steadily decreasing towards the specimen surface. This means that the crack growth will be initiated in the middle of the specimen followed by the specimen edges. With a curved crack front the variation of the J -integral towards the edge of the specimen is reduced (Fig. 4.5). The crack driving energy is becoming balanced over the crack front to a large extent. However, it has to be noted that the crack front as it is modeled in this analysis (polynomial function of order 2) is not identical with the actual experimental crack front. This approach is only valid to show tendencies of crack front curvature formation. More accurate modeling of the crack front curvature may lead to better balance of the J -integral over the z -direction.

Besides the formation of the crack front curvature, the effect of a present curved crack front on the experimental approaches of this work has to be analyzed. Regarding the applied measurement techniques of OCT and DIC two effects have to be taken into account:

- Effect of curved crack front on the measured R -curve at the beginning of the fracture process. – The straight crack front induced by tapping of a razor blade is the result of a rapid crack propagation. Therefore, the crack front is not equivalent to the curved crack front during a steady state or stick-slip type of crack propagation.

- Effect of curved crack front on the crack tip field at the specimen surface due to the fact that the crack front is tilted to the normal of the specimen surface.

4.3.1 Effect of Crack Front Curvature on R-Curve

Figure 4.6 shows the load displacement curves for an ideal straight and a curved crack front (pre-running in the middle of the specimen: 0.5 mm) where the crack length at the edge of the specimen is identical.

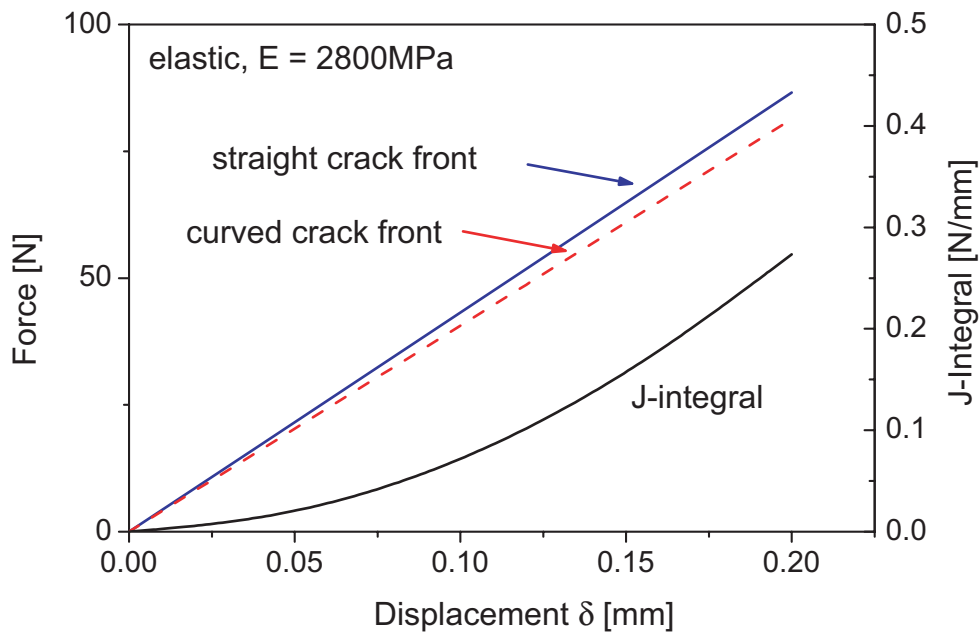


Figure 4.6. *Effect of curved crack front on the load-displacement curve.*

The effect on the loading for mode I crack opening is in the range of 6.4% leading to an equivalent error in the fracture toughness value. This effect is included in a measured R -curve and can be detected at the critical value where the load value is constant for a short time phase although the drive of the loading is moving constantly. It can be described as a "running-in" of the R -curve (compare to Fig. 3.10 (left)). Compared to an error caused by a step-like pre-crack as discussed in Sect. 3.3.2, Fig. 3.12 and 3.13, the crack curvature influence is relatively low. Nevertheless, this result clearly emphasize the advantage of the R -curve measurement in comparison to ASTM D5045 where the K_{Ic} value is determined from a single crack initiation point. However, the results show that in practice the OCT measurement values have to be adjusted by a correction factor for crack front curvature. It has to be mentioned that these conclusions hold true only for CT-specimens of similar thickness B and linear-elastic material properties.

4.3.2 Effect of Crack Front Curvature on Crack Tip Field

For the measurement of deformation fields at specimen surfaces the curvature of the crack tip cannot be neglected. Göken and Vehoff showed by FEA that displacement fields can be significantly influenced by the angle between the crack front and the specimen surface [21, 22]. Figure 4.7 shows the results of FE-analysis calculated with a straight and a curved crack front. In the middle of the specimen the crack front is running 0.5 mm ahead compared to the specimen surface leading to an angle of 19.3° between the crack front and the normal of the surface area.

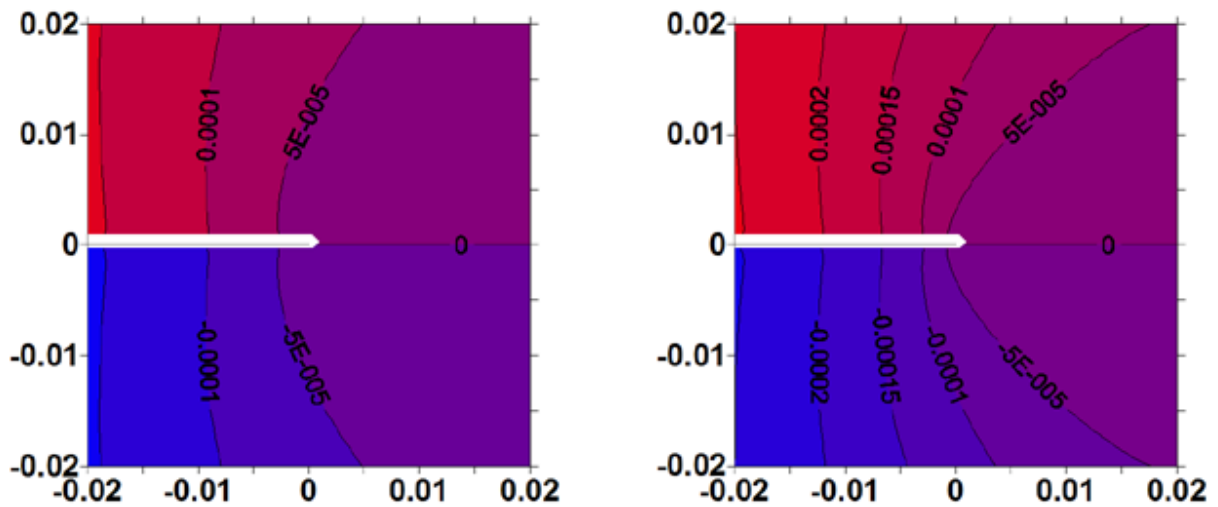


Figure 4.7. Crack tip displacement field in y -direction, u_y in [mm]; **(left)** straight crack front; **(right)** curved crack front.

The comparison of the fields show that the displacement values at the crack field are 1.7 times higher for the FE calculation based on a curved crack front. This result is in correlation with the J -integral across the specimen thickness, (compare to Fig. 4.5). The loading of the crack front at the surface is lower for a straight crack than for a curved crack. This result clearly emphasizes that an accurate crack evaluation by experimental methods has to be verified by finite element simulations with models representing the actual geometry of the specimen with a high accuracy.

4.4 Influence of Viscoelasticity on Crack Tip Field

The question of the effect of a viscoelastic in comparison to an elastic model is answered by simulation. FE calculations were carried out with the model of Fig. 4.2 and viscoelastic material model as defined in Sect. 3.2.5.

For the chosen materials the effect of viscoelasticity on the loading and the crack tip field is negligible. Due to the fact that the results are nearly the same (effect below 0.1%) they are not presented in this work.

4.5 Influence of Plasticity on Crack Tip Field

At the crack front of polymer materials, several failure modes such as blunting effects, crazes, microcracks, microvoids may be observed. Although these effects were not observed in the performed SPM measurements an estimation of the size of the plastic zone is carried out. Therefore, a numerical simulation is performed with an FE-model analogous to Fig. 4.3 where the material model is defined including perfect plasticity with a flow stress of 50 N/mm^2 . The corresponding stress-strain curve of the material model is defined as illustrated in Fig. 4.8 (left).

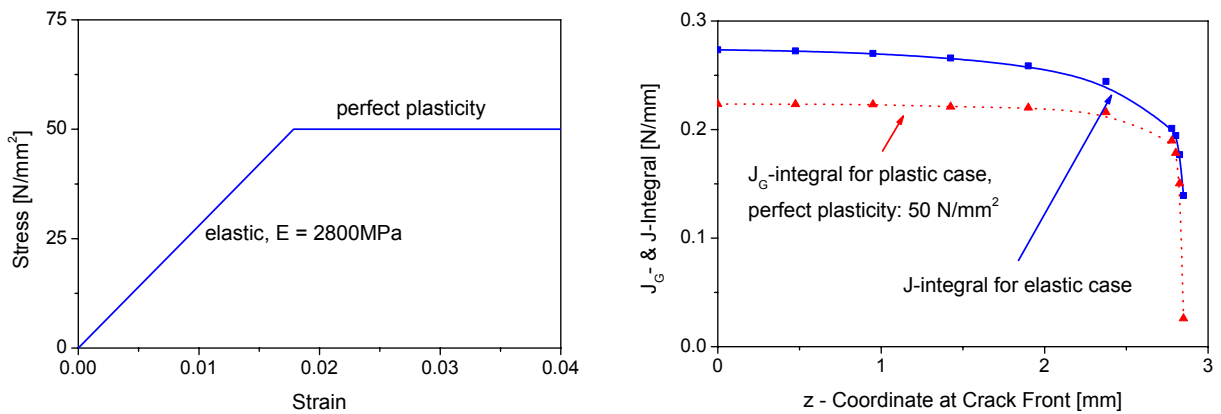


Figure 4.8. Material model for perfect plasticity. Effect of plasticity on J -integral along the crack front.

The effect of plasticity on the crack front behavior is analyzed by a generalized J -integral approach developed by Ghavifekr [91] (compare to Eqn. 2.18). The results are shown in Fig. 4.8 (right).

Similar to the effect of crack front curvature formation also plasticity causes the "flattening" of the J -integral over the specimen thickness. This is the result of the ability to react with large inelastic strains. However, in this work prevailing of a large plasticity zone was not verified by the experimental displacement field measurements.

Figure 4.9 shows the von Mises stresses around the crack tip at the specimen surface extracted from linear-elastic simulation. The results are presented for a loading of $F = 86 \text{ N}$ which is already above the fracture toughness of the actual cyanate ester resin. At the surface of the specimen the plastic simulation did not show a significant influence on the stress field so that the numerical results are not shown here. However this underlines the experimental observation that a plastic zone was not detected by the application of DIC to the crack tip images obtained by AFM.

A comparison of von Mises stresses of the CT-specimen based on linear-elastic and plastic material model are given in Fig. 4.10 and 4.11. As the coordinate systems indicate the Figs. illustrate the stress solution of the center of the specimen where the effect of plasticity is obviously more evident. With the assumption of perfect plasticity the size of the plastic zone at the crack tip would be in the range of $1 \mu\text{m}$ (compare to Fig. 4.11). Such a large

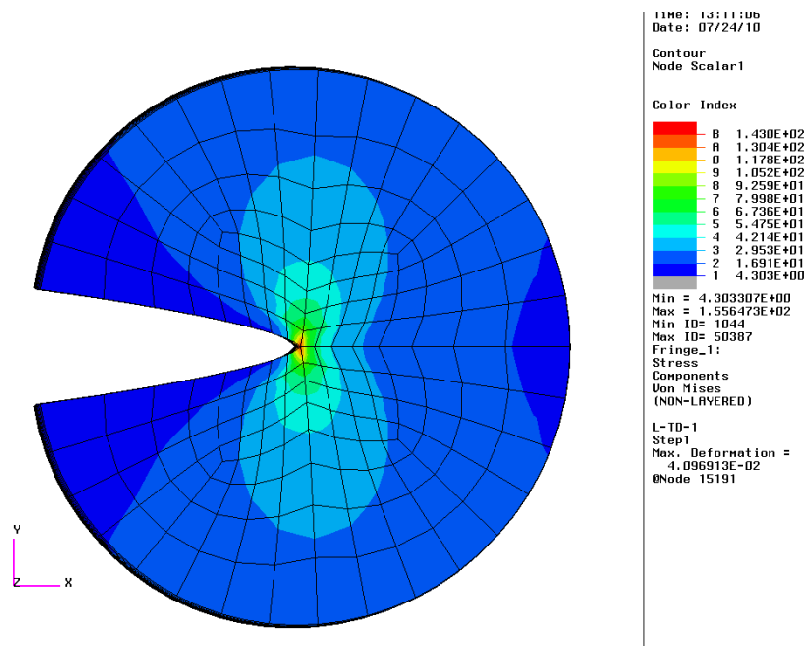


Figure. 4.9. *Von Mises stress at crack tip at specimen surface for linear-elastic simulation.*

plastic zone was not detected in the SPM experiments. This result also correlates to the fractographic analysis (compare to Sect. 3.5) of the fracture surface revealing no indication for the formation of a plastic zone in the μm range.

The conclusion of the experimental approach and the verification with FE-results clearly emphasize the predominating linear-elastic material behavior of the investigated cyanate ester resin.

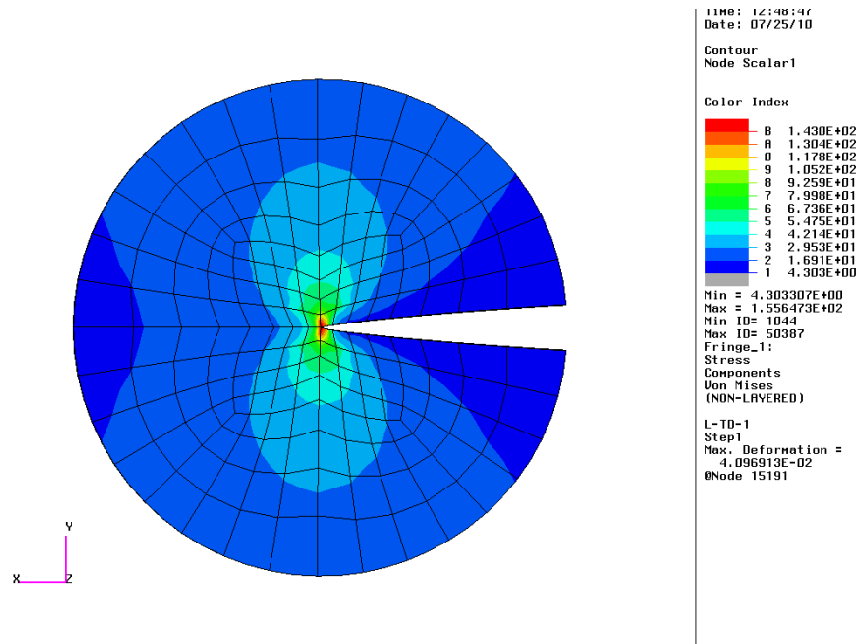


Figure 4.10. Von Mises stress at crack tip in the middle of the specimen for linear-elastic simulation.

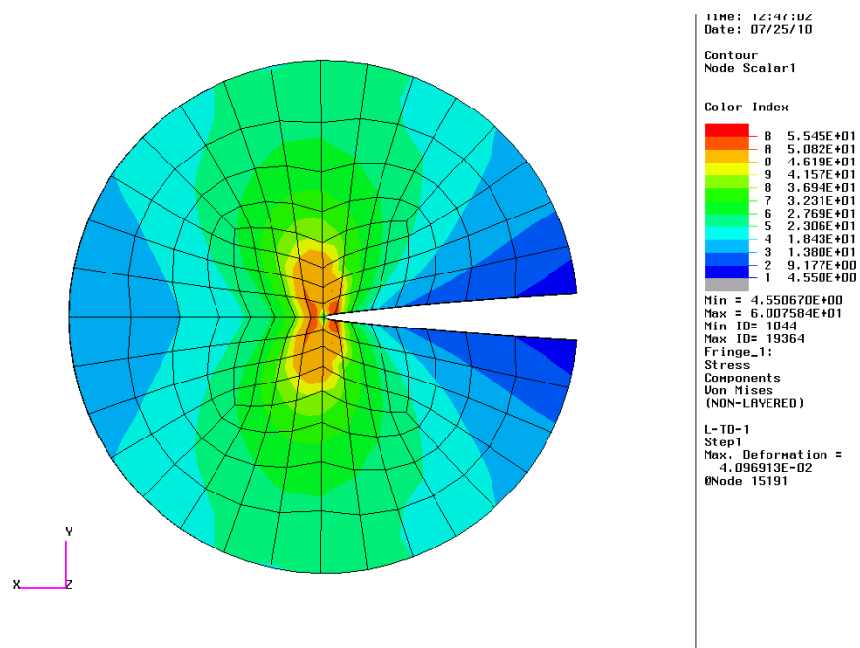


Figure 4.11. Von Mises stress at crack tip in the middle of the specimen for plastic simulation; a plastic zone of $\approx 1 \mu\text{m}$.

4.6 Adaptation Strategies between Simulation and Experiment

The presented FE-results of the previous sections clearly underline the difficulties involved in the experimental crack tip evaluation at the micro and nanoscale. Moreover, micro- and nanocracks in real electronic systems, MEMS or NEMS are nested in a variety of materials with different material properties. In such cases, the experimental approach on its own is not suited for the determination of critical stress/strain states or system reliability. A possible solution is the strategy of using a hybrid analysis tool combining SPM-based experimental displacement measurements and finite element concepts. In this work such an approach is implemented by a definition of an adaptation concept which is presented in Sect. 4.6.1. The basis for the concept is the mesh adaptor enabling the reduction of 3D-FE mesh data to 2D-DIC software node coordinate data (Sect. 4.6.2). Furthermore, a common platform for FEA and DIC results is defined (Sect. 4.6.3) and a verification algorithm for simulation/experimental results is developed (Sect. 4.6.4).

The developed strategy is applied to the measurements of Sect. 3.4.4 in combination with FE-results basing on the models described in Sect. 4.2.

4.6.1 Adapted Finite Element Concept

The objective of an adapted finite element concept is the creation of a tool which allows the verification of in-situ loading experiments and finite element results using a combination of finite element simulation and DIC-based displacement fields. FEA on its own is not sufficient to describe complex material and device behavior for future micro and nanomaterial testing. Unknown material constitutive laws and complex interrelation between testing equipment and specimen make it unreliable to evaluate reliability exclusively by FEA or analytical approaches. Consequently validation of mechanical test modeling by suitable experiments is inevitable.

Comparison between measured and simulated deformation fields is the way to achieve trustworthy testing results. Unfortunately, in many cases simple determination of material properties by DIC measurements is impossible since there is the general access restriction of DIC measurements to surface and in-plane deformation. 3D and internal deformation data is indispensable for many testing purposes, e.g. for the determination of parameters for advanced fracture mechanics criteria (J -, C^* -, T -integral, etc.). Moreover, in some cases stress/strain data on three dimensional objects is needed, which cannot be obtained from in-plane surface measurements. This information can be provided adapting FEA to DIC measurement. Due to the fact that both methods are implemented in completely different and therefore incompatible software packages an adaptation concept from FEA to DIC was developed. A flow chart of the concept is shown in Fig. 4.12.

Basically, the concept allows to match simulation and measurement results in order to provide material characterization on a best-fit strategy. At the end, material properties such as Young's modulus or fracture mechanical properties are determined combining FEA and DIC results. FE meshes from either PATRAN/ABAQUS or ANSYS are utilized for

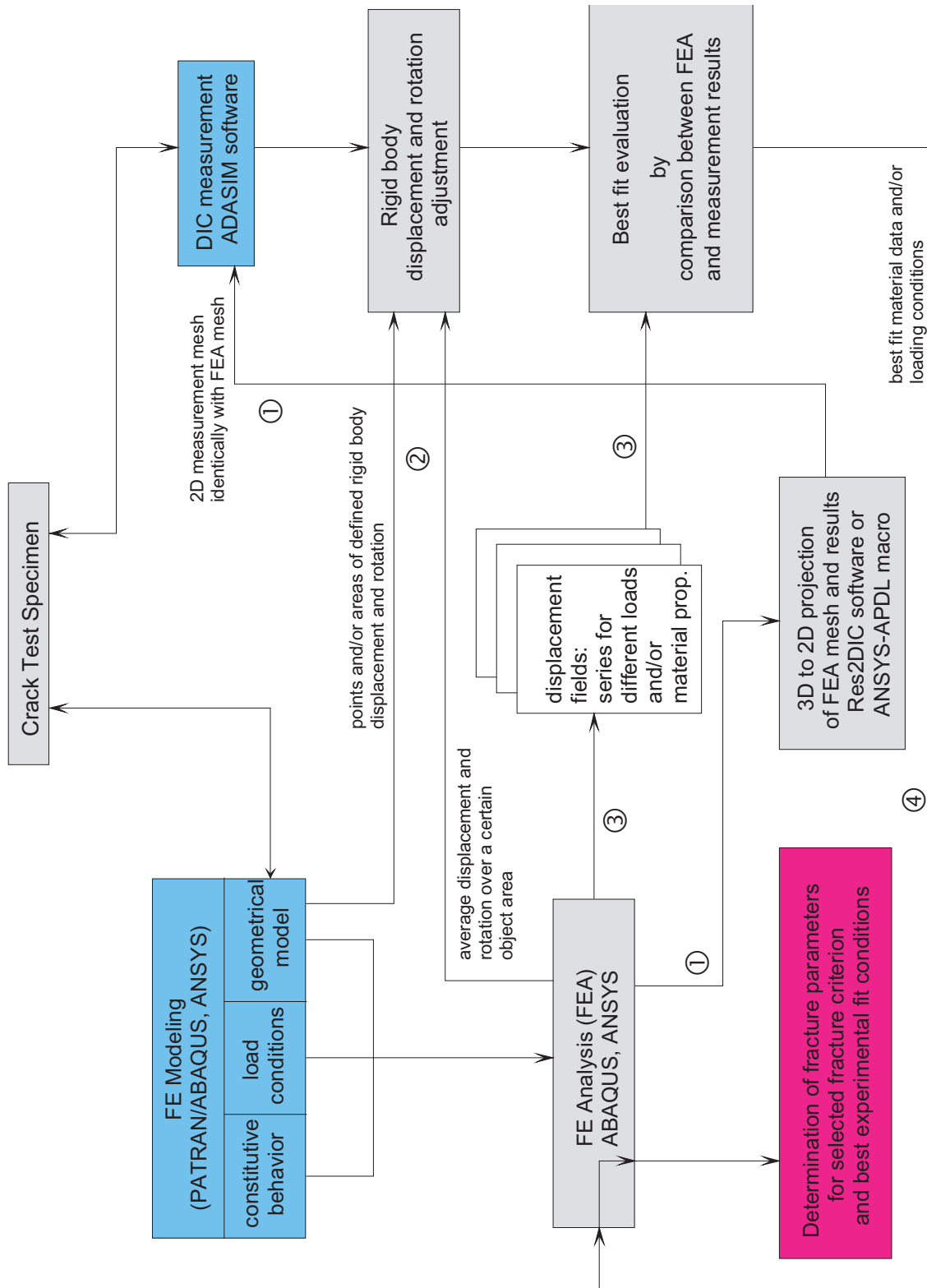


Figure 4.12. Adaptation concept.

simulation as well as for DIC displacement field determination from load state images (see ① in Fig. 4.12). Therefore, a transformation interface of FE mesh nodes to respective measurement mesh nodes have to be developed. 3D-to-2D mesh transformation, data (node) reduction and allocation of object and model coordinates are the major problems to be solved.

Although determined in the same mesh nodes, simulation and measurements results cannot be compared directly. DIC deformation fields are superposed by rigid body displacements and rotations originating from, e.g. , testing machine drifts, or FE boundary conditions which are not equivalent to the actual experimental loading. Therefore, original DIC results have to be derotated and a translation correction has to be applied before comparing them with FEA fields (see ② in Fig. 4.12). Within the concept, a set of finite element displacement fields is compared with a set of derotated and displaced measurement fields (③ in Fig. 4.12). Different simulated fields are provided varying specimen load conditions or material properties. The best fit between simulation and measurement field reveals the optimum input data (modeling) for simulation with regard to the specimen load conditions under consideration. Utilizing these best fit conditions proven by experiment, additional or more advanced material properties can be produced demanding more information than DIC measurements can provide (④ in Fig. 4.12).

4.6.2 Mesh Transfer from FEA to Experiment

Transfer of finite element nodes to the measured experimental area is a straightforward approach for data comparison. This technique allows to determine the experimental displacements at the position of the FE nodes so that a direct validation of the results can be performed. Figure 4.13 illustrates the concept of the mesh adaption from 3-dimensional FE model to 2-dimensional region-of-interest (ROI) of the experimental approach.

The digital image correlation technique determines displacements at specific grid nodes which are similar to the nodes of the finite element mesh. In addition to meshing by means of an internal mesh generator the DIC software allows to import user defined meshes. During this mesh-import procedure the user has to specify x, y -scaling factors for the transformation of [mm]-based node location (from FE-model data) to [pixel]-coordinates (of measurement images).

In the presented case, the mesh adaptation is carried out between the FE-code ANSYS and the DIC software ADASIM using ANSYS parametric design language (APDL). The application of APDL introduces a functionality allowing a fast postprocessing and streamlines the data extraction form the FE-model to the DIC software. The implemented interface macro is structured as follows:

1. defining of an region-of-interest (ROI) area by user defined (mouse) picking of 4 edge nodes,
2. definition of result coordinate system aligned with the coordinate system of the user-defined ROI area,

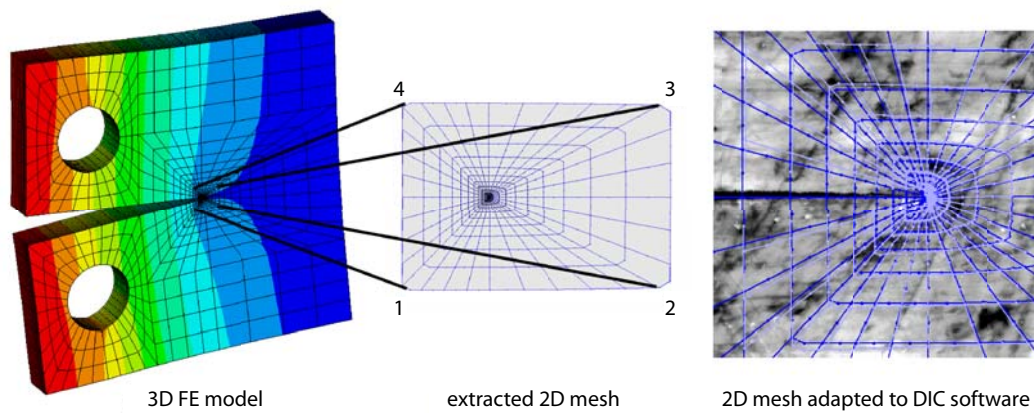


Figure 4.13. *Concept of mesh adaptation from FEA- to DIC-software.*

3. printout of the node coordinates and element definitions of the ROI area; the node indices have to be re-organized from ANSYS notation to the notation implemented in ADASIM; details on node notations can be found in the ANSYS and ADASIM user manuals [129, 130]
4. printout of the results (node displacements).

The interface macro produces mesh input files according to the interface definition of ADASIM. A detailed description of the APDL code is not necessary. The programming can be actualized relatively straightforward by implementation of the concept described above.

Figure 4.13 illustrates mesh adaptation for the rather simple case of the CT-specimen which is the test specimen within this work. Nevertheless, the basic idea of this mesh adaptation can also be applied to more complex structures of microelectronic components. In this case the region of interest can be e.g. mechanically weak parts of a micro- or nanostructured solder bump or ultrathin passive or active layers. In microelectronic applications, usually a large number of different materials is combined on a small volume. This results in a variety of material interfaces and failure often occurs at these interfaces where an experimental evaluation is difficult to obtain. Therefore, the DIC analysis software (ADASIM) provides the ability to define separate meshes for areas of different materials within an image. Furthermore, the correlation algorithms are modified in such a way that the kernel structure (compare to Fig. 2.3) of a surface of a specific material will not be searched in an adjacent mesh of another material. At the material interface the strategy of cutting the kernel in two pieces is implemented to avoid correlation error at material interfaces. However, it has to be mentioned that currently this strategy is not tested completely and a detailed analysis has to be carried out in the future.

Furthermore, it has to be mentioned that the described mesh transfer is also available from ABAQUS to ADASIM [131]. In addition, an in-house FE-code (ALICE) can also be used for finite element analysis and subsequent mesh data adaptation. A discussion of this so-called RES2DAC module would go beyond the scope of this thesis.

4.6.3 Results Platform

As a platform for finite element and DIC result data comparison Mathworks MATLAB software is used. MATLAB's *load* function enables the import of output files originating from DIC software, ADASIM and favored finite element codes (either ABAQUS or ANSYS). Import of finite element data means reading predefined file output formats already modified by the 3d FEA-DIC mesh adapter (compare to Sect. 4.6.2).

The link between displacement values from different sources is performed by node number allocation of the FE-mesh. Because ADASIM results are obtained for the same mesh node indices as in the FE simulation (if coordinate transformation is performed correctly) and all ADASIM nodes are included in the FE mesh, a direct comparison between simulation and experiment is possible. The import function can comprise not only data import but also different sort function e.g. the deletion of error type values from ADASIM. In the most practical cases the mesh will consist of areas with varying node densities so that weighting functions have to be applied to node results. However, in this work weighting functions are not included.

4.6.4 Verification Algorithm

The general aim is the verification of either FE-model or DIC-measurements. After data import an appropriate comparison algorithm between the FE- and DIC-results has to be applied. The accomplished verification process implemented as a MATLAB program comprises two main functions:

- variation of DIC-results for the compensation of rigid body rotation and displacement within the region of interest,
- assessment of the degree of similarity between the FE- and the DIC-results to figure out optimum matching conditions and the best-fitting of the FE-results to the measurements.

In special cases, information on appropriate rotation and displacement correction values can be extracted directly from the measured field i.e. if special symmetry conditions are given in the loaded structure. However, for future application of the adaptation concept, a more general approach has to be employed. Therefore, the variation of the DIC-results is done by addition of rotation and displacement terms to the measured field values depending on the location of the measurement point. The modification of the displacement field is done for different angles and displacement values so that a variety of displacement fields are generated.

In the second step, the modified displacement fields have to be evaluated according to their similarity to the FE-results. A problem arises from the fact that the deformation behavior of an FE model can be far from reality (measurement) due to wrong material data or material model assumptions. As a consequence, rotation and displacement matching and the comparison with FE-results is not a simple task. Derotation is performed although the simulation results may be inadequate with regard to the measurement. To overcome this problem, different statistical criteria are implemented in the MATLAB verification algorithm e.g. cross correlation coefficient, covariance and least square methods.

In the following the verification algorithm is applied to the crack tip field of the CT-specimen presented in Sect. 3.4.4. The COD-concept (compare to Sect. 4.1) led to the conclusion that a combination of DIC- and FE-results will provide additional information for the evaluation of a crack tip displacement field. The analysis of the required fitting procedures in this reveals the following algorithm sub-steps:

- Derotation and displacement matching
- Determination of material properties

In the following, the verification process is carried out to the example of the CT-specimen. It has to be noted that in-situ measurements on other structures (e.g. three point bending of a microelectronic component) may necessitate other approaches.

Derotation and Displacement Matching

The modification of the measured field was achieved by two steps. Firstly, the mean values of displacement in x - and y -direction u_x and u_y were evaluated and subtracted from the measured field values. In a second step, the measured displacement field was rotated stepwise within a predefined interval of angle increments so that a set of modified displacement fields was generated. The rotation center was chosen with regard to the rotation field data obtained by the correlation software.

Each of the modified displacement fields was compared to the FE-results by the three different statistical criteria described above. Figure 4.14 shows computed cross correlation coefficients, covariance and least square fitting parameters for the pair of FE and ADASIM fields in dependence on the rotation angle. Least square fitting as well as cross correlation result in graphs with well defined extremum values. Therefore, they can act as appropriate criteria for the determination of accurate derotation angles. Unfortunately, the covariance method is not suited for the determination of an appropriate derotation angle. A significant feature indicating an optimum derotation angle is not observed in the plot of the covariance (Fig. 4.14).

The cross correlation coefficient is the better criterion for optimum derotation evaluation, because it tolerates (to a certain extent) non-matching FE-results. Cross correlation method is therefore suited to match displacement field pattern rather than to find absolute values of similarity.

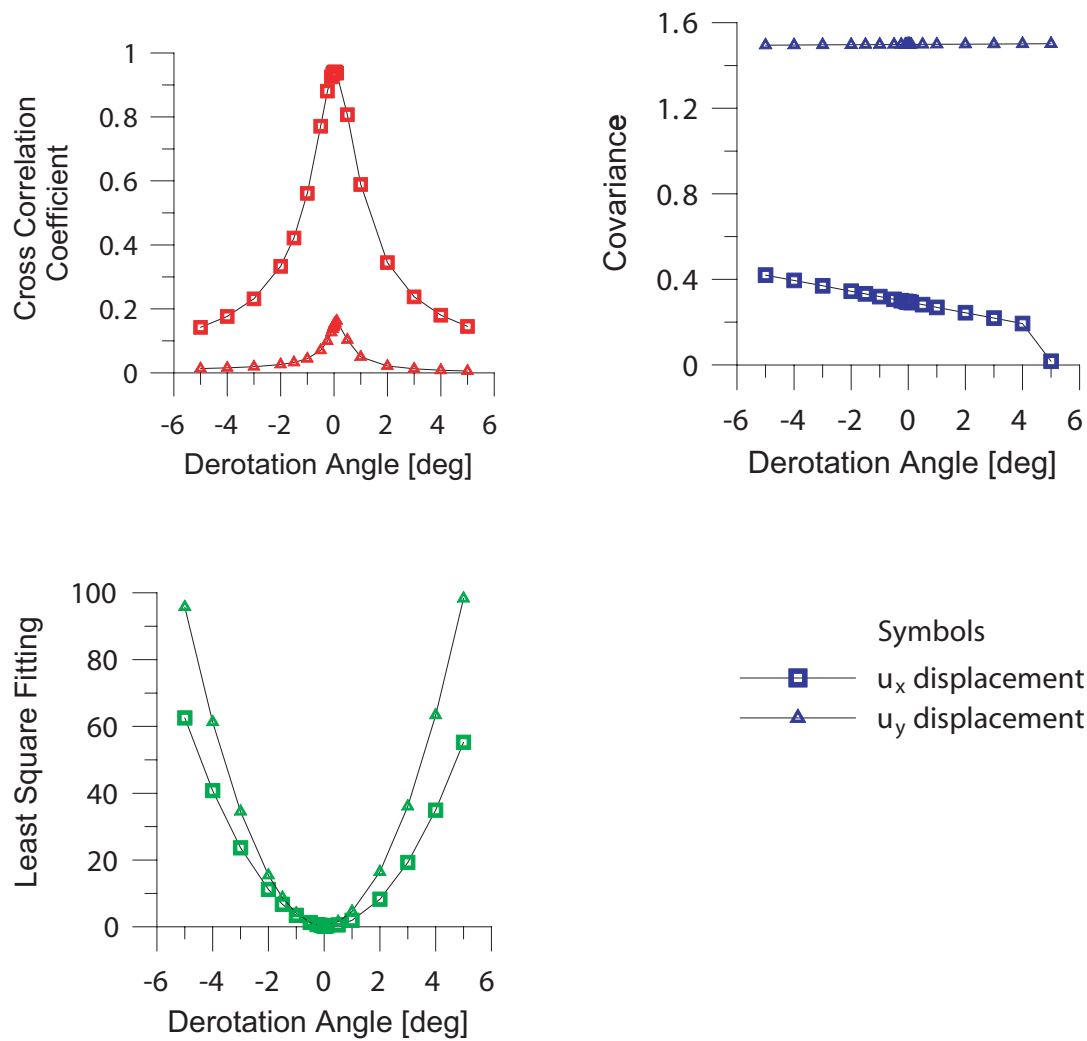


Figure 4.14. Different fitting criteria characterizing derotation of a pair of FE and ADASIM results, best fit is achieved at extremum position.

Figure 4.15 shows a zoomed-in graph of the cross correlation plot of Fig. 4.14. The exact determination of the optimum derotation angle is achieved by fitting a square polynomial to the discrete data points.

Optimum derotation is slightly different for x - and y -components of the in-plane displacement fields. In this case u_y -optimization is the better choice because the u_x -displacement exhibits higher measurement errors due to the low absolute displacement values in x -direction. The optimum value for cross correlation between the measured and the FE-based u_x -field is very low compared to that of the u_y -field (0.16 to 0.94).

Another fact that has to be taken into account is the interaction of a small amount of mode II crack tip loading caused by non-ideal loading pin parallelism. This problem can be solved by a re-design of the loading pin holders. However, within this work a new design of the loading device was not possible.

Moreover, the varying mesh density is not taken into account. Every measurement and FE-value is weighted equally. In the presented case of a material with a loaded crack tip behaving in an elastic manner this fact is not causing a significant error. However, if plastic deformation is present in the very vicinity of the crack tip large differences in the displacement value compared to the FE-model are expected. In such cases, a location or mesh density related weighting function should be introduced.

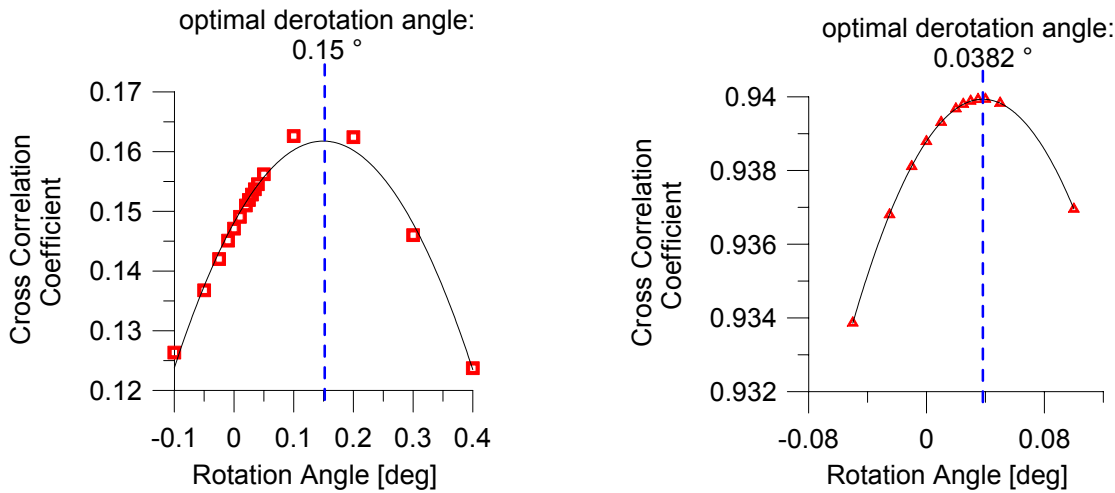


Figure 4.15. Determination of the ideal derotation angle by means of cross correlation of displacement fields; (**left**) for u_x displacement field; (**right**) u_y displacement field.

Figure 4.16 illustrates the effect of derotation on measured displacement fields. Original measurement (Fig. 4.16 (b)) results have to be rotated only slightly by an angle of 0.038 deg (Fig. 4.16 (d)) for best matching with simulation (Fig. 4.16 (a)). In this case the overall pattern of the u_y crack opening displacement field becomes very similar to that of the simulation. For comparison a derotation with a relatively large angle of 1 deg is shown in (Fig. 4.16 (c)).

However, absolute values of both fields are still quite different. The FE-results of the crack opening displacement fields are approximately 1.6 times higher than that of the measurement. This may be caused by inaccurate material properties of the FE-analysis e.g. a slightly inaccurate value of the Young's modulus. In the following the material model will be checked utilizing similar verification algorithms as introduced in this section.

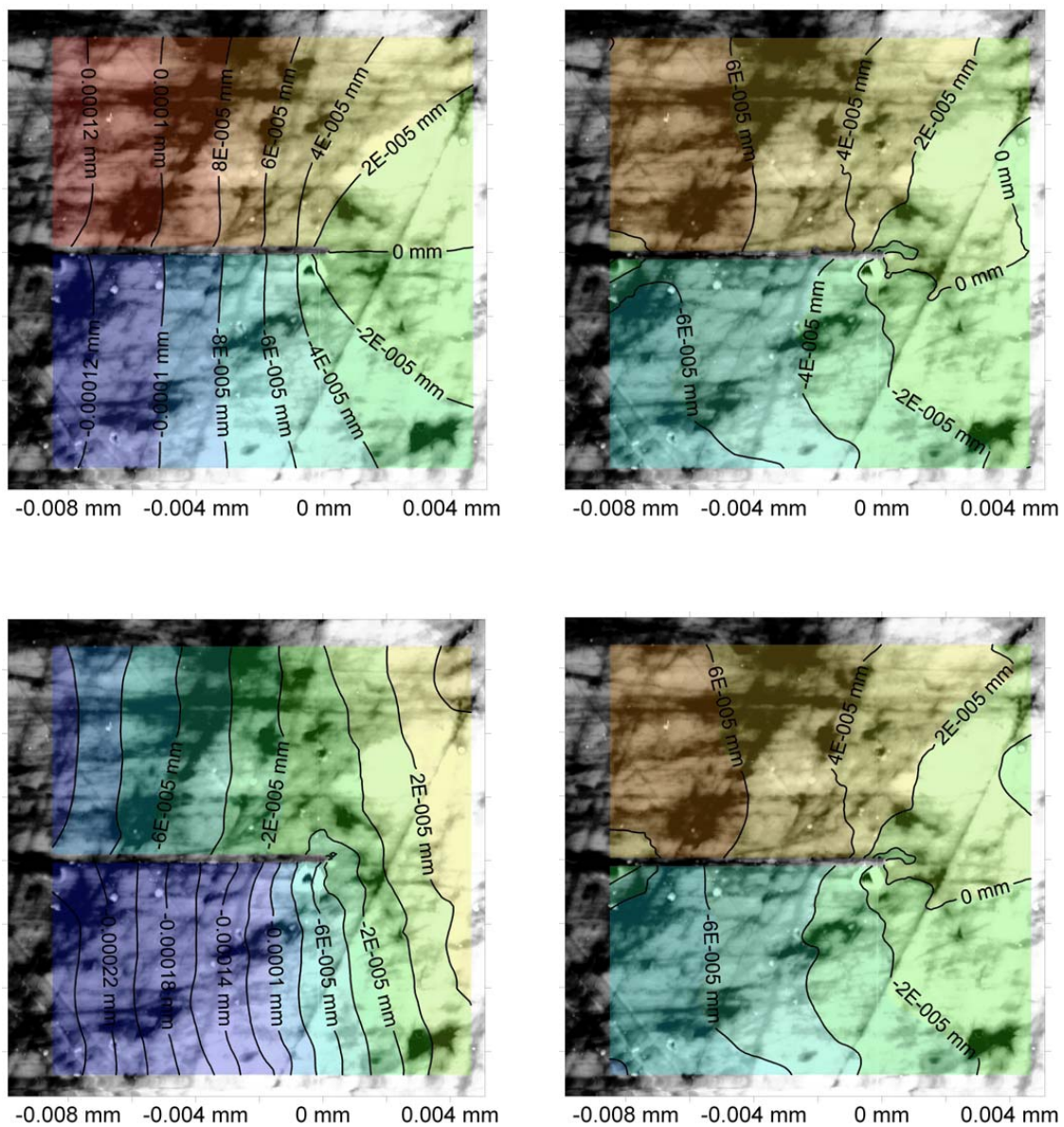


Figure 4.16. Displacement field derotation and rigid body displacement compensation, u_y -displacement field (a) FE-result computed with ANSYS, (b) measurement field by ADASIM, (c) derotation by 1 deg (much larger angle than needed), (d) derotation by 0.038 deg (best fitting between simulated and measured field).

Determination of Material Properties

For the determination of material properties the verification algorithm has to be applied to a pair of measured and simulated results. In this case the FE-results are varied and the measured (or modified) field remain the same. FE-simulations are performed with different Young's moduli within a reasonable scope of values i.e. 2600 - 5000 MPa. Each of the obtained FE-displacement fields is compared to the modified (derotated and rigid body displacement corrected) measured field by means of the least square method.

Figure 4.17 illustrates the least square parameter versus the Young's modulus of the FE simulation. A minimum value of the least square parameter at a Young's modulus of 3600 MPa is indicating the best matching pair of displacement fields.

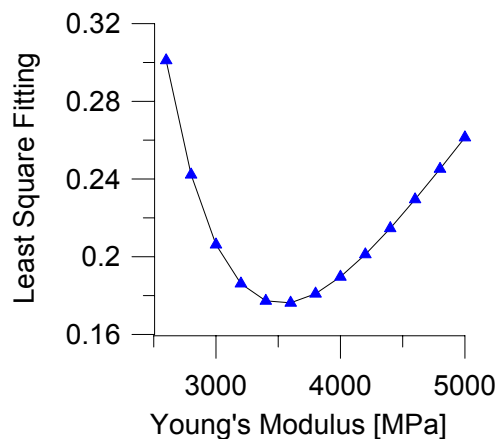


Figure 4.17. Determination of best fitting material model (Young's modulus) at the minimum of least square differences of displacements (here u_y -field), best fit between FE and DIC for $E = 3600$ MPa.

Figure 4.18 shows the modified measured displacement field (a) and FE-based fields (b-c) where the best matching field is illustrated in (c).

The results of the verification algorithm clearly proof the capability of the adaptation concept in combination with the verification algorithm. The applied verification strategy by comparison of measured and simulated displacement fields leads to a well defined best matching parameter set.

Unfortunately, the recursively derived Young's modulus of 3600 MPa is not equivalent to the measurements discussed in Sect. 3.2.5 where a value of 2800 MPa was determined. A reason for this can be that the relaxation test specimens for Young's modulus determination and the crack test CT-specimen are not manufactured from the same charge of material. Slightly different curing cycles can cause this deviation in material property. Moreover, unmodified cyanate ester resins tends to form a pre-stressed material configuration. This fact was indicated by the observation of cracks in the cured plates. Therefore, a homogeneous material behavior cannot be guaranteed within the complete volume of the cured plates and the specimens. Especially at the surface of the plates the curing parameters are

different from that of the middle resulting in varying material properties over the thickness of the plates.

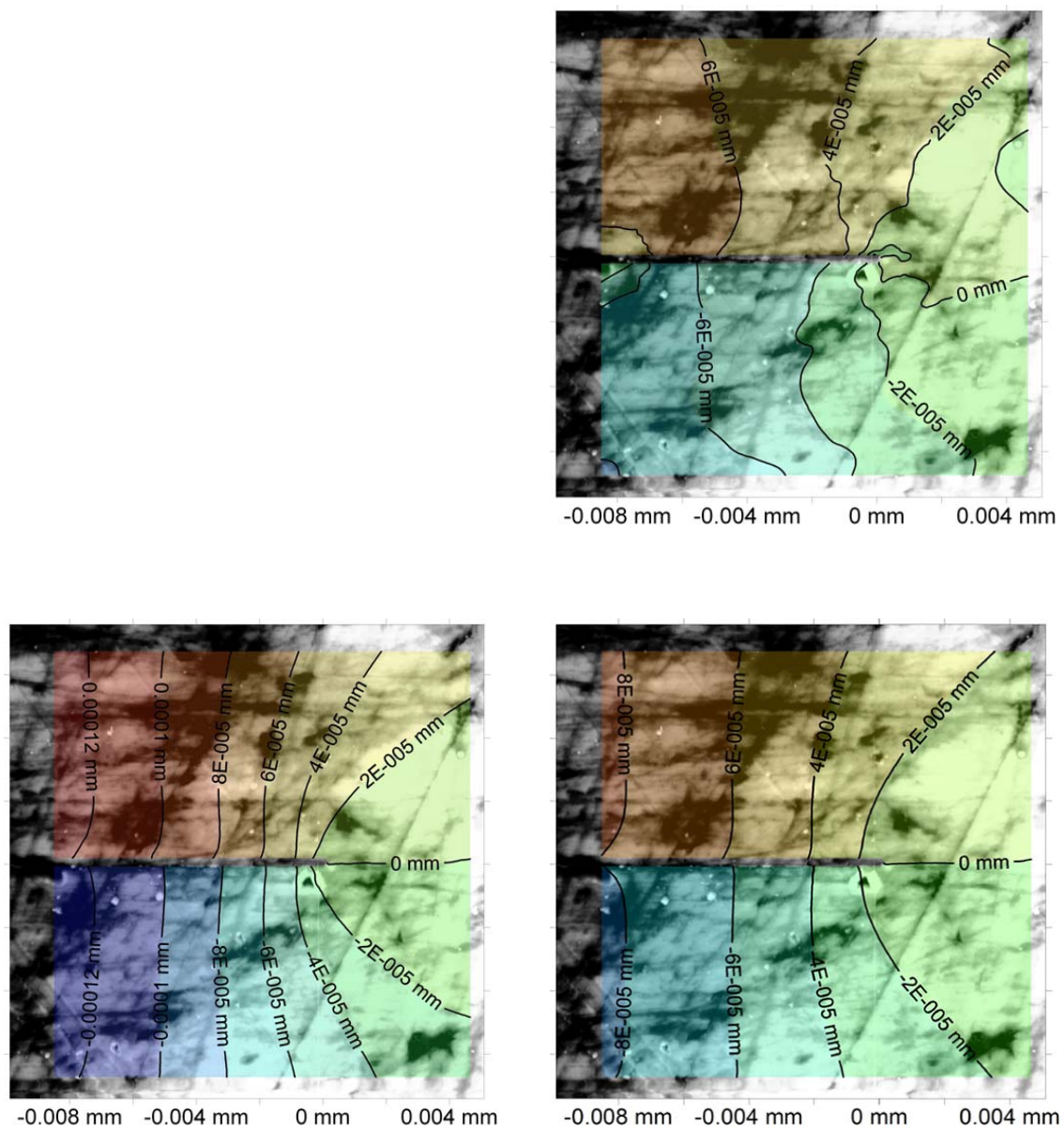


Figure 4.18. Validation of FE-modeling by comparison of displacement fields with DIC measurement, (a) ADASIM result for crack opening displacement field (derotated and rigid body displacement corrected field), (b) FE field for non fitting simulation with $E = 2800$ MPa, (c) FE field for best fit simulation with $E = 3600$ MPa.

4.6.5 Concluding Remarks on Adaptation Concept

The introduced adaptation strategy and measurement/simulation verification concept emphasize its capability for the evaluation of micro- and nanocracks. Reliability testing and in-situ loading of newly developed micro- and nanoelectronics components supported by DIC measurements and FEA will give new insights in the material behavior on the micro- and nanoscale. Especially the potential in the determination of unknown material properties qualifies the adaptation strategy as a powerful tool for future electronics and material design.

Chapter 5

Conclusions and Outlook

In this thesis the principle of DIC-based displacement measurements extracted from in-situ loading tests under the AFM is successfully applied to crack tip evaluation of a polymer material. The measurements were carried out in ambient air with a commercially available scanning probe microscope equipped with specially designed loading stages.

The presented tests and results lead to the following conclusions:

- In general, the application of digital image correlation to SPM-based images is established as a technique for the extraction of displacements on the micro- and nanoscale.
- AFM topography images of surfaces with a defined roughness in the nm-range are well suited for the application of digital image correlation techniques and are, therefore, the basis for in-situ displacement measurements.
- System drifts induced by thermal drifts or piezoceramic based scanner instabilities can be eliminated. The correction for system drifts is achieved by fitting of correction functions to mean displacements values.
- For scan sizes below $1\ \mu\text{m}$, the described SPM based displacement measurement technique is not qualified yet. Possible solutions for elimination of the arisen thermal instabilities are the development of systems which compensate thermal drifts. Another feasible approach would be a installation of thermal control units for the whole system or specific system components.
- Crack evaluation of micro- and nanocracks have to be supported by numerical simulations. The introduced adaptation strategy is a possible method for a hybrid-type evaluation of cracks and defects in electronic systems and MEMS/NEMS. A potential is also seen for the testing and qualification of nanomaterials.

Outlook

The presented results serve as a basis for displacement measurements down to the nanoscale. As scanning probe microscopy is a cutting edge technology the application in the fields of (nano)-electronics, MEMS/NEMS, BIO-MEMS, and material science will be inevitable for future research. In the following, the trends emerging from several research fields showing direct effect on the presented nanoDAC technique will be discussed briefly.

Nanomaterials

Design of nanomaterials is already a fundamental task for the development of tailored structural, active or passive components. Often the effects of incorporation of nanofillers, such as nanotubes or OLS on the macromechanical behavior are not understood. The presented nanoscale displacement measurement technique is a promising tool for qualitative and quantitative description of these size-effects. However, further improvements of the accuracy of the nanoDAC method is required to target the observation of objects in the 10 nm range.

Interface problems

The growing number of passive and active ultrathin layers in microelectronic systems is becoming a problem for experimental and FE-based reliability determination. A possible solution from the experimental point of view is newly developed DIC algorithms taken into account the spatial variation of materials. By application of material based correlation zones the accuracy of method will be enhanced at the material interfaces. In combination with SPM or FIB/SEM experimental techniques an improvement of the nanoDAC method can be expected.

SPM developments

Arisen problems of stability will be overcome by the application of the actual SPM developments. Higher scanning frequencies are a key for the experimental analysis of plastic or visco-plastic material classes and will reduce the errors introduced by thermal drifts. The problem of scanner creep and scanner nonlinearities caused by piezoceramic scanning devices will be overcome by improved closed-loop scanning techniques. The application of capacitive components for scanning units has also a high potential for the accuracy enhancement of nanoscale displacement measurements.

Major improvements of the presented nanoDAC method are expected from the following ongoing developments of experimental techniques:

- application of fast scanning techniques in SPM equipment will reduce thermal drifts;
- combined SEM/SPM equipment improves the handling of the measurements;
- combined FIB/SEM tools will improve the specimen fabrication and will broaden the extracted information from the observed specimens;

- AFM topography image based 3D-DIC for 3D displacement fields is the key for a one-to-one comparison of finite element results and experimental approaches. With 3-D displacement fields the correction for specimen tilt is becoming a solvable task.

Simulation

For future developments of microelectronic systems, MEMS and NEMS the importance of the combination of simulation and experiments will increase. The discussed adaptation strategies will be improved by implementation of:

- weighting functions, to take into account the density of FE-meshes;
- automated recursive finite element parameter studies with stochastic parameter variation;
- advanced concepts of automated derotation.

Parallel to these strategies emerging from classical mechanics approaches quantum mechanics will play an important role in the nanometer range. Nowadays, the existing quantum mechanics simulation tools are beginning to expand their capabilities from molecular modeling towards meso-type material descriptions. The implementation of homogenization techniques is believed to close the technological gap between the *micro-* and *nanoworld*. The term homogenization is understood as the numerical determination of a model describing a representative volume of bulk material. Thereby, the spacial distribution of filler particles or different material phases are taken into account. The results of the homogenization will be employed as input data for standard finite element codes.

Bibliography

- [1] R. Bashir. Biological Mediated Assembly of Artificial Nanostructures and Microstructures. In W.A. Goddard, D.W. Brenner, S.E. Lyschevski, and G.J. Iafarte, editors, *Handbook of Nanoscience, Engineering, and Technology*. CRC Press, Boca Raton, 2003.
- [2] D. Vogel, A. Schubert, W. Faust, R. Dudek, and B. Michel. MicroDAC - a Novel Approach to Measure In Situ Deformation Fields of Microscopic Scale. *Microelectronics Reliability*, 36(11-12):1939–1942, 1996.
- [3] M. Bauer and J. Bauer. Aspects of the Kinetics, Modelling and Simulation of Network Build-Up During Cyanate Ester Cure. In I. Hamerton, editor, *Chemistry and Technology of Cyanate Ester Resins*, pages 58–86. Chapman & Hall, 1994.
- [4] G.-M. Kim and G.H. Michler. Micromechanical Deformation Processes in Toughened and Particle-Filled Semicrystalline Polymers: Part 1. Characterization of Deformation Processes in Dependence on Phase Morphology. *Polymer*, 39(23):5689–5697, 1998.
- [5] J.U. Starke, G.H. Michler, W. Grellmann, S. Seidler, M. Gahleitner, J. Fiebig, and E. Nezbedova. Fracture Toughness of Polypropylene Copolymers: Influence of Interparticle Distance and Temperature. *Polymer*, 39(1):75–82, 1998.
- [6] D. Baither, F. Ernst, T. Wagner, M. Rühle, M. Bartsch, and U. Messerschmidt. Micromechanisms of Fracture in NiAl Studied by In Situ Straining Experiments in an HVEM. *Intermetallics*, 7:479–489, 1999.
- [7] J. Guan, C. Wang, and W. Chu. Atomic Structure of Loaded Crack Tip by AFM. *Scripta Materialia*, 39(9):1211–1214, 1998.
- [8] Y.H. Lu, Y.G. Zhang, L.J. Qiao, Y.-B. Wang, C.Q. Chen, and W.Y. Chu. In-Situ TEM Study of Fracture Mechanisms of Polysynthetically Twinned (PST) Crystals of TiAl Alloys. *Material Science and Engineering A*, 289(1-2):91–98, 2000.
- [9] J.X. Li, W.Y. Chu, Y.B. Wang, and L. J. Qiao. In Situ TEM Study of Stress Corrosion Cracking of Austenitic Stainless Steel. *Corrosion Science*, 45(7):1355–1365, 2003.
- [10] L. Cretegy and A. Saxena. AFM Characterization of the Evolution of Surface Deformation During Fatigue in Polycrystalline Copper. *Acta Materialia*, 49:3755–3765, 2001.

- [11] L. Creteigny and A. Saxena. Evolution of Surface Deformation During Fatigue of PH 13-8 Mo Stainless Steel Using Atomic Force Microscopy. *Fatigue & Fracture of Engineering Materials & Structures*, 25(3):305–314, 2002.
- [12] M.S. Bobji and B. Bushan. Atomic Force Microscopic Study of the Micro-Cracking of Magnetic Thin Films under Tension. *Scripta Materialia*, 44(1):37–42, 2001.
- [13] M.S. Bobji and B. Bushan. In Situ Microscopic Surface Characterization Studies of Polymeric Thin Films During Tensile Deformation Using Atomic Force Microscopy. *Journal of Materials Research*, 16(3):844–855, 2001.
- [14] T. Kinoshita. Stress Singularity Near the Crack-Tip in Silicon Carbide: Investigation by Atomic Force Microscopy. *Acta Materialia*, 46(11):3963–3974, 1998.
- [15] K. Komai, K. Minoshima, and S. Inoue. Fracture and Fatigue Behavior of Single Crystal Silicon Microelements and Nanoscopic AFM Damage Evaluation. *Microsystem Technologies*, 5(1):30–37, 1998.
- [16] C. Marieta, M. del Rio, I. Harismendy, and I. Mondragon. Effect of the Cure Temperature on the Morphology of a Cyanate Ester Resin Modified with a Thermoplastic: Characterization by Atomic Force Microscopy. *European Polymer Journal*, 36(7):1445–1454, 2000.
- [17] C. Marieta, P.M. Remiro, G. Garmendia, I. Harismendy, and I. Mondragon. AFM Approach Toward Understanding Morphologies in Toughened Thermosetting Matrices. *European Polymer Journal*, 39(10):1965–1973, 2003.
- [18] F. Creuzet and E. Guilloteau. An AFM Study of Key Phenomena Involved in the Fracture of Glass. *Verre*, 1(6):11–13, 1995.
- [19] M. Göken, H. Vehoff, and P. Neumann. Atomic Force Microscopy Investigations of Loaded Crack Tips in NiAl. *Journal of Vacuum Science and Technology B*, 14(2):1157–1161, 1996.
- [20] F. Thome, M. Göken, and H. Vehoff. Study of the Fracture Behavior in Soft and Hard Oriented NiAl Single Crystals by AFM. *Intermetallics*, 7(3-4):491–499, 1999.
- [21] M. Göken, M. Maßmann, F. Thome, and H. Vehoff. Microscopic Fracture Behavior of Single Crystalline Intermetallics. In *Structural Intermetallics 1997. Proceedings of the Second International Symposium on Structural Intermetallics*, pages 641–648, 1996.
- [22] H. Vehoff, P. Ochmann, M. Göken, and M. Große Gehling. Deformation Processes at Crack Tips in NiAl Single- and Bicrystals. *Material Science and Engineering A*, 239-240(1-2):378–385, 1997.
- [23] M. Göken, F. Thome, and H. Vehoff. Study of Crack Tip Deformation in FeAl and NiAl Crystals with Optical Interference Microscopy and Atomic Force Microscopy. *Philosophical Magazine A*, 82(17-18):3241–3250, 2002.

- [24] U. Rabe, K. Janser, and W. Arnold. Vibrations of Free and Surface-Coupled Atomic Force Microscope Cantilevers: Theory and Experiment. *Review of Scientific Instruments*, 67(9):3281–3293, 1996.
- [25] E. Chilla, T. Hesjedal, and H.J. Fröhlich. Scanning Acoustic Force Microscope Detection of SAWs. In *IEEE Ultrasonics Symposium. Proceedings*, pages 363–366, 1994.
- [26] U. Rabe, S. Amelio, E. Kester, V. Scherer, S. Hirsokorn, and W. Arnold. Quantitative Determination of Contact Stiffness Using Atomic Force Acoustic Microscopy. *Ultrasonics*, 38(1-8):430–437, 2000.
- [27] O.V. Kolosov, M.R. Castell, C.D. Marsh, G.A.D Briggs, T.I. Kamins, and R.S. Williams. Imaging the Elastic Nanostructure of Ge Island by Ultrasonic Force Microscopy. *Physical Review Letters*, 81(5):1046–1049, 1998.
- [28] K. Yamanaka. UFM Observation of Lattice Defects in Highly Oriented Pyrolytic Graphite. *Thin Solid Films*, 273(1-2):116–121, 1996.
- [29] C.J. Druffner and S. Sathish. Improving Atomic Force Microscopy with the Adaptation of Ultrasonic Force Microscopy. In *Proc. SPIE Vol. 4703, Nondestructive Evaluation and Reliability of Micro- and Nanomaterial Systems*, pages 105–113, 2002.
- [30] K. Porfyarakis, H.E. Assender, and I.M. Robinson. The Interrelationship Between Processing Conditions, Microstructure and Mechanical Properties for Injection Moulded Rubber-Toughened Poly(methyl methacrylate) (RTPMMA) Samples. *Polymer*, 43(17):4769–4781, 2002.
- [31] A. Kuske and G. Robertson. *Photoelastic Stress Analysis*. Wiley, London, 1974.
- [32] E. O’Brien. A Review of Current Research in Photoelasticity. In *Photo-Mécanique 98*, pages 49–55, 1998.
- [33] T.Y. Chen. Digital Photoelasticity. In P.K. Rastogi, editor, *Photomechanics*, pages 197–232. Springer, 2000.
- [34] D. Coker, A.J. Rosakis, and A. Needleman. Dynamic Crack Growth Along a Polymer Composite-Homalite Interface. *Journal of the Mechanics and Physics of Solids*, 51(3):425–460, 2003.
- [35] A. Asundi, H. Xie, J. Yu, and Z. Zhong. Phase-Shifting AFM Moiré Method. In *Proc. SPIE Vol. 4448, Optical Diagnostics for Fluids, Solids, and Combustion*, pages 102–110, 2001.
- [36] P.F. Luo, Y.J. Chao, M.A. Sutton, and W.H. Peters. Accurate Measurement of Three-Dimensional Deformations in Deformable and Rigid Bodies Using Computer Vision. *Experimental Mechanics*, 33(2):123–132, 1993.
- [37] A. Tatschl and O. Kolednik. A New Tool for the Experimental Characterization of Micro-Plasticity. *Materials Science and Engineering A*, 339(1-2):265–280, 2002.

- [38] M.A. Sutton, W.J. Wolters, W.H. Peters, W.F. Ranson, and S.R. McNeill. Determination of Displacements Using an Improved Digital Image Correlation Method. *Image Vision Computing*, 1(3):133–139, 1983.
- [39] F.-P. Chiang. Moiré and Speckle Methods Applied to Elastic-Plastic Fracture Mechanics. In J.S. Epstein, editor, *Experimental Techniques in Fracture*, pages 291–325. VCH Publishers, 1993.
- [40] K. Matsumoto and M. Takashima. Improvements on Moiré Technique for In-Plane Deformation Measurements. *Applied Optics*, 12(4):858–864, 1973.
- [41] D. Post, B. Han, and P. Ifju, editors. *High Sensitivity Moiré*. Springer, New York, 1994.
- [42] B. Michel and R. Kuehnert. Mikro-Moiré-Methode und MikroDAC-Verfahren anwenden. *Materialprüfung*, 38(7/8):311–315, 1996.
- [43] D.T. Read and J.W. Dally. Theory of Electron Beam Moiré. *Journal of Research of the National Institute of Standards and Technology*, 101(1):47–61, 1996.
- [44] H. Xie, A. Asundi, C.G. Boay, L. Yungguang, J. Yu, Z. Zhaowei, and B. K.A Ngoi. High Resolution AFM Scanning Moiré Method and its Application to the Micro-Deformation in the BGA Electronic Package. *Microelectronics Reliability*, 42:1219–1227, 2002.
- [45] A. Asundi, X. Huimin, L. Chongxiang, C.G. Boay, and O.K. Eng. Micro-Moiré Methods - Optical and Scanning Techniques. In *Proc. of SPIE Vol. 4416, Optical Engineering for Sensing and Nanotechnology (ICOSN 2001)*, pages 54–57, 2001.
- [46] Y. Xing, F. Dai, and W. Yang. Experimental Study About Nano-Deformation Field Near Quasi-Cleavage Crack Tip. *Science in China, Series A (Mathematics, Physics, Astronomy)*, 43(9):963–968, 2000.
- [47] H. Xie, B. Li, R. Geer, B. Xu, and J. Castracane. Focused Ion Beam Moiré Method. *Optics and Lasers in Engineering*, 40:163–177, 2003.
- [48] F.-P. Chiang. A Family of 2D and 3D Experimental Stress Analysis Technique Using Laser Speckle. *Solid Mechanics Archives*, 3(1):1–32, 1978.
- [49] R.S. Sirohi and F.S. Chau, editors. *Optical Methods of Measurement - Wholefield Techniques*. Marcel Dekker, New York, 1999.
- [50] W.H. Peters and W.F. Ranson. Digital Imaging Techniques in Experimental Stress Analysis. *Optical Engineering*, 21(3):427–431, 1982.
- [51] M.A. Sutton, M. Cheng, W.H. Peters, Y.J. Chao, and S.R. McNeill. Application of an Optimized Digital Image Correlation Method to Planar Deformation Analysis. *Image and Vision Computing*, 4(3):143–150, 1986.

- [52] H.A. Bruck, S.R. McNeill, M.A. Sutton, and Peters W.H. Digital Image Correlation Using Newton-Raphson Method of Partial Differential Correlation. *Experimental Mechanics*, 29(3):261–267, 1989.
- [53] M.A. Sutton, S.R. McNeill, J.D. Helm, and M.L. Boone. Measurement of Crack Tip Opening Displacement and Full-Field Deformations During Fracture of Aerospace Materials Using 2d and 3d Image Correlation Methods. In A. Lagarde, editor, *IUTAM Symposium on Advanced Optical Methods and Applications in Solid Mechanics*, pages 571–580, 2000.
- [54] T.C. Chu, W.F. Ranson, M.A. Sutton, and W.H. Peters. Application of Digital-Image-Correlation Techniques to Experimental Mechanics. *Experimental Mechanics*, 25(3):232–244, 1985.
- [55] Y.-J. Chao and M.A. Sutton. Accurate Measurement of Two- and Three-Dimensional Surface Deformations for Fracture Specimens by Computer Vision. In J.S. Epstein, editor, *Experimental Techniques in Fracture*, pages 59–93. VCH Publishers, 1993.
- [56] J. Liu, J. Lyons, M. Sutton, and A. Reynolds. Experimental Characterization of Crack Tip Deformation Fields in Alloy 718 at High Temperatures. *Journal of Engineering Materials and Technology*, 120(1):71–78, 1998.
- [57] J. González and W.G. Knauss. Strain Inhomogeneity and Discontinuous Crack Growth in a Particulate Composite. *Journal of the Mechanics and Physics of Solids*, 46(10):1981–1995, 1998.
- [58] W.D. Lockwood and A.P. Reynolds. Use and Verification of Digital Image Correlation for Automated 3-D Surface Characterization in the Scanning Electron Microscope. *Materials Characterization*, 42(2-3):123–134, 1999.
- [59] M.G.D. Geers, R. de Borst, and T. Peijs. Mixed Numerical-Experimental Identification of Non-Local Characteristics of Random-Fibre-Reinforced Composites. *Composites Science and Technology*, 59(10):1569–1578, 1999.
- [60] J. Lambros, A. Narayanaswamy, M.H. Santare, and G.J. Anlas. Manufacture and Testing of a Functionally Graded Material. *Journal of Engineering Materials and Technology*, 121(4):488–493, 1999.
- [61] A.-F. Bastawros and A.G. Evans. Deformation Heterogeneity in Cellular Al Alloys. *Advanced Engineering Materials*, 2(4):210–214, 2000.
- [62] A.-F. Bastawros, H. Bart-Smith, and A.G. Evans. Experimental Analysis of Deformation Mechanisms in a Closed-Cell Aluminum Alloy Foam. *Journal of the Mechanics and Physics of Solids*, 48(2):301–322, 2000.
- [63] H.W. Schreier, J.R. Braasch, and M.A. Sutton. Systematic Errors in Digital Image Correlation Caused by Intensity Interpolation. *Optical Engineering*, 39(11):2915–2921, 2000.

- [64] I. Chasiotis and W.G. Knauss. A New Microtensile Tester for the Study of MEMS Materials with the Aid of Atomic Force Microscopy. *Experimental Mechanics*, 42(1):51–57, 2002.
- [65] J. Abanto-Bueno and J. Lambros. Investigation of Crack Growth in Functionally Graded Materials Using Digital Image Correlation. *Engineering Fracture Mechanics*, 69(14-16):1695–1711, 2002.
- [66] D.L. Davidson. Micromechanics Measurement Techniques for Fracture. In J.S. Epstein, editor, *Experimental Techniques in Fracture*, pages 41–57. VCH Publishers, 1993.
- [67] D. Vogel, J. Auersperg, A. Schubert, B. Michel, and H. Reichl. Deformation Analysis on Flip Chip Solder Interconnects by MicroDAC. In *Design and Reliability of Solders and Solder Interconnections. Proceedings of a Symposium held during the TMS Annual Meeting*, pages 429–438, 1997.
- [68] D. Vogel, J. Simon, A. Schubert, and B. Michel. High Resolution Deformation Measurement on CSP and Flip Chip. In *Fourth VLSI Packaging Workshop of Japan. Technical Digest*, pages 84 – 86, Kyoto, 1998.
- [69] E. Soppa, P. Doumalin, P. Binkele, T. Wiesendanger, B. Bornert, and S. Schmauder. Experimental and Numerical Characterisation on In-Plane Deformation in Two-Phase Materials. *Computational Materials Science*, 21(3):261–275, 2001.
- [70] G. Vendroux, N. Schmidt, and W.G. Knauss. Submicron Deformation Field Measurements. 3. Demonstration of Deformation Determinations. *Experimental Mechanics*, 38(3):154–160, 1998.
- [71] Y. Huang. *Scanning Tunneling Microscopy and Digital Image Correlation in Nanomechanics Investigations*. Ph.D. thesis, California Institute of Technology, Pasadena, 2001.
- [72] W.G. Knauss, I. Chasiotis, and Y. Huang. Mechanical Measurements at the Micron and Nanometer Scales. *Mechanics of Materials*, 35(3-6):217–231, 2003.
- [73] D. Vogel and B. Michel. Microcrack Evaluation for Electronics Components by AFM nanoDAC Deformation Measurement. In *Proceedings of the 2001 1st IEEE Conference on Nanotechnology. IEEE-NANO 2001*, pages 309–312, 2001.
- [74] D. Vogel, J. Keller, A. Gollhardt, and B. Michel. Evaluating Microdefect Structures by AFM based Deformation Measurement. In *Proc. of SPIE Vol. 5045, Testing Reliability, and Application of Micro- and Nano-Materials Systems*, pages 1–12, 2003.
- [75] J. Keller, D. Vogel, A. Schubert, and B. Michel. Displacement and Strain Field Measurements from SPM Images. In B. Bhushan, H. Fuchs, and S. Hosaka, editors, *Applied Scanning Probe Methods*, pages 253–276. Springer, 2004.

- [76] J. Keller, A. Gollhardt, D. Vogel, and B. Michel. Characterization of Microcracks by Application of Digital Image Correlation to SPM Images. In *Proceedings of SPIE 11th Annual International Symposium on Smart Structures and Materials, 14-18 March, 2004*, page to be published, 2004.
- [77] G. Vendroux and W.G. Knauss. Submicron Deformation Field Measurements. 2. Improved Digital Image Correlation. *Experimental Mechanics*, 38(2):86–92, 1998.
- [78] M.A. Sutton, S.R. McNeill, J. Jang, and M. Babai. Effects of Subpixel Image Restoration on Digital Correlation Error Estimates. *Optical Engineering*, 27(10):870–877, 1988.
- [79] G. Vendroux and W.G. Knauss. Submicron Deformation Field Measurements. 1. Developing a Digital Scanning Tunneling Microscope. *Experimental Mechanics*, 38(1):18–23, 1998.
- [80] D. Vogel, J. Auersperg, and B. Michel. Characterization of Electronic Packaging Materials and Components by Image Correlation Methods. In *Proc. of SPIE, Advanced Photonic Sensors and Applications II, Nov. 27-30 2001, Singapore*, volume 4596, pages 237–247, 2001.
- [81] M. Dost, E. Kieselstein, and R. Erb. Displacement Analysis by Means of Grey Scale Correlation at Digitized Images and Image Sequence Evaluation for Micro- and Nanoscale Applications. *Micromaterials and Nanomaterials*, 1(1):30–35, 2002.
- [82] T.L. Anderson. *Fracture Mechanics: Fundamentals and Applications*. CRC Press, 2nd edition, 1995.
- [83] D. Gross. *Bruchmechanik*. Springer, 1996.
- [84] American Society for Testing and Materials. *ASTM D5045, Standard Test Methods for Plane-Strain Fracture Toughness and Strain Energy Release Rate of Plastic Materials*, 1999.
- [85] G.R. Irwin. Onset of Fast Crack Propagation in High Strength Steel and Aluminum Alloys. In *Sagamore Research Conference Proceedings*, volume 2, pages 289–305, 1956.
- [86] J.R. Rice. A Path Independent Integral and the Approximate Analysis of Strain Concentration by Notches and Cracks. *Journal of Applied Mechanics*, 35:379–386, 1968.
- [87] D.M. Parks. A Stiffness Derivative Finite Element Technique for Determination of Crack Tip Stress Intensity Factors. *International Journal of Fracture*, 10(4):487–502, 1974.
- [88] T.K. Hellen. On the Method of Virtual Crack Extensions. *International Journal for Numerical Methods in Engineering*, 9(1):187–207, 1975.

- [89] H.G. deLorenzi. On the Energy Release Rate and the J-Integral of 3-D Crack Configurations. *International Journal of Fracture*, 19(3):183–193, 1982.
- [90] H.G. deLorenzi. Energy Release Rate Calculations by Finite Element Method. *Engineering Fracture Mechanics*, 21(1):129–143, 1985.
- [91] H.B. Ghavifekr. *Einsatz bruchmechanischer Integralkonzepte zur thermomechanischen Zuverlässigkeitsbewertung in der mikroelektronischen Aufbau- und Verbindungstechnik*. Ph.D. Thesis, Technische Universität Berlin, Berlin, 2003.
- [92] N.L. Goldman and J.W. Hutchinson. Fully Plastic Crack Problems: The Center-Cracked Strip under Plane Strain. *International Journal of Solids and Structures*, 11(5):575–591, 1975.
- [93] J.D. Landes and J.A. Begley. A Fracture Mechanics Approach to Creep Crack Growth. In *ASTM STP, 590*, pages 128–148. American Society for Testing and Materials, 1976.
- [94] K. Kishimoto, S. Aoki, and M. Sakata. On the Path Independent Integral - \hat{J} . *Engineering Fracture Mechanics*, 13(4):841–850, 1980.
- [95] S.N. Atluri. Path-Independent Integrals in Finite Elasticity and Inelasticity, with Body Forces, Inertia, and Arbitrary Crack-Face Conditions. *Engineering Fracture Mechanics*, 16(3):341–364, 1982.
- [96] S.N. Atluri, T. Nishioka, and M. Nakagaki. Incremental Path-Independent Integrals in Inelastic and Dynamic Fracture Mechanics. *Engineering Fracture Mechanics*, 20(2):209–244, 1984.
- [97] G. Menges, E. Haberstroh, W. Michaeli, and E. Schmachtenberg. *Werkstoffkunde Kunststoffe*. Hanser, 5. edition, 2002.
- [98] A.J. Kinloch and R.J. Young. *Fracture Behaviour of Polymers*. Elsevier Applied Science Publishers, London, 1983.
- [99] G.H. Michler. *Kunststoff-Mikromechanik: Deformations- und Bruchmechanismen*. Hanser, München, 1992.
- [100] I. Hamerton. Introduction to Cyanate Ester Resins. In I. Hamerton, editor, *Chemistry and Technology of Cyanate Ester Resins*, pages 1–6. Chapman & Hall, 1994.
- [101] C.P.R. Nair, D. Mathew, and K.N. Ninan. Cyanate Ester Resins, Recent Developments. *Advances in Polymer Science*, 155:1–99, 2001.
- [102] A.W. Snow. The Synthesis, Manufacture and Characterization of Cyanate Ester Monomers. In I. Hamerton, editor, *Chemistry and Technology of Cyanate Ester Resins*, pages 7–57. Chapman & Hall, 1994.

- [103] S.L. Simon and J.K. Gillham. Cure Kinetics of a Thermosetting Liquid Dicyanate Ester Monomer/High- T_g Polycyanurate Material. *Journal of Applied Polymer Science*, 47(3):461–485, 1993.
- [104] J. Bauer and M. Bauer. Cyanate Ester Based Resin Systems for Snap-Cure Applications. *Microsystem Technologies*, 8:58–62, 2002.
- [105] D.A. Shimp and B. Chin. Electrical Properties of Cyanate Ester Resins and their Significance for Applications. In I. Hamerton, editor, *Chemistry and Technology of Cyanate Ester Resins*, pages 230–281. Chapman & Hall, 1994.
- [106] T. Fang and D.A. Shimp. Polycyanate Esters: Science and Applications. *Progress in Polymer Science*, 20(1):61–118, 1995.
- [107] D.A. Shimp. Applications of Cyanate Ester (CE) Resins. *Polymeric Material Science and Engineering*, 71:561–562, 1994.
- [108] A.J. Kinloch and A.C. Taylor. The toughening of cyanate-ester polymers. *Journal of Materials Science*, 38:65–79, 2003.
- [109] S. Ganguli, D. Dean, K. Jordan, G. Price, and R. Vaia. Mechanical Properties of Intercalated Cyanate Ester-Layered Silicate Nanocomposites. *Polymer*, 44:1315–1319, 2003.
- [110] Y.M. Haddad. *Viscoelasticity of Engineering Materials*. Chapman & Hall, London, 1995.
- [111] J.D. Ferry. *Viscoelastic Properties of Polymers*. Wiley, New York, 3rd edition, 1980.
- [112] J.D. Ferry, R.F. Landel, and M.L. Williams. Extensions of the Rouse Theory of Viscoelastic Properties to Undiluted Linear Polymers. *Journal of Applied Physics*, 26(4):359–362, 1955.
- [113] Deutsches Institut für Normung. *DIN 53504, Prüfung von Kautschuk und Elastomeren; Bestimmung von Reißfestigkeit, Zugfestigkeit, Reißdehnung und Spannungswerten im Zugversuch*. Beuth, Ausgabe: 1994-05.
- [114] C. Uhlig, O. Kahle, B. Wieneke, and M. Bauer. A New Method for the Automatic Determination of Fracture Toughness of Polymers. *Forum der Forschung*, 5(11):50–53, 2000. BTU Cottbus.
- [115] J. Keller, C. Uhlig, O. Kahle, B. Wieneke, B. Michel, and M. Bauer. Optical Crack Tracing - A New Method for Automatic Fracture Toughness Measurement. In Werkstoffwoche-Partnerschaft, editor, *Materials Week 2000 and 2001, Proceedings*, Frankfurt, 2002. Werkstoff-Informationsgesellschaft.
- [116] C. Uhlig, O. Kahle, B. Wieneke, and M. Bauer. Optical Crack Tracing - A New Method for the Automatic Determination of Fracture Toughness for Crack Initiation and Propagation. In *Proceedings of the 3rd International Micro Materials Conference, Berlin, 17-19 April 2000*, pages 618–629, 2000.

- [117] C. Uhlig, O. Kahle, B. Wieneke, and M. Bauer. Optical Crack Tracing - A New Method for the Automatic Determination of Fracture Toughness for Crack Initiation and Propagation. In *3rd Int. Conf. Mechanics of Time Dependent Materials, Erlangen, Sept. 17-20, 2000*, 2000.
- [118] G. Binning, H. Rohrer, C. Gerber, and E. Weibel. Surface Studies by Scanning Tunneling Microscopy. *Physical Review Letters*, 49(5):57–61, 1982.
- [119] G. Binning, C.F. Quate, and C. Gerber. Atomic Force Microscope. *Physical Review Letters*, 56(9):930–933, 1986.
- [120] B. Bhushan, editor. *Springer Handbook of Nanotechnology*. Springer, 2004.
- [121] ThermoMicroscopes, Sunnyvale, California. *User's Guide to Autoprobe CP and M5*, August 2000.
- [122] Y. Martin, C.C. Williams, and H.K. Wickramasinghe. Atomic Force Microscope-Force Mapping and Profiling on a sub 100-Å Scale. *Journal of Applied Physics*, 61(10):4723–4729, 1987.
- [123] D. Sarid and V. Elings. Review of Scanning Force Microscopy. *Journal of Vacuum Science and Technology B*, 9(2):431–437, 1991.
- [124] Q. Zhong, D. Inniss, K. Kjoller, and V.B. Elings. Fractured Polymer/Silica Fiber Surface Studied by Tapping Mode Atomic Force Microscopy. *Surface Science Letters*, 290:L688–L692, 1993.
- [125] S.N. Magonov and M.-H. Whangbo. *Surface Analysis with STM and AFM: Experimental and Theoretical Aspects of Image Analysis*. VCH, Weinheim, 1996.
- [126] P. West and N. Starostina. *A Guide to AFM Image Artifacts*. Pacific Nanotechnology, <http://www.pacificnanotech.com/afm-artifacts.html>.
- [127] D.T. Nguyen. Messgenauigkeit von nanoDAC - Verschiebungsfeldmessungen im Scanning Force Microscope. Master Thesis, Technische Fachhochschule Berlin, Berlin, 2003.
- [128] B. Wunderle, J. Auersperg, V. Groer, E. Kaulfersch, O. Wittler, and B. Michel. Modular Parametric Finite Element Modelling for Reliability-Studies in Electronic and MEMS Packaging. *Proc. of Symposium on Design, Test, Integration and Packaging of MEMS/MOEMS, May 5-7, Cannes, France*, pages 335–340, 2003.
- [129] SAS IP. *ANSYS 7.0 Documentation*, 2002.
- [130] Image Instruments. *ADASIM User Manual, ADASIM Version 1.1*. Image Instruments GmbH, Chemnitz, Germany, 2004.
- [131] D. Vogel, V. Grosser, A. Schubert, and B. Michel. MicroDAC Strain Measurement for Electronics Packaging Structures. *Optics and Lasers in Engineering*, 36:195–211, 2001.

Lebenslauf

Name:	Jürgen Keller
Geburtstag:	10.06.1972
Geburtsort:	Bad Sobernheim
1978–1982	Grundschule in Monzingen
1982–1991	Staatliches Gymnasium in Bad Sobernheim
05/1991	Allgemeine Hochschulreife
1991–1992	Grundwehrdienst, JaboG 34, Bad Sobernheim
1992–1999	Studium Maschinenbau und Verfahrenstechnik an der Universität Kaiserslautern
05/1996–10/1996	Studium an der University of Bristol, England
11/1998–05/1999	Diplomarbeit am Shonan Institute of Technology, Fujisawa, Japan
06/1999	Abschluss des Studiums als Diplom-Ingenieur, Thema der Diplomarbeit: „Friction and Wear Properties of Continuous-Fibre Ceramic-Matrix Composites“, Universität Kaiserslautern, durchgeführt am Shonan Institute of Technology, Fujisawa, Japan
10/1999–2003	Wissenschaftlicher Mitarbeiter am Lehrstuhl für Polymerwerkstoffe der Brandenburgischen Technischen Universität Cottbus
seit 10/1999	Promotion mit dem Thema: „Micro- and Nanoscale Characterization of Polymeric Materials by Means of Digital Image Correlation Techniques“ am Lehrstuhl für Polymermaterialien der Brandenburgischen Technischen Universität, Cottbus, in Zusammenarbeit mit dem Fraunhofer Institut für Zuverlässigkeit und Mikrointegration, Berlin
seit 06/2003	Tätigkeit als Entwicklungsingenieur Micro- and Nanomaterials in der AMIC Angewandte Micro-Messtechnik GmbH, Berlin

Erklärung

Ich versichere, dass ich die von mir vorgelegte Dissertation selbständig und ohne unzulässige Hilfe angefertigt, die benutzten Quellen und Hilfsmittel vollständig angegeben und die Stellen der Arbeit – einschliesslich Tabellen und Abbildungen – die anderen Werken im Wortlaut oder dem Sinn nach entnommen sind, in jedem Einzelfall als Entlehnung kenntlich gemacht habe, dass diese Dissertation noch keiner anderen Fakultät zur Prüfung vorgelegen hat, dass sie noch nicht veröffentlicht worden ist, sowie dass mit der Veröffentlichung der Dissertation bestehende Schutzrechte nicht verletzt werden.

Die Bestimmungen der geltenden Promotionsordnung sind mir bekannt. Die von mir vorgelegte Dissertation ist von Frau Prof. Dr. Monika Bauer und Herrn Prof. Dr. Bernd Michel betreut worden.

Jürgen Keller